CENTRO DE INVESTIGACIÓN Y DE ESTUDIOS AVANZADOS DEL INSTITUTO POLITÉCNICO NACIONAL

UNIDAD QUERETARO

Chitin nano-fibers processed by supercritical carbon dioxide and thermal properties of chitosan films

Thesis Submitted by

José Francisco Louvier Hernández

For the Degree of

Doctor in Science

In the Specialty of

Materials

Thesis Advisors: Dr. J. Gabriel Luna Bárcenas
Dr. J. Francisco Javier Alvarado

Santiago de Querétaro, Qro. April, 2006

CENTRO DE INVESTIGACIÓN Y DE ESTUDIOS AVANZADOS DEL INSTITUTO POLITÉCNICO NACIONAL

UNIDAD QUERETARO

Nano-fibras de quitina procesadas con dióxido de carbono supercrítico y propiedades térmicas de películas de quitosán

Tesis que presenta

José Francisco Louvier Hernández

para obtener el Grado de

Doctor en Ciencias

en la Especialidad de

Materiales

Codirectores de la Tesis: Dr. J. Gabriel Luna Bárcenas
Dr. J. Francisco Javier Alvarado

Santiago de Querétaro, Qro. Abril de 2006

To my son, José Manuel, who is
learning to walk and barely speaks,
but through whom I can feel God's majesty.

Also to my new son or daughter,
who is 5 cm height and is already
a light of hope in our lives.

Finally, to my wife, Cristina,
for her continuous support, thrust,
and endless patience.

¿Con qué he de irme?
¿Nada dejaré en pos de mí sobre la tierra?
¿Cómo ha de actuar mi corazón?
¿Acaso en vano venimos a vivir,
a brotar sobre la tierra?
Dejemos al menos las flores
Dejemos al menos cantos

What will I take when leaving?
Would I leave nothing on earth after me?
How should act my hearth?
May be come to live in vain,
to grow over the earth?
Let leave at least, flowers
Leave at least, singing

De *Un recuerdo que dejo*
From *A memory I left*

Nezahualcóyotl (1402-1472)

Preface

It was in January 2002 when I decided to begin my doctoral studies. Four years have passed since then and, of course, there are thousands of stories to tell. During the first and a half year I was dedicated to the installation of the high-pressure equipment. I want to acknowledge the continuous support of Roberto Limón Campos, Maximiliano Nuñez Ramírez and Fernando Trejo Reséndiz for their help in setting up facilities for the laboratory, and special thanks to Pedro García Jiménez, laboratory technician that helped very much with tubbing bending and fittings.

At the same time, I got my first training with high-pressure experiments from Prof. Ciro Humberto Ortíz Estrada from Universidad Iberoamericana, Ciudad de México, who also helped me with phase behavior measurements. I also want to mention Sebastian Stolz, a student from the Technische Universität Berlin who was a visiting scholar at that time and from whom I learned my first lessons on supercritical fluids.

Then I spent one year —July 2003 to June 2004— at Auburn University with Prof. Ram B. Gupta. I appreciate very much his hospitality and guidance. It was in Auburn were I prepared the chitin nano-fibers. I want to thank my laboratory colleagues Jayant B. Gadhe, Amol Thote, Ranjit Thakur, John Chapell, Daniel Lilly, and Deepak Sree; our weekly meetings were a continuous source of learning for me and we shared a very nice time.

Special thanks to Chris B. Roberts, chair of the Chemical Engineering Department, for his warm hospitality. Also I thank Kellie Wilson, Sue Ellen Abner, and Joe Aderholdt for paperwork and laboratory assistance. Finally, help with SEM measurements was provided from Prof. Michael Miller.

At my return to México, I was dedicated to characterizing the obtained nano-fibers and to reproduce the experiment at Cinvestav. I want to thank María del Carmen Delgado Cruz for her continuous support with thermal measurements and Dr. Faustino Mijangos from Mettler Toledo for his help in detecting the thermal artifact. Martín A. Hernández Landaverde and José Eleazar Urbina Álvarez were very helpful with X-Ray and SEM measurements. I want to express my gratitude to Gloria Alejandra Camacho Bragado, from University of Texas at Austin, for her valuable help with TEM measurements, as well as for her helpful comments on SEM sample preparation.

The idea of evaluating the thermal properties of chitosan using Impedance Spectroscopy was born in February 2005. Since these measurements with biopolymers were a novelty for Cinvestav-Querétaro, we spent a great amount of time at sample preparation and preliminary evaluation. I want to express my deepest gratitude to Prof. Evgen Prokhorov Federovitch for his time, dedication, and guidance in this part of the work. It was a pleasure to work with him. Alfredo Muñoz Salas was very helpful with impedance measurements. I acknowledge Prof. Sergio Manuel Nuño Donlucas for useful discussions on calorimetric and infrared analysis, as well as for calorimetric measurements that were done in his laboratory at the Universidad de Guadalajara.

I greatly appreciate the guidance and continuous support from my thesis advisors Profs. J. Gabriel Luna Bárcenas and J. Francisco Javier Alvarado. I also want to thank the members of the committee, Profs. Arturo Mendoza Galván, Evgen Prokhorov Federovitch, Rafael Ramírez Bon, and Aldo Humberto Romero Castro from Cinvestav-Querétaro, and Prof. Kirk Ziegler from University of Florida. They provided valuable comments that enriched this work. Special thanks to Profs. Mendoza Galván and Romero Castro for their constructive and detailed observations.

I had very useful discussions with my classmates at Cinvestav: Guadalupe Barreiro Rodríguez, Ana María López Beltrán, Rodrigo Mayén Mondragón, Zeuz Montiel González, and Diana Ruíz Serrano. I appreciate the collaboration of Jhoana Aréchiga Carbajal from Universidad de Sinaloa, who spent one month at our Center and helped me with the preparation of some Laboratory Standard Methods. I thank Janett Betzabé González Campos for helping with Impedance Spectroscopy measurements, as well as for useful discussions and preparation of some Laboratory Standard Methods. I am indebted with Reina Araceli Mauricio Sánchez —Supercritical Fluids and Polymers Laboratory Technician— not only for laboratory assistance, but for her friendship. She was specially helpful with paperwork during my stay at Auburn University.

Financial support for this project was provided by NSF (CTS-0219271) for the USA team and by NSF-CONACYT (U-39377) for the Mexican team. CONCYTEQ (project 106/02) also funded part of this research. I appreciate the four-year doctoral scholarship provided by the Mexican Government through CONACYT. As a visiting scholar, I want to thank Auburn University and COMEXUS for providing the fundings for my stay. I was honored with a six-month Fulbright-García Robles scholarship. I am also indebted with Fundación Telmex for a scholarship supplement

during the first three years of my doctoral studies. I want to thank the Research and Technological Development Center (CID) from the DESC group for providing supplementary funding for my stay at Auburn University. Finally, I want to thank Cinvestav for the grant provided to present part of this thesis work at the 7th Symposium on Supercritical Fluids held in Orlando, Florida in May 2005. Thanks also to Cinvestav for the three-month financial support when the CONACYT scholarship was ended.

This project would had not been possible without the continuous support and love from my family. These four years were not an easy time for them, but now comes the reward. I must thank my wife, Cristina Pacheco Sánchez, for her patience during this time and for encouraging me all the time. At the end, I am very satisfied with the results of this work. I am glad to deliver this dissertation as the writing I left, as the *memory I left.*

JOSE FRANCISCO LOUVIER-HERNÁNDEZ

Querétaro, Qro, México, April 18, 2006.

Contents

List of Figures

List of Tables

Glossary

Abbreviations

CPE	Constant Phase Element.
CTN	Chitin.
CTS	Chitosan.
DA	Degree of Acetylation.
DCM	Dichloromethane.
DDT	Dichloro-Diphenyl-Trichloroethane.
DD	Degree of Deacetylation.
DMAc	N,N-Dimethylacetamide.
DMSO	Dimethylsulfoxide.
DSC	Differential Scanning Calorimetry.
DTA	Differential Thermal Analysis.
EPA	Environmental Protection Agency.
FDA	Food and Drug Administration.

FTIR	Fourier Transformed Infrared.
GRAS	Generally Regarded as Safe.
H-N	Havriliak and Negami relation.
HFC	Hydrofluorocarbon.
HFIP	1,1,1,3,3,3-Hexafluoro-2-propanol.
HPMA	Poly-(Hydroxypropylmethacrylamide).
IS	Impedance Spectroscopy.
M-W-S	Maxwell-Wagner-Sillars relaxation.
PCB	Polychlorinated Biphenyl.
PLLA	Poly-L-lactide.
PTFE	Polytetrafluoroethylene.
RESS	Rapid Expansion of Supercritical Solution.
SAS	Supercritical Antisolvent.
$SCCO_2$	Supercritical Carbon Dioxide.
SCF	Supercritical Fluid.
SEM	Scanning Electron Microscopy.
SFE	Supercritical Fluid Extraction.
TEM	Transmission Electron Microscopy.
TGA	Thermogravimetric Analysis.

UPL	Universal Power Law for Conductivity.
VFTH	Vogel-Fulcher-Tammann-Hesse relation for polymers.
XRD	X-Ray Diffraction.
ac	Alternating Current.
dc	Direct Current.
perc	Perchloroethylene.

Greek letters

α	Chitin polymorph with anti-parallel chain arrangement; dielectric relaxation; fitting parameter in Havriliak-Negami and Cole-Cole empiric relations.
β	Chitin polymorph with parallel chain arrangement; dielectric relaxation; fitting parameter in Davidson-Cole and Havriliak-Negami empiric relations.
δ	Solubility parameter.
ε^*	Complex permittivity.
$\varepsilon_r, \varepsilon'$	Real permittivity or dielectric constant.
$\varepsilon_i, \varepsilon''$	Imaginary permittivity or dielectric loss.
κ_e	Relative permittivity or relative dielectric constant.
ε_0	Permittivity of free space.
ε_s	Low-frequency limit permittivity or static permittivity.

ε_∞	High-frequency limit permittivity.
γ	Chitin polymorph with parallel/antiparallel chain arrangement; dielectric relaxation.
μ_0	Permeability of free space.
ω	Frequency in radians, $\omega = 2\pi f$.
σ^*	Complex conductivity.
σ'	Real part of complex conductivity.
σ_{dc}	dc conductivity.
σ_0	Preexponential factor for conductivity in Arrhenius and VFTH relations.
τ	Relaxation time.
τ_0	Preexponential factor for Relaxation time in Arrhenius and VFTH relations.

Symbols

$\mathbf{D}$	Electric flux density.
$\mathbf{E}$	Electric Field Intensity.
A	Characteristic constant of a CPE.
c	Velocity of Light.
C_0	Capacitance of vacuum or capacitancy of an empty cell, $C_0 = \varepsilon_0 S/d$.
C_x	Capacitance of a given dielectric.

d	Thickness of film sample, i.e. perpendicular distance between contacts.
$E_{a\sigma}$	Activation Energy for Conductivity.
$E_{a\tau}$	Activation Energy for Relaxation Time.
f	Frequency in Hz.
j	Complex number, $j^2 = -1$.
K	Pre-exponential material parameter for UPL.
n	Exponential material parameter for UPL.
P	Pressure.
P_c	Critical Pressure.
R	Resistance; Universal Constant of Gases equal to 8.314 J/mole.
R_0	Material bulk resistance.
S	Contact area of sample.
T	Temperature.
T_0	Vogel Temperature, also related to Kauzmann Temperature.
T_c	Critical Temperature.
T_g	Glass Transition Temperature.
u	Internal energy.
v	Specific volume.
Y^*	Complex admittance.

Y_i, Y''	Imaginay part of admittance.
Y_r, Y'	Real part of admittance.
Z^*	Complex impedance.
Z_i, Z''	Imaginay part of impedance.
Z_r, Z'	Real part of impedance.

Abstract

In this work a three-dimensional nano-fibrous network of chitin biopolymer has been prepared using supercritical carbon dioxide as anti-solvent; additionally, thermal properties of chitosan films have been analyzed with Impedance Spectroscopy. The supercritical anti-solvent processed biomaterial presents high porosity and very low density. Temperature and pressure were set to 40 °C and 103.4 bar, respectively; chitin was dissolved in hexafluoroisopropanol and the solution was then sprayed into supercritical carbon dioxide, which rapidly removes the organic solvent forcing chitin to precipitate as fibers. The resultant fibers are a white-yellowish, fluffy and sticky, with an estimated bulk density of 0.01 g cm^{-3} Based on Scanning Electron Microscopy, each fiber is formed of a three-dimensional nano-fibrous structure of about 80 nm in diameter. Fourier Transform Infrared Spectroscopy performed on raw chitin and chitin nano-fibers indicates that chemical structure is preserved during the supercritical anti-solvent process, while X-Ray Diffraction analysis evidence a loss in crystallinity for nano-fibrous chitin. There is a controversy about the existence of a glass transition temperature in chitin and chitosan. Using Impedance Spectroscopy, thermal relaxations of chitosan films are investigated in the frequency range $10^2 - 10^7$ Hz and temperatures from 25 to 250 °C. By applying the Vogel-Fulcher-Tamann-Hesse relation on the conductivity and relaxation time plots, a glass temperature of about 60-80°C is obtained.

Keywords: chitin, chitosan, biopolymer, biomaterial, supercritical carbon dioxide, supercritical anti-solvent, thermal relaxation, glass temperature, impedance spectroscopy.

Resumen

En este trabajo se preparó un material de quitina con estructura tridimensional nano-fibrosa usando dióxido de carbono supercrítico como anti-solvente; adicionalmente se analizaron las propiedades térmicas de películas de quitosán mediante Espectroscopía de Impedancia. El biomaterial procesado mediante anti-solvente supercrítico presenta una gran porosidad y es extremadamente liviano. La temperatura y presión se establecieron a 40 °C y 103.4 bar, respectivamente; la quitina se disolvió en hexafluoroisopropanol y esta solución se atomizó dentro del dióxido de carbono supercrítico, el cuál remueve rápidamente al solvente orgánico provocando la precipitación de la quitina en forma de fibras. Las fibras obtenidas son color blanco-amarillento, esponjosas y ligeras. La densidad aparente aproximada es de 0.01 g cm^{-3} Cada una de las fibras esta conformada de un estructura tridimensional nano-fibrosa con diámetros de 80 nm aproximadamente. La espectroscopía de infrarrojo indica que la estructura química se preserva durante el procesamiento supercrítico, mientras que el análisis de Difracción de Rayos-X hace evidente una pérdida en la cristalinidad del material. Por otra parte, existe controversia sobre la existencia de la temperatura vítrea en la quitina y quitosán. Por ello, se analizaron las relajaciones térmicas de películas de quitosán utilizando espectroscopía de impedancia, en el intervalo de frequencia entre $10^2 - 10^7$ Hz y de temperatura de 25 a 250 °C. Aplicando la relación de Vogel-Fulcher-Tamann-Hesse a las gráficas de conductividad y tiempo de relajación, se obtuvo un valor de temperatura vítrea de entre 60-80 °C.

Palabras clave: quitina, quitosán, biopolímero, biomaterial, dióxido de carbono supercrítico, anti-solvente supercrítico, relajación térmica, temperatura vítrea, espectroscopía de impedancia.

Chapter 1

Introduction

In recent years, the related biopolymers chitin and chitosan have attracted growing interest in diverse industrial areas as health care, agriculture, biomedical, and food additives. Chitin (CTN) is not only the second most common polysaccharide in world, but it also possess a combination of individual properties that makes it attractive for applications in several market niches, many of them potentially high-value.

Chitin occurs as component of crustacean shells, insect cuticles, certain fungi, and the cell walls of specific plants. It is found in crustacean exoskeletons in association with proteins and minerals such as calcium carbonate. Different sources of chitin differ somewhat in their structure and percentage of chitin content. For example, α-chitin from crab and shrimp, is a highly crystalline polymorph in which polymer chains are tightly packed in anti-parallel arrangement forming an orthorhombic crystal structure. making this polymorph very difficult to dissolve. In the other hand, β-chitin, from squid pen, has a less crystalline structure, in which polymer chains are arranged in parallel, forming a monoclinic crystal structure. β-chitin has weaker inter-molecular hydrogen bonding than α-chitin, and dissolution is not as difficult; however, β-chitin could revert to the α form when precipitated from solution [4]. Chemically, chitin is a natural occurring polymer formed primarily of $\beta - (1 \rightarrow 4)$-2-acetamido-2-deoxy-D-glucose repeating units. Few known solvents can dissolve chitin, like mixtures of N,N-Dimethylacetamide (DMAc) with 5 wt% LiCl, or 1,1,1,3,3,3-Hexafluoro-2-propanol (HFIP). Chitosan (CTS) is obtained upon deacetylation of chitin, it is soluble in aqueous dilute organic acids, and for this reason is more widely used than chitin. Current research in the biomedical area is being conducted for testing chitin hemostatic properties [5, 6, 7] as well as the use of chitin/chitosan as scaffolds for tissue repair [8, 9, 10, 11, 12]. These kind of materials might be further commercialized into the specialty medical field.

Regarding the process for manufacturing biomaterials, supercritical anti-solvent (SAS) process is a novelty. Nowadays, several biomaterials are produced by different means: extrusion, injection, and thermoforming for polymeric materials used in artificial organs; melt spinning, wet spinning, or electrospinning for producing fibers used in sutures, grapes and meshes; milling, grinding, and lyophilization, for particle formation in pharmaceutical applications; and forging, casting, and machining for metals to be used as implants. Recently, supercritical fluid (SCF) processes are being used for particle design, mainly in the pharmaceutical field, in specific for drug delivery applications[13, 14], but also for polymerization reactions in supercritical carbon dioxide[15]. Both techniques can be useful in biomaterials field. Any substance that exists above its critical temperature and pressure is called a supercritical fluid, showing an advantageous combination of liquid and gas properties. Its density can be tuned to achieve values comparable to a liquid, that will impart the SCF appreciable dissolving power; the diffusion coefficient is generally higher than in liquids with lower viscosities, therefore, by manipulating its temperature and pressure, a SCF can have liquid-like densities with enhanced transport properties. Furthermore, because of the high compressibility of SCFs near the critical point, their density and dissolving power can be adjusted by small changes in pressure or temperature. SCFs have been proposed for replacing —or reducing— toxic organic solvents. Biomaterials science may take advantage of these benefits for materials processing: a green technology capable to produce novel structures and dry, solvent-free materials, which is highly desirable for biomaterials.

While the interest in CTN and CTS biopolymers has gained strong momentum, development of commercial applications has occurred slowly. One of the reasons for this situation is due to the lack of synthesized materials with high-added value. Although companies in the United States and the rest of the world have made serious efforts to market chitin, chitosan and their derivatives during the past decade; markets for these biopolymers remain largely underdeveloped. Japan provides the greatest promise for developing reasonably sized markets. Japanese companies are producing roughly 5 000 ton of chitin and chitosan annually. By contrast, the U.S. figure scarcely exceeds 5 ton per year. The medical field has emerged as the most promising, despite the fact that companies entering that arena must cope with tough requirements of regulatory approvals. Here, in particular, Japan leads the way. Japanese sales of CTN and CTS related medical products have reached about USD$1 billion per year. These uses promise higher margins than any other field, because they will require starting substances with high purity. The most promising application in health care at present is wound-healing. Several wound dressings are on the market in Japan, like surgical sutures that dissolve in the body. In the U.S., wound-healing ointments are beginning to emerge. As a consequence of the above, it is imperative to address a market-driven research.

In the dawn of 21st century, the necessity for protecting the environment along with development of alternate renewable energies in substitution of fossil fuels, and the increasing conscience of sustained development, are guiding research efforts to use cleaner technologies and natural degradable materials such as SCFs and biopolymers. Biomaterials science is an increasing area of opportunity regarding natural materials and clean technologies.

In part of this work, chitin biopolymer was processed with supercritical carbon dioxide as anti-solvent, and a novel structure is obtained which may be used as a scaffold for cell culture in tissue engineering. This part of the work can be regarded as a first step in the technological production of a natural, biocompatible, solvent-free biomaterial. Scaling the production of this material will not be an easy task. The biomaterial should be first tested *in vivo* and it should meet several government regulations. Though there are several tasks to be complied before commercialize it, the opportunity is as large as biomaterials market, which is increasing every day and represents, only in the United States, a USD$ 9 billion market[16], while the global market can be two or three times greater.

On the other hand, understanding thermal relaxation processes in biomaterials is highly important for processing. As a complement of the work, a thermal relaxation study for chitosan films using impedance spectroscopy is done. Impedance spectroscopy is a powerful and very sensitive tool for the analysis of thermal relaxations. Having a complete knowledge of the material behavior will improve its processing for different applications.

1.1 Dissertation Outline

Background and fundamental concepts regarding chitin and chitosan biopolymers, supercritical fluids technologies, dielectric measurements and glass transition temperature are provided in the following sections: Chitin and chitosan are the biopolymers used in this work and a complete chemical and molecular structure description is provided along with a brief mention of their bioactive properties and some biomedical applications are given in section 1.2. Fundamentals on supercritical fluids and a wide description of their industrial and research importance are reviewed in section 1.3. Several techniques are used for determining the glass transition temperature in polymers, among them Impedance Spectroscopy (IS) is very sensitive for detecting such transition. Basic concepts for dielectrics, impedance measurement, and equivalent circuit approaching for relaxation time evaluation are explained in section 1.4 along with the correlation for glass transition temperature in polymers using the Vogel-Fulcher-Tamman-Hesse relation.

The main objectives of this work are detailed in Chapter 2. These are twofold: to produce a nano-fibrous chitin biomaterial processed with supercritical carbon dioxide as anti-solvent; and to study thermal relaxations in chitosan films using Impedance Spectroscopy.

Experimental details are given in Chapter 3, while results and discussion are presented in Chapter 4. Part of the information contained in this thesis was already published in the *Journal of Biomedical Nanotechnology*, from American Scientific Publishers [17]. Finally, in Chapter 5, conclusions are presented and future work perspectives are also discussed.

1.2 Chitin and Chitosan

1.2.1 Chitin

Chitin is a natural occurring polysaccharide and can be regarded as nitrogenated cellulose, with an acetylamino group substituted at C-2 (Figure 1.1 instead of the hydroxyl group of cellulose, and hence, the IUPAC name is (1 → 4)-2-acetamido-2-deoxy-β-D-glucan. It is defined as "a horny polysaccharide that forms part of the hard outer integument especially of insects, arachnids, and crustaceans" by the Merriam-Webster Online Dictionary [18].

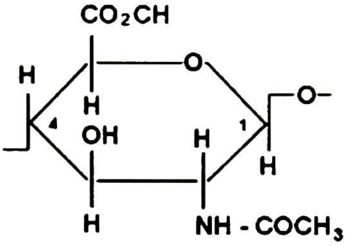

Figure 1.1: Chitin basic unit or monomer

It is the second most abundant polysaccharide in nature after cellulose, and its total annual production by arthropods has been estimated to be more than one billion ton per year [19]. Its existence was first reported by Braconnot in 1811 [20], who discovered it when he was studying derivatives from *Agaricus volvaceus* and other fungi. He called it "fungine" as it was a component of fungi. In 1823, Odier found a similar material in the cuticle of beetles and named it "chitin" from the Greek *chiton, kítos, tunic* [20, 21] or $\chi\iota\tau o\mu\gamma$ [22], which means "coat of mail" or envelope. A coat of mail is "a garment of metal scales or chain mail worn as armor" [23], and this analogy is due to the protective character of chitin in insects and arthropods. The chemical composition and structure of chitin was elucidated as time passed.

In 1935, Meyer and Pankow [24] found that chitin had an orthorhombic unit cell and crystallized in space group V_3 or V_2. Clark and Smith [25] performed X-ray studies verifying the proposed structure. In 1950, Darmon and Rudall [26] using infrared analysis, found that adjacent chains are bound together by hydrogen bonds. Later on, Carlström [27] proposed a refinement of the α-chitin structure, followed by other works by Pearson *et al.* [28] and Dweltz [29]. Finally, in 1962, Carlstöm [30] made an observation about the spatial configuration of the polysaccharide chain of chitin. In the same manner, the structure of β-chitin was initially proposed by Dweltz [31] in 1961 and by Blackwell [32] later in 1969. Finally, it was refined in 1975 by Gardner and Blackwell [33]. Structural differences between α- and β-chitins were studied by infrared and X-ray diffraction analysis by Gow *et al.* [34] and Focher *et al.* [35]. Most of the recent research regarding chitin may be attributed to Prof. Muzzarelli at University of Ancona. His 1977 book [36] was a pioneer work and, in conjunction with the International Conferences on Chitin and Chitosan —initiated the same year—, were the generators of the increasing research interest on this biopolymer.

1.2.2 Chitosan: a Chitin Derivative

The discovery of chitosan is assigned to Rouget in 1859, when he found that boiling chitin in potassium hydroxide yielded an acid soluble chitin. In 1894, Hoppe-Seyler named it chitosan, however its molecular structure was not resolved until 1950. The existence of chitosan in nature was unknown before 1954, when it was discovered in the yeast *Phycomyces blakesleeanus.* Chitosan occurs as the major structural component of the cell walls of certain fungi, mainly of the *Zygomycetes* species.

Chitosan undergoes a recent boom as a weight loss aid. It is obtained by alkaline deacetylation of chitin isolated from shrimp or crab shells [37]. It is insoluble in water but soluble in most acidic media (pH lower than 6.5), the preferred solvent being acetic acid. Unlike cellulose, chitosan biodegrades in human tissue because it is susceptible to the action of the lysozyme enzyme, present in human body. It also possess anti-viral properties such that it can be used in bandages, sponges, artificial skin, contact lenses, controlled drug release, antimicrobial preparations, artificial blood vessels, and bone healing treatment [38, 39, 40, 37]. The utilization of chitosan in the above applications has many interesting advantages. It is inexpensive since it is obtained from the naturally abundant crustacea which are the waste of the fishery industry. Chitosan is non-toxic, biocompatible and biodegradable. Chitosan is also a polyelectrolyte widely used as flocculant binding proteins and other negatively charged molecules in solution. On the other hand, chitosan can also bind metal ions by forming complexes rather than charge attractions.

Chitosan nanoparticles have been prepared for different medical and pharmaceutical applications such as doxorubicin carriers [41], oral immunization synthesized with plasmid DNA [42, 43, 44], cancer therapy [45], as drug delivery in ocular mucosa and body [46, 47], or as composite biomaterial like chitosan-hydroxyapatite. [48]

1.2.3 Sources and Production

Chitin occurs as component of crustacean shells, insect cuticles, certain fungi, and the cells walls of specific plants. It is found in crustacean exoskeletons in association with proteins and minerals such as calcium carbonate. Chitin is produced from the processing waste of shellfish, krill, clams, oysters, and fungi. Chitin and chitosan also have a commercial interest due to their relatively high percentage of Nitrogen (6.89%) compared to synthetically substituted cellulose (1.25%), thus attracting interest for its production and commercialization. Chitosan and chitin are sold for pharmaceutical, cosmetical or medical applications. Here is a list of some of the principal producers in the world:

1. France Chitine (www.france-chitine.com) provides a wide range of prime quality chitosan produced in two factories, one in Africa and one in India. France Chitine's chitosans are made from shrimp shells and squid bones and has the capacity to supply 500 tons of finished products annually.
2. Dalwoo-ChitoSan (http://dalwoo.com) is a Korea based corporation involved with the extraction, processing and sale of the highly purified chitin, chitosan, and chitosan oligomer in various grades since 1988.
3. Heppe GmbH (www.biolog-heppe.de) from Germany, has a production capacity of 250 ton per year in its facility in Halle-Queis, near Berlin. This is one-tenth of the world production of chitosan. The processing of the raw material is done in various countries to guarantee a wide variety of products and balance out different seasonal conditions. This company have plans for extend its capacity to 750 ton per year.
4. Primex (www.primex.is) from Iceland, manufacture chitin and chitosan from the North Atlantic shrimp, *Pandalus borealis*, with an annual capacity of production up to 500 tons of chitosan. It has a market share in Europe and in Asia of around 50%, and has strengthened its position as the world's leading producer of chitosan products through the acquisition of the bulk chitosan business of Vanson HaloSource from US.

1.2.4 Structure and Properties

Chitin ideal molecular structure is depicted in Figure 1.1 as a linear polysaccharide of β-(1$\rightarrow$ 4)-2-acetamido-2-deoxy-D-glucopyranose where all units are comprised entirely of N-acetyl-D-glucosamine. Chitosan is the deacetylated form of chitin, and its molecular structure (Figure 1.2) is idealized as a linear polysaccharide of β-

(1→ 4)-2-amino-2-deoxy-D-glucopyranose where all units are comprised entirely of D-glucosamine. However in most natural forms, this biopolymer exists as a random copolymer of D-glucosamine and N-acetyl-D-glucosamine units. When the number of acetamido groups is more than 50% (more commonly 70-90%) the biopolymer is termed chitin, in contrast, when the number of acetamido groups is less than 50% (more commonly 10-30%) it is termed chitosan [20].

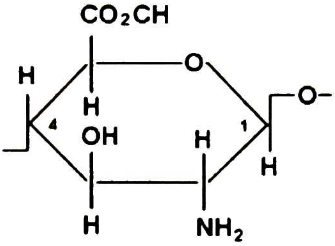

Figure 1.2: Chitosan basic unit or monomer

Even they differ chemically only on the content of acetamido groups —commonly known as degree of acetylation (DA)—, several properties are being affected drastically by it. For example, chitin (Poly-N-acetyl-D-glucosamine) can be dissolved by few known solvents. Mixtures of N,N-Dimethylacetamide (DMAc) with 5 wt% lithium chloride (LiCl) [49, 50], methanol saturated with calcium chloride dihydrate [51], or hexafluoroisopropanol (HFIP) and hexafluoroacetone sesquihydrate [52, 53] are the known solvents that can solubilize it without alteration of its chemical structure. Chitosan, on the other hand, can be solubilized in acidic media. The most common solvents are diluted organic acids such as acetic, formic, and lactic.

Structure of chitin exists in three polymorphic states: α-chitin —from crab and shrimp— is a highly crystalline polymorph in which polymer chains are tightly packed in an anti-parallel arrangement. The crystal unit cell is orthorhombic. The second polymorph is β-chitin —found in squid pen and fungi— and it has a less crystalline structure. Polymer chains are arranged in a parallel fashion and the crystal unit cell is monoclinic. It is known that β-chitin has weaker intermolecular hydrogen bonding than α-chitin, and hence can be solublized in concentrated formic acid. The last polymorph is γ-chitin, which is a combination of the previous forms with some chains in parallel and others in anti-parallel arrangement. Although chitosan is a semi-crystalline polymer, it has much less crystallinity than chitin. Additionally, the amino group protonates in acidic media facilitating its solubilization.

Typical chitin and chitosan properties are [36]:

1. **Biodegradable.** Chitin and chitosan are biodegradable biopolymers. Enzymes like chitinase and chitosanase —and lysozyme, present in human body— break them down into oligo-polymers that are then dealt with by the metabolism.
2. **Biocompatible.** Chitin and chitosan are natural biopolymers. They have no antigenic properties, and thus are perfectly compatible with living tissue. Their antithrombogenic and hemostatic properties make them very suitable for use in all fields of biology.
3. **Cicatrizant.** Chitosan forms films that are permeable to air. It facilitates cellular regeneration while protecting tissue from microbe attack. In addition, chitosan has been found to have a stimulant effect on the regeneration of tissue. This property has allowed it to be used in making an artificial skin for skin grafts on high degree burns and in surgical applications such as chitin suture thread.
4. **Anticholesterolemic agent.** Chitosan can trap lipids at their insolubilization pH in the digestive tract. Administered to rats, chitosan considerably reduces the level of cholesterol in the blood.

5. **Chelation agent.** Chitin and its derivatives are remarkable chelation agents. Chitosan is used for a wide range of applications: as a chromatography medium, or for trapping heavy metals, or for water treatment. Chitosan has a strong positive charge, which allows it to bind with negatively charged surfaces or materials, including metals, skin, and macromolecules such as proteins.

1.2.5 Biomedical Applications

Chitosan can be referred to as a polycation. Polycations have been known to bind to red blood cells, thus are effective cellular agglutinating agents, even at very low concentrations. For this reason it is considered a hemostatic agent [54, 55, 36, 56]. The agglutination of red blood cells by polycations is dependent both on polymer structure and molecular weight. Out of six common polycations, only chitosan is able to effectively initiate gel formation of heparinized blood.

In the 1970s, researchers with the University of Delaware Sea Grant College Program [57] developed a method to spin pure chitin filaments [49]. These new chitin sutures could be absorbed by the body, eliminating the need for surgical removal. In addition chitin is used to make dressings for burns, surface wounds, and skin-graft donor sites, which dramatically accelerate healing and reduce pain compared to standard treatments where the dressings must be removed.

For burn treatments, chitosan can form a tough, oxygen-permeable films, which can be formed directly on the burn by application of an aqueous solution of chitosan acetate. The solution, although acidic, provides a cool and pleasant soothing effect when applied to the open wounds of burn patients. Oxygen permeability is important to prevent oxygen-deprivation of injured tissues. Additionally, chitosan films have the ability to absorb water and are naturally degraded by body enzymes. This fact means that the chitosan need not to be removed. In most injuries (and especially burns), removing the wound dressing can cause damage to the injury site. Some applications include artificial skin and suture thread that are absorbed naturally after cicatrization, and contact lenses that are well tolerated. Betschitib W, an artificial skin based on chitin, has been made in Japan since 1987 [58]. This skin is in the form of a tissue that is applied to the wound in one single operation: the dressing does not have to be changed. Betschitib W is gradually biodegraded until a new epidermis is formed.

Lastly, chitosan is an excellent medium for carrying and slow release of medicinal active principles in plants, animals and man. Since it is undigested by the stomach, it is, for example, a good means of retarding the release of encapsulated products that must reach the intestine without undergoing any transformation. The non-antigenic behavior of chitosan promises unlimited development in the health field.

1.2.6 Other Applications

Besides the medical and pharmaceutical applications of chitin and chitosan, their properties make them interesting candidates in diverse areas such as: cosmetics, dietetics, biotechnology, environment, water treatment, agriculture, paper manufacture, and textiles.

For water treatment, chitosan's chelating behavior can gather organic materials, such as oils, detergents, and other contaminants suspended in water. The material then coagulates to form flocs —or flakes— that are easily filtered out. The toxicity level of these natural products is about equal to table sugar. They are environmentally safe and harmless to plants, humans, fish and other animals. Chitin and chitosan are also used for treating drinking water by separating organic compounds and heavy metals, and for treating sewage by precipitating certain anionic wastes and capturing pollutants such as DDT (Dichloro-Diphenyl-Trichloroethane) and PCB (polychlorobenzene). The Environmental Protection Agency (EPA) has already approved the use of chitosan in water at concentrations of up to 10 mg per liter. For sewage treatment, chitosan can be used at up to 5 ppm. It reduces the oxygen demand by 80 to 85% and reduces the phosphates level to less than 5 ppm [59].

As a dietary supplement, chitosan has properties similar to plant fiber and can significantly bind fat, acting like a sponge in the digestive tract. It is not digestible itself and the bound fat leaves via the body without ever entering the bloodstream. Chitosan is already part of our everyday diet: we absorb it in its natural state in shellfish, crustaceans and mushrooms. It is already a common ingredient of food in Japan and its official approval is currently pending in Europe, where it has achieved a major breakthrough in dietetics as a fat trap.

In cosmetics, it is an ingredient of make-up powder; nail polish; moisturizers; face, hand, and body creams; and toothpaste [60, 61, 62]. The chemical structure of chitin is very close to that of mucopolysaccharides (heparin and hyaluronic acid), whose biological tolerance has been demonstrated for a long time. In addition, it is an efficient trapper of heavy metals that are responsible for very many contact allergies. Chitin is a particularly effective hydrating agent. It has two advantages: it supplies water and avoids dehydration. In addition, the great advantage of chitin and its derivatives is the lasting quality of their hydrating effect.

Lastly, chitosan forms a protective tensor film on the skin's surface that can fix other active principles for the skin. Thus other hydrating agents, solar filters, organic acids or other active principles can be combined with the derivatives of chitin. Chitin facilitates their effects.

In Agriculture, seeds treated with chitosan are larger and stronger and more resistant to fungal diseases. Treating seeds with chitin can increase crop yields by up to 50%. Chitin is added to commercial feed mixtures containing whey, a by-product of the cheese industry [63]. Many animals find it hard to digest the high-lactose whey. But chitin supports the growth of beneficial microorganisms in the animals' digestive tract —these bacteria produce enzymes that help the animals digest whey. Chitosan and its derivatives have plant protecting and antifungal properties. They can trigger defensive mechanisms in plants against infections and parasite attacks, in very low concentrations in the order of a few milligrams per cubic meter of water. They can be used in solution, in powder form or as coatings of seeds [64, 65]. Chitosan acts on several levels. Apart from its specifically antifungal action, it strengthens the root system and thickens the stem. Some studies also show that chitosan stimulates the plant's synthesis of protective agents. Moreover, chitosan behaves like a fertilizer by accelerating the germination and growth of plants. Chitin and chitosan could become both the natural fertilisers and the pesticides of the new century.

1.3 Supercritical Fluids

1.3.1 Definition and Properties of SCFs

A supercritical fluid (SCF) is defined as a substance above its critical temperature (T_c) and critical pressure (P_c). The critical point represents the highest temperature and pressure at which the substance can exist as a vapor and liquid in equilibrium. The phenomenon can be easily explained with reference to the phase diagram for a pure substance (Figure 1.3). The diagram shows the areas where carbon dioxide exists as a gas, liquid, solid or as a SCF. The curves represent the temperatures and pressures where two phases coexist in equilibrium (at the triple point, three phases coexist). The gas-liquid coexistence curve is known as the boiling curve. With an increase in temperature and pressure along the vapor pressure coexistence line, thermal expansion causes the liquid to become less dense, whereas the vapor becomes more dense. At the critical point, the liquid and vapor densities become identical and both phases merge into one fluid phase.

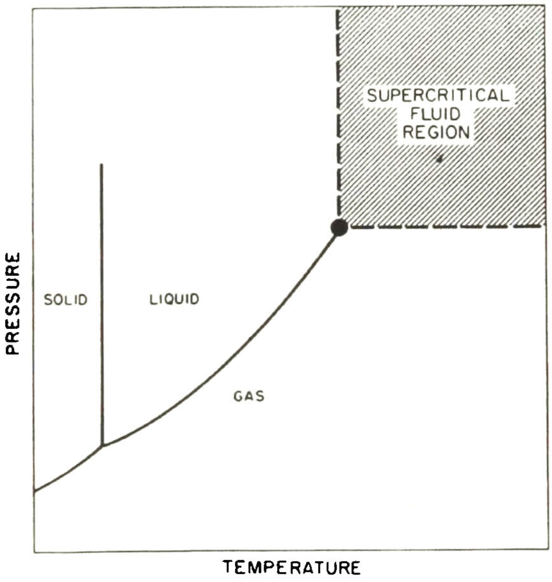

Figure 1.3: Pressure-Temperature diagram for pure carbon dioxide. Taken from [1]

The shaded area in Figure 1.3 correspond to the supercritical fluid phase. SCFs begin to exhibit significant solvent strength when they are compressed to liquid-like densities, and this solvent capacity is pressure-dependent. This makes physical sense intuitively since gases are not considered as solvents. The variable solvent capacity of a supercritical fluid is the basis on which separations processes can be devised. Table 1.1 lists critical temperature and critical pressure for a variety of substances. The critical point for carbon dioxide occurs at a pressure of 73.8 bar (1 070 psia) and a temperature of 31.1 °C (304.25 K). Because this temperature is near ambient, supercritical carbon dioxide ($SCCO_2$) is an attractive solvent for thermolabile compounds such as pharmaceutical, flavors, vitamins, and proteins. Besides, these parameters make equipment design and reaction set-up relatively simple.

Table 1.1: Critical parameters for various substances

Substance	**Mw, g/gmol**	T_c, **K**	P_c, **bar**	ρ_c, **g/cm**^{3}
Ethylene	28.05	282.4	50.4	0.215
Xenon	131.3	289.7	58.4	1.109
Carbon dioxide	44.01	304.1	73.8	0.469
Ethane	30.07	305.4	48.8	0.203
Propane	44.09	369.8	42.5	0.217
n-Butane	58.12	425.2	38.0	0.228
n-Hexane	86.18	507.5	30.1	0.233
Water	18.02	647.3	221.1	0.315

The most prominent property for SCFs is their density. Figure 1.3.1 shows the change in density of a pure solvent around the critical point. At reduced temperatures ($T_r = T/T_c$) in the range 0.9-1.2, the reduced solvent density ($\rho_r = \rho/\rho_c$) can increase from gas-like values of 0.1 to liquid-like values of 2.5 as the reduced pressure ($P_r = P/P_c$) is increased to values greater than one. This behavior is also observed for other properties such as cohesive energy density, enthalpy, viscosity, and diffusivity [1]. By operating around the critical region, pressure and temperature can be used to regulate density which, in turn, regulates the solvent power of a SCF. The reason is because density is related to the solubility parameter, δ, as:

$$\delta = \left(\frac{u^{ig} - u}{v}\right)^{1/2} \tag{1.1}$$

where u is the internal energy, v is the molar volume, and the superscript ig refers to the ideal gas. The solubility parameter value for gaseous carbon dioxide is practically zero, whereas, the value for liquid carbon dioxide is close to the value of a hydrocarbon ($15<\delta<20$). Above the critical temperature, it is possible to modify the solubility parameter over a wide range with only small changes in temperature or pressure.

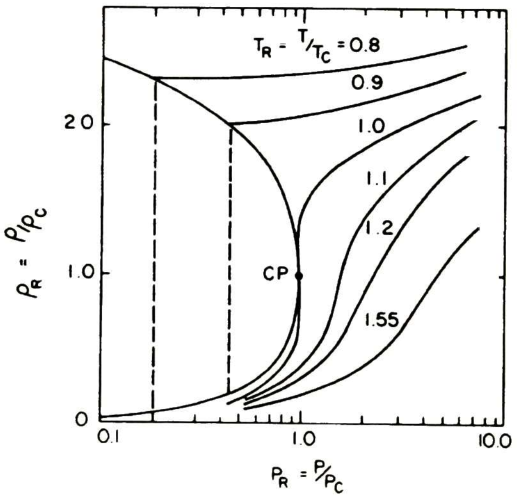

Figure 1.4: Variation of density as a function of pressure of a pure solvent near critical point. Taken from [1]

Since the variation in density changes directly the solubility parameter (square root of cohesion energy density), the behavior of δ is similar to that of ρ near the critical point as can be seen in Figure 1.5 where solubility parameter is shown as a function of pressure for CO_2 in supercritical, liquid and vapor states. The ability for tuning the solvent strength of a SCF is a unique feature, which can be used for several applications as we will learn later.

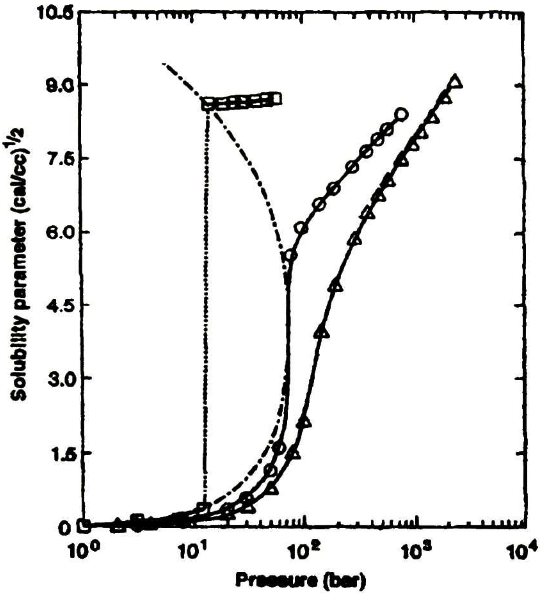

Figure 1.5: Solubility parameter for CO_2 as a function of pressure in the gas, liquid and supercritical states at -30 °C (squares); 31 °C (circles); and 70 °C (triangles), respectively. Taken from [2]

In addition to its unique solubility characteristics, a SCF possesses certain other physico-chemical properties that increase its attractiveness. For example, it exhibits gas-like transport properties of diffusivity and viscosity. In addition, the very low surface tension allows facile penetration into micro-porous materials to occur. Table

1.2 shows some typical values for density and transport properties among gas, liquid and supercritical states. In general, the attractiveness of SCFs is their liquid-like density with gas-like transport properties, making them a "liquid" solvents with increased mass transport properties.

Table 1.2: Comparison of some properties among vapor, liquid and supercritical states

Property	**Liquid**	**SCF**	**Vapor**
Density, g/cm^3	1	$0.1 - 0.5$	10^{-3}
Viscosity, Pa s	10^{-3}	$10^{-4} - 10^{-5}$	10^{-5}
Diffusivity, cm^2/s	10^{-5}	10^{-4}	10^{-1}

Among the substances used as solvents in supercritical phase, $SCCO_2$ is the widest used for a number of features to be discussed in the next section.

1.3.2 Supercritical Carbon Dioxide

Supercritical carbon dioxide is advantageous from an environmental standpoint because it is non-flammable, virtually inert, is not an ozone-depleting compound, and has GRAS (Generally Regarded As Safe) status. Recently $SCCO_2$ has emerged as an environmentally benign substitute for more conventional solvents. Although a greenhouse gas, it can be obtained in large quantities as a by-product of fermentation, combustion and ammonia synthesis. Its ready availability coupled with its ease of removal and disposal/recycling makes CO_2 an exciting prospect for synthetic and industrial applications. Therefore, it does not add to global warming potential and, in fact, reduces dependency on ozone-depleting solvents.

For a number of reasons, supercritical carbon dioxide is now well established as a solvent for different extraction processes. It can generally penetrate a solid sample faster than liquid solvents because of it's high diffusion rates, and can rapidly transport dissolved solutes from the sample matrix because of it's low viscosity. There are also of course less solvent residues present in the products.

A crucial aspect for carrying out reactions in $SCCO_2$ is the solubility of the substance in the supercritical solvent. Pure supercritical carbon dioxide is a relatively non-polar solvent, but has some limited affinity with polar molecules due to its large molecular quadrupole moment. Modifiers can often be added (e.g. methanol) to improve the solubility of polar molecules. Alternatively, if the reaction involve more than one reagent, less polar reagents can be used as modifiers enhancing the solubility of the substance in $SCCO_2$, thus avoiding the need to resort to additional co-solvents.

There are also a number of practical advantages associated with the use of supercritical carbon dioxide as a solvent. Product isolation to total dryness is achieved by simple evaporation. This could prove to be particularly useful in the final steps of pharmaceutical syntheses where even trace amounts of solvent residues are considered problematic. There are also two very useful complementary routes to particle formation with SCFs and supercritical carbon dioxide in particular: rapid expansion of supercritical solutions (RESS) and supercritical anti-solvent precipitation (SAS).

1.3.3 Supercritical Fluid Applications and Relevance

Supercritical Extraction. The most relevant application of supercritical fluids is the supercritical fluid extraction (SFE) process. There are several companies that provides products extracted with supercritical carbon dioxide, like Scenz (http://www.supercritical.co.nz) that manufacture extracts and oils by $SCCO_2$ extraction. This technology provides high quality, pure, solvent-free natural products and cosmetic oils. There is another company called Natex Prozesstechnologie (http://www.natex.at) in Austria that provides technology for SFE. Some examples for oil extraction performed in their R&D pilot plant are: arnica, eucalyptus, peppermint, parsley, ginseng, anise, cinnamon, garlic, paprika, cardamom, etc.

Supercritical Fluid Reaction. The properties of $SCCO_2$ make it an especially suitable solvent for large-scale industrial synthesis. In fact, two small-scale plants using $SCCO_2$, one owned by Thomas Swan & Co. (http://www.thomas-swan.co.uk) and the other by DuPont (http://www.dupont.com), have been in operation for several years. Thomas Swan & Co. has very recently completed a large plant for the use of supercritical carbon fluids in industrial scale synthesis. In addition, DuPont has allocated initially USD$40 millions for the construction of a plant for the production of fluoropolymers that was expected to be fully functional by 2006, and will represent a USD$275 millions facility [66, 67]. Moreover, DuPont has decided to construct a new facility in China with this technology [68].

Cleaning. Most traditional dry cleaning systems clean clothes using perchloroethylene (perc), a chemical that the EPA has classified as a groundwater contaminant and a potential human health hazard. Hangers Cleaners (http://www.hangersdrycleaners.net) is a company that uses a $SCCO_2$ patented process that yields superior cleaning results. Semiconductor wafer cleaning is another interesting process. Current generation technology relies on a variety of organic solvents and solvent blends for photoresist removal. Supercritical Systems and Praxair (http://www.praxair.com) in joint venture are developing a next-generation, single-wafer cleaning technology that uses supercritical carbon dioxide to remove photoresist and etch residue from low dielectric constant, κ_e, films.

Particle design. Nowadays, SCF's are being used to obtain nano-particles with narrow particle size distribution and free of solvent which is a major advantage for medical and pharmaceutical applications since it is possible to minimize toxicity and secondary effects. Supercritical fluids have been used in the formation of solvent-free, drug-loaded polymer microspheres for controlled drug release of therapeutic agents [69, 70], production of ultrafine and chemically pure ceramic precursors [71, 72], formation of intimate mixtures of ceramic precursors [73], formulation of crystalline powders of labile pharmaceutical drugs [74], and particle formation and design [14, 75]. The latter such interesting application for its ability to produce special material properties such as particle size, particle size distribution, porosity, surface area and morphology.

1.3.4 Particle Formation Processes

Particle formation or particle design is a major application of SCFs, basically for the pharmaceutical, nutraceutical, cosmetic and specialty chemistry industries. There is a very complete review published by Jung and Perrut in 2001, [14] the interested reader in a more detailed explanation is referred to it.

There are several different processes for particle formation using supercritical carbon dioxide. The first proposed process is called Rapid Expansion from Supercritical Solution (RESS) and consists in saturating the $SCCO_2$ with the solute to later depressurize the solution through a nozzle into a low pressure chamber. This pressure release causes a very fast nucleation and precipitation of the solute into small particles —or fibers, or films. The process is based in the solubilization of a solute into $SCCO_2$; unfortunately, there are only few substances that are soluble in $SCCO_2$. Very polar molecules such as sugars or amino acids and most inorganic salts are

Supercritical Anti-solvent Atomization (SAA) process has been developed to produce micro and nanoparticles of controlled size and distribution at University of Salerno, Italy (http://www.unisa.it). World and US patents were issued by Prof. Reverchon [76, 77]. This process is based on the solubilization of controlled quantities of $SCCO_2$ in liquid solutions containing a solid solute and on the subsequent atomization of the ternary solution through a nozzle. It has been successfully tested for: superconductor and catalyst precursors, ceramics, and drugs, using different liquid solvents like water, methanol and acetone.

Solution Enhanced Dispersion by Supercritical fluid (SEDS) was originally developed at Bradford University (http://www.brad.ac.uk). Prof. York issued world and US patents [78, 79, 80]. for this process which involves taking an aqueous solution of the drug, then decreasing the solvating power of the water by saturating it with carbon dioxide under supercritical conditions, the drug solution and a stream of supercritical carbon dioxide are mixed using a coaxial nozzle. The high velocity, turbulent, supercritical fluid stream breaks up the aqueous solution into very small droplets. A third stream, containing an organic solvent can be used to overcome immiscibility problems between the aqueous and supercritical carbon dioxide phases. The three nozzle process enables proteins to be exposed to denaturing conditions for a minimal amount of time [78]. Control over the size of the particles produced is achieved by variation of a number of process variables, including the flow rates of the three input streams to the nozzle, and the pressure drop across the nozzle [81]. Bradford Particle Design was established in 1994 by Prof. Peter York, Dr. Mazen Hanna and Dr. Gwyn Humphreys, to develop and manage the exploitation of the patented technology for controlled particle formation initially developed by Bradford University's School of Pharmacy. This company was acquired by Inhale Therapeutics Systems from US in 2001, in near USD$24 millions. Later on, in Janfor antisolvent than solute, forming a homogeneous phase. This can be explained more easily using the schematic of Figure 1.6. During the atomization, a droplet enters into the supercritical antisovent media (shaded area). The $SCCO_2$ possesses a higher diffusion coefficient into the solvent than the inverse. The arrows indicate the diffusion of each component and have been drawn of different sizes, being the $SCCO_2$ diffusion which dominates, causing the droplet size to increase. Due to this increase in size, the overall density of the solvent is decreased, and therefore its dissolving power. There is a moment when the solvent can hold no more the solute forcing it to precipitate, as depicted in Figure 1.6B. After the solute is precipitated, it is further washed with the supercritical antisolvent to remove any residual solvent, and finally depressurize the system for product collection.

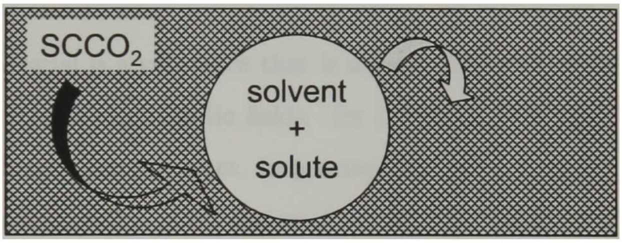

A. Atomized drop

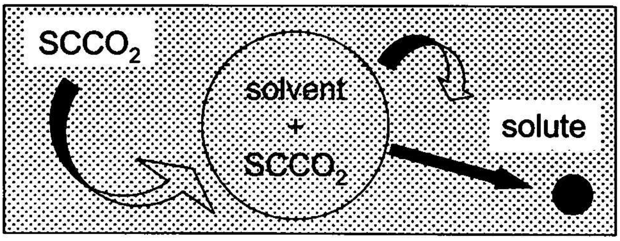

B. Precipitated solute

Figure 1.6: Schematic for SAS precipitation phenomenon

Supercritical carbon dioxide has been widely used for pharmaceutical processing for the last fifteen years, and several reviews have been published where the benefits of using supercritical CO_2 are highlighted, including: (a) reduced usage of conventional liquid solvents; (b) production of relatively contaminant-free products; (c) micron and submicron-size particles production with controlled particle size and purity; (d) control of porosity by choosing the appropriate process path; (e) extraction and fractionation of pharmaceutical compounds; (g) drug encapsulation, impregnation and coating; and (h) sterilization of pharmaceutical products.

1.4 Dielectrics fundamentals

1.4.1 Definition of a Dielectric

A dielectric material is a substance that is a poor conductor of electricity, but an efficient supporter of electrostatic fields. By definition it is (*dia+electric*) a non conductor of direct electric current. In practice most dielectric materials are solids. Examples include ceramics, glass, and plastics; also some liquids and gases can serve as good dielectric materials. Dry air is an excellent dielectric, distilled water is a fair dielectric, and vacuum is an exceptionally efficient dielectric. When exposed to an electric field, the electric charges in a dielectric material, including permanent and induced electric dipoles, can be moved, thus polarizing the material. An important property of a dielectric is its ability to support an electrostatic field while dissipating minimal energy in the form of heat. The lower the dielectric loss, ε'', the more effective is a dielectric material. The dielectric constant, ε', is the extent to which a substance concentrates the electrostatic lines of flux.

1.4.2 Permittivity and Dielectric Constant

Permittivity is the ability of a dielectric to store electrical potential energy under the influence of an electric field. It is measured by the ratio of the capacitance of a condenser with the material as dielectric, to its capacitance with vacuum as dielectric. It is also called dielectric constant. Electric permittivity, ε_0, and magnetic permeability, μ_0, of the free space are related by the equation:

$$c = \frac{1}{\sqrt{\mu_0 \varepsilon_0}} \tag{1.2}$$

where c is the velocity of light, and the value for permittivity of the free space is equal to $8.854187817 \times 10^{-14}$ F/cm. In the presence of a polarizable or magnetic media the effective constants will have different values. In the case of a polarizable medium, called a dielectric, the comparison is stated as relative permittivity or relative dielectric constant. The relative permittivity or dielectric constant, κ_e, is defined as the ratio of the static permittivity of a substance to the permittivity of the free space:

$$\kappa_e = \frac{\varepsilon_s}{\varepsilon_0} \tag{1.3}$$

It is an expression of the extent to which a material concentrates electric flux and is the electrical equivalent of the relative magnetic permeability. The permittivity of the free space is derived from Maxwell's equations by relating the electric field intensity, **E** to the electric flux density, **D**. Its relation to permittivity is given by:

$$\mathbf{D} = \varepsilon \cdot \mathbf{E} \tag{1.4}$$

where ε is a scalar if the medium is isotropic or a 3×3 matrix if it is anisotropic.

Permittivity can take a real or complex value. In general it is not a constant as it can vary with the position of the medium, the frequency of the applied field, humidity, temperature, and other parameters. In vacuum the relative dielectric constant is unity. The relative dielectric constant can be measured for static electric fields (dc) as follows: first the capacitance of a test capacitor, C_0, is measured in air between its plates. Then using the same capacitor and distance between its plates the capacitance with a dielectric between the plates, C_x, is measured. The relative dielectric constant can be then calculated as:

$$\kappa_e = \frac{C_x}{C_0} \qquad (1.5)$$

For time-varying electromagnetic fields, the dielectric constant becomes frequency dependent and in general is called permittivity. The permittivity of a given material is an intensive physical quantity that describes how an electric field affects and is affected by the medium. It can be looked at as the quality of a material that allows it to store electrical charge. A given amount of material with high permittivity can store more charge than a material with lower permittivity. A high permittivity tends to reduce any electrical field present. Therefore the capacitance of a capacitor can be increased by increasing the permittivity of the material inside it.

The permittivity is usually given relative to that of vacuum, as a relative permittivity. The actual permittivity is then calculated by multiplying the relative permittivity by ε_0:

$$\varepsilon = \kappa_e \varepsilon_0 \qquad (1.6)$$

The frequency dependence of permittivity reflects the fact that the polarization of a given material does not respond instantaneously to an applied field. For this reason permittivity is treated as a complex function of the frequency of the applied field, ω. The response of a medium to a static electric field is described by the low-frequency limit of permittivity, also called the static permittivity, ε_s:

$$\varepsilon_s = \lim_{\omega \to 0} \varepsilon^*(\omega) \tag{1.7}$$

At the high-frequency limit, the complex permittivity is commonly referred to as ε_∞. At the plasma frequency and above, dielectrics behave as ideal metals, with electron gas behavior. Since the response of materials to alternating fields is characterized by a complex permittivity, it is natural to separate the real and imaginary parts, where j is the complex number:

$$\varepsilon^*(\omega) = \varepsilon'(\omega) - j\varepsilon''(\omega) \tag{1.8}$$

At a given frequency, the imaginary part of ε^* leads to absorption loss if it is positive and gain if it is negative. Materials can be classified according to their permittivity. Those with a permittivity that has a negative real part, ε', are considered to be metals, in which no propagating electromagnetic waves exist. Those with a positive real part are dielectrics. A perfect dielectric is a material that exhibits a displacement current only, therefore it stores and return electrical energy as if it were an ideal battery. In general, the absorption of electromagnetic energy by dielectrics is covered by a few mechanisms that influence the shape of the permittivity as a function of frequency:

- **Relaxation effects** associated with permanent and induced molecular dipoles. At low frequencies the field changes slowly enough to allow dipoles to reach equilibrium before the field has measurably changed. For frequencies at which dipole orientations cannot follow the applied field due to the viscosity of the medium, absorption of the field's energy leads to energy dissipation. The mechanism of dipoles relaxing is called dielectric relaxation and for ideal dipoles is described by classic Debye relaxation.

- **Resonance effects**, which arise from the rotations or vibrations of the atoms, ions or electrons. These processes are observed in the neighborhood of their characteristic absorption frequencies.

1.4.3 Polarization Mechanisms

Polarization of a dielectric may be classified according to: electronic, atomic or ionic, and orientational polarization. Electronic and atomic polarization are temperature independent, but orientational polarization varies inversely with absolute temperature. All of these polarization mechanisms can only operate up to a limiting frequency, after which a further frequency increase will result in their disappearance. Because of the spring-like nature of the forces involved, this is accompanied by an absorption of the resonance type for electronic and atomic polarization, but for orientational polarization the disappearance, accompanied by a broader peak in the loss factor, is more gradual, because the mechanism involved is of the relaxation type, and may involve a broad distribution of relaxation times.

Electronic polarization occurs in a neutral atom when the electric field displaces the electron density relative to the nucleus it surround. A dipole moment is induced in the atom, this atom is said to be electronically polarized. All atoms present this type of polarization to different extents. It is established in a very short time and remains appreciable until the frequency exceeding that of visible light (10^{15}Hz).

Atomic or ionic polarization is observed when an agglomeration of positive and negative ions is deformed under the force of the applied field. Whether a molecule possesses a permanent dipole or not, if it has polar bonds the applied field induces a displacement; this displacement is superimposed on the electronic displacement. The charge displacement in an electric field involves changes in bond length and bond angle, in addition to bending or twisting of polar groups with respect to each other. The displacement is restricted by the degree of vibrational freedom of the molecule.

Dipole relaxation originates from permanent and induced dipoles aligned to an electric field. Their orientational polarization is disturbed by thermal noise and misaligns the dipole vectors from the direction of the field. The time needed for dipoles to relax is determined by the local viscosity. Dispersion for orientational polarization may lie anywhere within a wide frequency range (10^{-2}–10^{10} Hz) depending on the material and its temperature. These two facts make dipole relaxation heavily dependent on temperature and chemical surrounding.

Dielectric relaxation as a whole is the result of the movement of dipoles and electric charges due to an applied alternating field, and is usually observed in the frequency range 10^{-2}–10^{10} Hz. Relaxation mechanisms are relatively slow compared to resonant electronic transitions or molecular vibrations, which usually have frequencies above 10^{12} Hz. Because polarization cannot follow an electric field in a high-frequency field, permittivity has a dependence on the frequency. This dependence is called dielectric dispersion. When the frequency becomes higher it becomes impossible for dipolar polarization to follow electric field in the microwave region around 10^{10} Hz; in the infrared or far-infrared region around 10^{13} Hz, ionic polarization loses the response to electric field; electronic polarization loses its response in the ultraviolet region around 10^{15} Hz. Below ultraviolet, permittivity approaches to ε_0. The dielectric responses to different polarization mechanisms are depicted in Figure 1.7.

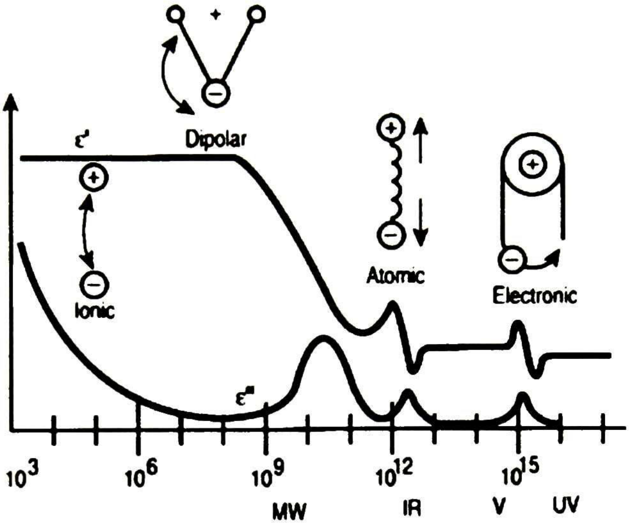

Figure 1.7: Dielectric responses as a function of frequency. Taken from [3]

In addition to these polarization mechanisms, the existence of interfacial effects such as macroscopic discontinuities in the material, or blocking at the electrodes, causes the trapping of charge carriers, and such phenomena, as well as the inclusion in the dielectric of impurities giving rise to conducting regions, result in behavior classified under the general heading of Maxwell–Wagner effects. These give rise to an effective polarization and associated loss, the frequency behavior of which is similar to that of orientational polarization, with a dispersion region which may lie in the region of 1 Hz or lower. This polarization is different from previous in which the former are all due to displacement of bound charges. This polarization takes the longest to build up: it may take several minutes or even more.

1.4.4 Simple Relaxation Theory

The molecular origins of dielectric relaxations had been established for dipolar molecular liquids and rotator-phase solids by Debye in 1929 [83]. It is a common characteristic of dielectric and other relaxation theories based on simple molecular or macroscopic models that they predict a time rate of change of polarization, or other response, which is proportional to the difference of the polarization from its equilibrium value. In such cases the complex dielectric constant is expressed by an equation of the form:

$$\varepsilon^*(f,T) = \varepsilon_\infty + \frac{(\varepsilon_s - \varepsilon_\infty)}{1 + j\omega\tau} \tag{1.9}$$

where, ε_∞ is the instantaneous permittivity, or the high-frequency permittivity; ε_s is the static permittivity, or the low-frequency permittivity; τ_0 is the relaxation time; and ω is the angular frequency.

In this equation the relaxation time, τ, is related to the kinetics of the relaxation process of the particular model and is analogous to the reciprocal of a rate constant in first order chemical kinetics. Debye obtained the equation (1.9) from his model for polar liquids or spherical polar molecules reaching equilibrium subject to Brownian diffusion and viscous damping [84].

A plot of ε_r against ε_i is termed Argand diagram, and for Debye model is plotted in Figure 1.8. This plot is also commonly know as a Cole-Cole plot. For Debye model, it is a perfect semicircle centered at $\omega RC_2 = 1$ with relaxation time equal to $\tau = RC_2$.

One disadvantage of the Argand diagram is that it is not easy to depict the behavior of ε_r and ε_i with frequency. For this reason the Bode plot is also very useful. A bode plot for ε_r and ε_i is shown in Figure 1.9, where the dielectric loss peak is symmetric about a central frequency, f_{max}.

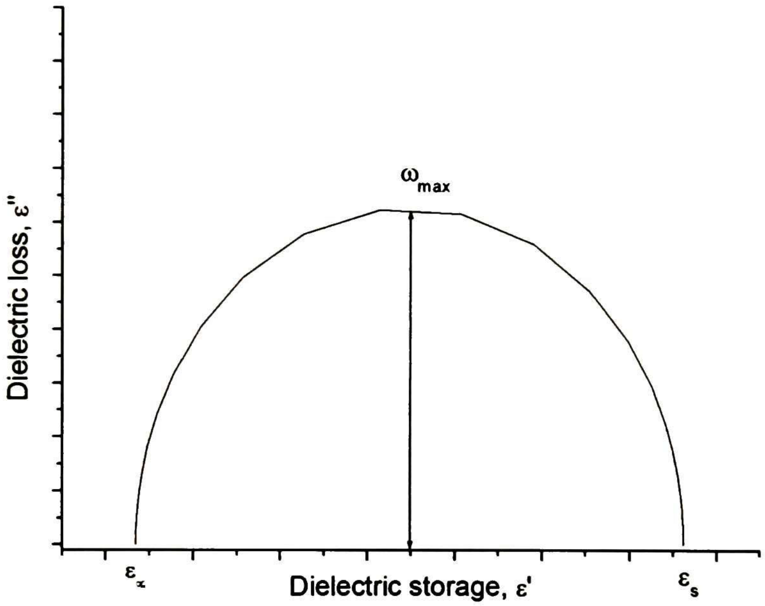

Figure 1.8: Argand plot for Debye model

The simple theory of Debye assumes that the molecules are spherical in shape and therefore the axis of rotation of the molecule in an external field has no influence in deciding the value of ε^* This is more an exception than a rule because not only the molecules can have different shapes, but —particularly in long chain polymers— they can have a linear configuration.

Further, in the solid phase, dipoles are more likely to be interactive and not independent in their response to the alternating field.

The relaxation time in such materials have different values depending upon the axis of rotation and, as a result, the dispersion commonly occurs over a wider frequency range.

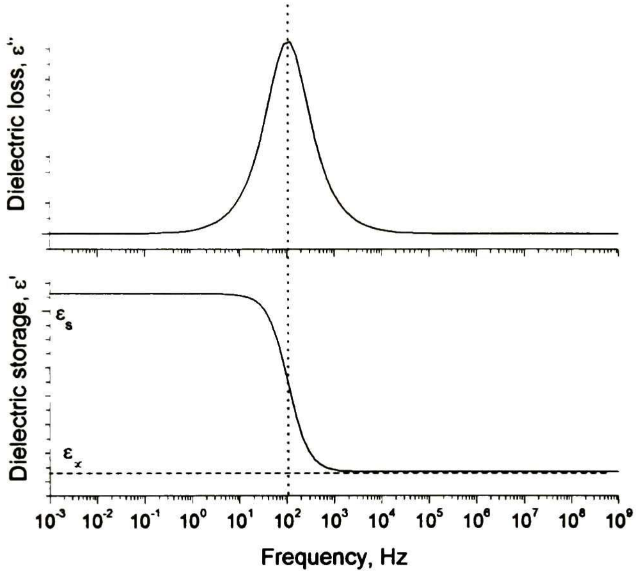

Figure 1.9: Bode plot for real and imaginary permittivity of Debye model

1.4.5 Empirical Relations for Permittivity

For dielectrics that do not satisfy Debye equations, there are several empiric equations for accounting this deviation from ideality. Some of such models are:

Cole-Cole

One of the most widely used distributions is that proposed by Cole and Cole to describe the occurrence of depressed semicircular arcs in Argand plots obtained for a wide variety of polar liquids and solids. This function gives a loss curve which is broad but symmetrical about $\log \omega\tau = 1$. The complex permittivity behavior (Figure 1.10) is described by:

$$\varepsilon^* = \varepsilon_\infty + \frac{\varepsilon_s - \varepsilon_\infty}{1 + (j\omega\tau)^{1-\alpha}} \tag{1.10}$$

where, ε_∞ is the high-frequency permittivity; ε_s is the static permittivity; τ is the mean relaxation time; ω is the angular frequency; and α is a parameter that describes the width of the material property distribution with values of $0 \leq \alpha \leq 1$.

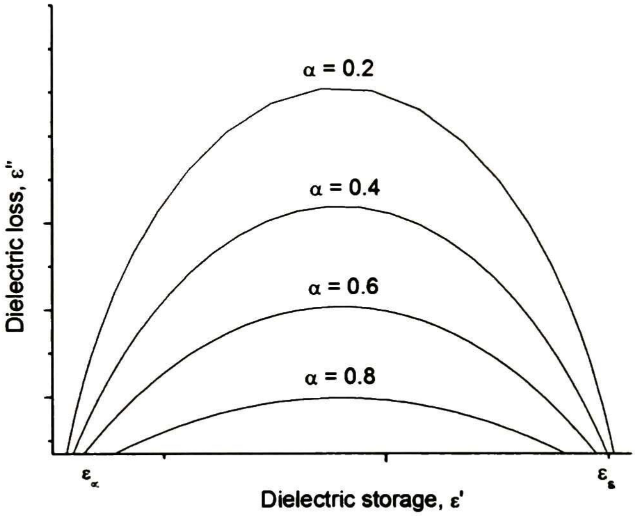

Figure 1.10: Argand plot for Cole-Cole relation. The parameter α describe the width of the material property distribution

Davidson-Cole

Some materials show a skewed semicircle in the Argand plot, for such geometry Davidson and Cole suggested the empirical equation:

$$\varepsilon^* = \varepsilon_\infty + \frac{\varepsilon_s - \varepsilon_\infty}{(1 + j\omega\tau)^{\beta}} \tag{1.11}$$

where, ε_∞ is the high-frequency permittivity; ε_s is the static permittivity; τ is the mean relaxation time; ω is the angular frequency; and β is a fractional shape parameter and $0 \leq \beta \leq 1$. The locus of Equation (1.11) in the complex plane (Figure 1.11) is an arc with intercepts on the ε' axis at ε_s and ε_∞ at the low and high frequency ends, respectively. As $\omega \to 0$ the limiting curve is a semicircle with center on the ε' axis, but as $\omega \to \infty$, the limiting straight line makes an angle of $\beta\pi/2$ with the ε' axis (skewed semicircle).

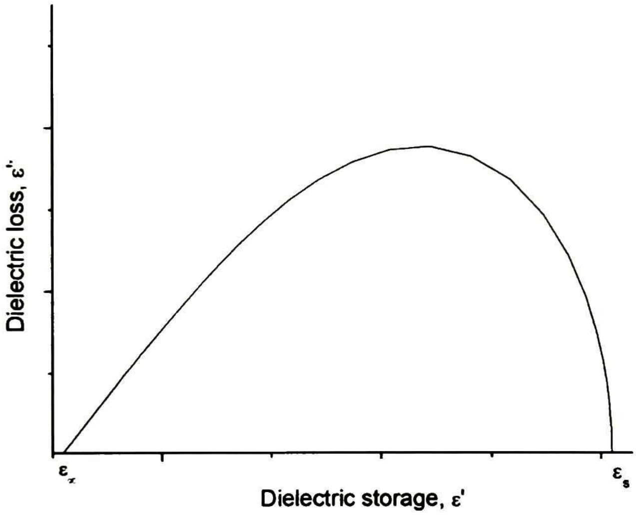

Figure 1.11: Argand plot for Davidson-Cole relation

Havriliak and Negami

Havriliak-Negami (H-N) relaxation accounts for the asymmetry and broadness of the dielectric dispersion curve. The model was first used to describe the dielectric relaxation of some polymers, by adding two exponential parameters into Debye equation:

$$\varepsilon^* = \varepsilon_\infty + \frac{\Delta\varepsilon}{[1 + (j\omega\tau)^\alpha]^\beta} \tag{1.12}$$

where, ε_∞ is the high frequency permittivity; $\Delta\varepsilon$ is the relaxation strength, and is equal to $\varepsilon_s - \varepsilon_\infty$; τ is the relaxation time; ω is the angular frequency; α and β are fitting parameters, which describe the width and asymmetry of the relaxation, respectively (Figure 1.12).

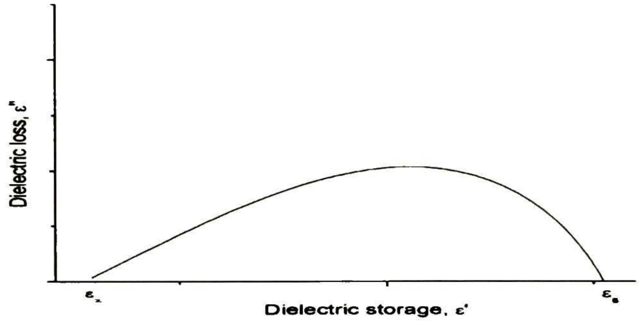

Figure 1.12: Argand plot for Havriliak-Negami relation. Here ϕ is the limiting angle related to the β parameter (skewness of the semicircle)

Furukawa *et al.* [85] used the H-N relation plus a conduction term for fitting experimental data as:

$$\varepsilon(\omega) = \varepsilon_\infty + \frac{\Delta\varepsilon}{[1 + (j\omega\tau)^\alpha]^\beta} + \frac{\sigma}{j\omega} \tag{1.13}$$

With the last expression they separate dc conduction from the relaxation mechanism.

1.4.6 Impedance Measurements

The real and imaginary parts of impedance of a dielectric is measured using an Impedance Analyzer. Impedance spectra is obtained and the Nyquist plot is conventionally plotted as $-Z''$ vs Z'. Since $\varepsilon^* = 1/(j\omega C_0 Z^*)$ [86], impedance values can be related to the permittivity using the following equivalences:

$$\varepsilon_r = \frac{Z_i}{\omega C_0 (Z_r^2 + Z_i^2)} \tag{1.14}$$

and

$$\varepsilon_i = \frac{Z_r}{\omega C_0 (Z_r^2 + Z_i^2)} \tag{1.15}$$

with $\omega = 2\pi f$ and $C_0 = \varepsilon_0 S/d$. Where C_0 is the capacitance of the empty cell; S is the contact area of the sample; and d is the thickness of the film.

1.4.7 Equivalent Circuit Approximation

A common approach for the interpretation of impedance spectra is the method of equivalent circuits, which states that a real dielectric can be represented using theoretical components, *i.e.* a capacitance in series with a resistance, or a capacitance in parallel with a resistance. Neither the series nor the parallel equivalent circuit will represent all polar dielectrics. Other equivalent circuits must be considered.

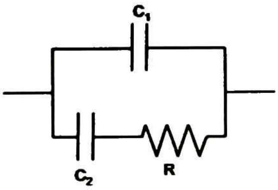

Figure 1.13: Equivalent circuit for Debye model with capacitor and resistance in parallel

For a series-parallel circuit in which a series branch having a capacitance C_2 and a resistance R is in parallel with a capacitance C_1, as depicted in Figure 1.13, the real an imaginary parts of complex permittivity are given by:

$$\varepsilon' = \varepsilon_\infty + (\varepsilon_s - \varepsilon_\infty)\frac{1}{\omega^2\tau^2} \tag{1.16}$$

$$\varepsilon'' = (\varepsilon_s - \varepsilon_\infty)\frac{\omega\tau}{1+\omega^2\tau^2} \tag{1.17}$$

These are identical with Debye Equation (1.9) providing a basis for the use of the equivalent circuit for polar dielectrics.

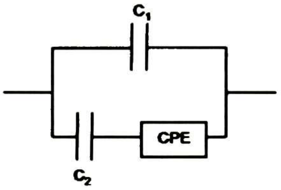

Figure 1.14: Equivalent circuit that models the Cole-Cole expression

The dielectric response corresponding to the Cole-Cole Equation (1.10) may be represented by the equivalent circuit shown in Figure 1.14, which contains a constant-phase element (CPE). The complex admittance Y^* of such circuit [86] may be expressed as following:

$$Y^* = j\omega C_1 + \frac{j\omega C_2}{[1 + C_2 A(j\omega)^{1-\alpha}]} \tag{1.18}$$

where capacitances are defined as $C_1 = \varepsilon_0\varepsilon_\infty S/d$, and $C_2 = (\varepsilon_s - \varepsilon_\infty)\varepsilon_0 S/d$; S is the contact area; d is the distance between contacts; and A is the CPE constant defined by:

$$A = \frac{\tau^{(1-\alpha)}}{(\varepsilon_s - \varepsilon_\infty)\varepsilon_0} \tag{1.19}$$

1.4.8 Temperature Dependence of Relaxation Time

When a direct voltage applied to a dielectric for a sufficiently long duration is suddenly removed the decay of polarization to zero value is not instantaneous but takes a finite time. This is the time required for the dipoles to revert to a random distribution, in equilibrium with temperature of the medium, from a field oriented alignment.

Similarly the build up of polarization following a sudden application of a direct voltage takes a finite time interval before the polarization attains its maximum value. This phenomenon is called dielectric relaxation. The relaxation time is a function of temperature according to a chemical rate process defined by [86, 87]:

$$\tau = \tau_0 \exp\left(\frac{E_{a\tau}}{RT}\right) \tag{1.20}$$

in which τ_0 is the pre-exponential factor and $E_{a\tau}$ is the energy of activation of the relaxation process, and R is the universal constant of gases equal to 8.314 J/mole. This is an Arrhenius equation. There is no theoretical basis for the dependence of τ on T. The relaxation time increases with decreasing temperature, as found in many substances. The temperature dependence of τ for the α relaxation in amorphous polymers is usually found to follow the Vogel-Fulcher-Tamman-Hesse (VFTH) equation [88]:

$$\tau = \tau_0 \exp\left(\frac{B}{T - T_0}\right) \tag{1.21}$$

where τ_0 is the pre-exponential factor, B is the activation parameter, and T_0 is the Vogel temperature closely related to the Kauzmann temperature.

The common feature of the α relaxation in amorphous polymers is that the plot of $\log f_{max}$ vs $1/T$ is strongly curved as the glass transition temperature, Tg, is approached from higher temperatures. Several theories have been proposed to account for Vogel-type behavior, and those involving free-volume concepts are prominent [89]. The secondary or β relaxations for amorphous polymers give extremely broad loss curves but τ is usually found to follow the Arrhenius Equation (1.20). The temperature dependence of τ reflects the fact that dielectric relaxation is a thermally-activated process.

1.4.9 Dielectric Loss and Conductivity

Since the effectiveness of orientational polarization is determined by the ability of the dipoles to reorient, it is dependent on the local environment. For instance, a dipole attached to a flexible chain can reorient more easily than a dipole attached to a stiff chain. Also, a dipole in a crystal will find it more difficult to reorient than a dipole in an amorphous phase. If an alternating field experiment is carried out as a function of increasing frequency, there will come a time when the dipole is unable to follow the oscillations of the field. When this occurs, dielectric losses will be generated. In addition to dielectric loss, the terms dielectric dispersion and dielectric relaxation are commonly used.

Ionic relaxation is comprised of ionic conductivity and interfacial and space charge relaxation. Ionic conductivity predominates at low frequencies and introduces only losses to the system. Interfacial relaxation occurs when charge carriers become trapped at interfaces of heterogeneous systems. Many dielectrics possess a conductivity due to motion of charges and such conductivity is usually expressed by a volume conductivity. The motion of charges in the dielectric gives rise to the conduction current and additionally polarizes the dielectric. The conductivity may therefore be visualized as contributing to the dielectric loss. Experimental ac conductivity can be calculated from measured impedance [90] data with the following relation:

$$\sigma'(\omega) = \frac{Y'd}{S} = \frac{Z_r d}{(Z_r^2 + Z_i^2)S} \tag{1.22}$$

where Y' is the real part of the admittance. The variation of the real part of ionic conductivity with frequency may be described, for a number of materials, by the universal power law:

$$\sigma(\omega) = \sigma_0 + K\omega^n \tag{1.23}$$

where σ_0 is a "dc" or frequency-independent part and the second term is of the CPE type, with K and n temperature-dependent frequency-independent material parameters. At low frequencies, a constant conductivity can be seen, but at higher frequencies a power law contribution enters.

The dc conductivity, σ_{dc}, can be obtained from two different methods: the real component of the complex conductivity measured in the very low frequency range as:

$$\sigma_{dc} = \sigma_0 f^n \tag{1.24}$$

and the exponent n was empirically found to be between 0.0 and 0.1 for amorphous materials [91]. The second method is to obtain the material bulk resistance, R_0, by fitting the semicircle of the impedance spectra [92]:

$$\sigma_{dc} = \frac{d}{R_0 S} \tag{1.25}$$

Moreover, the dielectric loss spectra are strongly modified in the low frequency range by the conductivity. The imaginary part of permittivity can be corrected using the dc conductivity as follows [91]:

$$\varepsilon''_{dc-corr} = \varepsilon''_{exp}(f,T) - \frac{\sigma_{dc}}{\varepsilon_0 \omega} \tag{1.26}$$

The σ_{dc} correction requires an accuracy of the σ_{dc} values better than 0.1% but this is out of the range of the experimental confidence. Therefore, the dc-corrected ε'' spectra have frequently shown physically incorrect behavior in the low frequency range.

1.4.10 Conductivity Dependence on Temperature

For dielectric materials, conductivity increase as temperature increase as opposed for metals. The temperature dependence of the dc conductivity can be described as Arrhenius-type as follows:

$$\sigma_{dc}(T) = \sigma_0 \exp\left(\frac{-E_{a\sigma}}{RT}\right) \tag{1.27}$$

where σ_0 is the pre-exponential factor and $E_{a\sigma}$ is an activation energy for conduction. Near the glass transition temperature, the Vogel-Tamman-Fulcher-Hesse (VTFH) equation [88] in terms of conductivity is also used to describe ionic conductivity in amorphous polymers as:

$$\sigma_{dc} = \sigma_0 \exp\left(\frac{-B}{T - T_0}\right) \tag{1.28}$$

where the pre-exponential factor, σ_0, the activation parameter, B, and the Vogel temperature, T_0, are temperature-independent empirical parameters.

1.4.11 Glass Transition Temperature in Polymers

The glass transition temperature, T_g, is defined as the temperature at which an amorphous material undergoes a transition from a highly elastic to a glassy or brittle state, and is accompanied by drastic changes in physical properties; hence, T_g, is the temperature that separates glassy behavior from rubbery behavior and many amorphous solids, including polymers, organic liquids, biomaterials, some metals and alloys, and inorganic oxide glasses, exhibit glass transition temperatures. The drastic change in the local motion of polymer chains at T_g leads to large changes in some physical properties like: density, specific heat, mechanical modulus, dielectric constant, elastic moduli, *etc.*

It is common to associate the α-relaxation in dielectric measurements with the glass transition. The VFTH equation describes the behavior of polymer near glass transition temperature and in many polymers T_0 is usually 50 K lower than T_g [93, 94, 95].

Chapter 2

Objectives

Supercritical fluids processing is a very interesting and promising technique for producing novel materials, specially those related to the biomedical area. Among these materials, chitin and chitosan have promising applications for such area. This work is a fusion of both —promising biopolymer and novel technique— for generating useful biomaterials. To the best of our knowledge, there are very few successful attempt for processing those polysaccharides with supercritical fluids techniques [96, 97]. Two main objectives are pursued within this work, one in the processing field and another of fundamental interest. The fist one is related to the processing of chitin nano-fibers using supercritical carbon dioxide ($SCCO_2$); the second one deals with the use of Impedance Spectroscopy (IS) for studying thermal relaxations on chitosan films.

2.1 Chitin Nano-fibers Processed by Supercritical Carbon Dioxide

There are few reports of biopolymers processed with supercritical fluids. The fabrication of a $CaCO_3$-biopolymer thin film have been reported [98], where chitosan or cellulose thin films were prepared at room temperature by spin coating and impregnated later with calcium acetate in the presence of $SCCO_2$ yielding composite films of high uniformity. Supercritical carbon dioxide has also been used as media for polymer modifications; chitosan was reacted with glucose or malto-oligosaccharides yielding a water soluble, imine-linked, branched chitosan derivative [97]. Some biopolymers like dextran, poly-L-lactide (PLLA), and poly-(hydroxypropylmethacrylamide) (HPMA) were successfully micronized using carbon dioxide as anti-solvent with dimethylsulfoxide (DMSO) and dichloromethane (DCM) as liquid solvents [99]. Hirokazu *et al.* [96] used supercritical anti-solvent (SAS) to produce chitosan powder for pulmonary gene delivery.

However, so far, chitin has not been precipitated by supercritical solvent, again mainly because of the chitin insolubility issues. Recently, HFIP solvent was found to be suitable for SAS process while processing insulin [100]. Fortunately this HFIP solvent can dissolve chitin to some extent. Hence, chitin/HFIP solution can be used for SAS process.

On the other hand, electrospinning has been used to produce chitin and chitosan nano-fibers. Min *et al.* [101] produced chitin nano-fibers with an average diameter of 110 nm with a broad fiber diameter distribution. Spasova *et al.* [102] prepared chitosan/Polyethylene oxide nano-fibers with diameters that ranged from 40-290 nm. Materials having a structure in the nanometer range exhibit properties significantly different from those for the same material with larger grain sizes, as to say, incremented contact area and hence, bioadhesion.

63 °C [108];102 °C [109]; 140-150 °C [110];161 °C [111]; 170 °C [112]; 203 °C [113]; and even to be higher or equal to 220 °C [114].

Second Main and Secondary Objectives

For that reason, the second objective of this work is to elucidate the molecular mechanism related to chitosan's film thermal relaxations using impedance spectroscopy; and to propose, whether or not, these relaxations can be related with a glass transition temperature. Experimental details are provided in section 3.2, while results are discussed in section 4.2.

For achieving this task, proposed secondary objectives are:

1. To develop a method for preparation chitosan films .
2. To get training in impedance measurements.
3. To evaluate the effect of contacts.
4. To evaluate the dc conductivity plot.
5. To fit the impedance spectrum with an equivalent circuit.
6. To evaluate the relaxation time of the low frequency relaxation.
7. To propose a relaxation mechanism.
8. To elucidate if this relaxation can be related to the T_g.

In the following chapter, experimental details are provided in order to achieve the stated objectives.

3.1.2 Chitin Purification

Chitin purification requires removal of proteins and minerals. Detailed procedure is described in the Standard Method 12-SM-001 of Appendix B.1 based on different purification methods [115, 20, 53, 116, 117, 36, 118]. Briefly, in order to remove minerals, 90 g chitin were soaked for 24 hours with 0.5 liter HCl (2 N) at 10 °C. This mixture was then rinsed with distilled water until neutral pH was obtained. To remove proteins, the rinsed chitin from previous step was added to 1 liter NaOH (2.5 N) and stirred at 90 °C for 2 hours. This mixture was then rinsed with distilled water until neutral pH was obtained and then dried in a vacuum oven. Ash tests were performed on raw chitin, demineralized chitin, and demineralized-deproteinized chitin with the following purities: 96.7%, 99.2%, and >99.2%, respectively. Purified chitin was stored at room temperature until used.

3.1.3 Chitin Dissolution

Chitin was mixed in HFIP to obtain either a 2.0 mg/mL or a 4.0 mg/mL concentration, and then stirred for 48 h. After this period most of the chitin was dissolved, except a small amount, which was filtered through a 0.2 micron PTFE syringe filter before using in SAS process.

3.1.4 Phase Behavior Measurements

Phase behavior of CTN/HFIP/$SCCO_2$ is analyzed using a high pressure variable volume cell with piston coupled with a light scattering measuring system. The anti-solvent effect of $SCCO_2$ is evaluated for the ternary system at 40 °C and 103.4 bar. Concentrations of chitin in HFIP solvent used were 2.0; 5.0; 10.0; and 15.0 mg/mL. The procedure consists in the following: the solution at a specific concentration is charged into the view cell (40 mL) along with a small stir bar. Typical volume used is 5-7 mL. The view cell is closed, connected to the pressure transducer (SENSOTEC, model TJE) and to the high pressure manual syringe pump (HIP, model 87-6-5) and placed into a water bath in which temperature is controlled within ±0.1 °C, by means of an immersion circulator (POLYSTAT, model U12112). The variable volume view cell is equipped with three sapphire windows: one at front and two laterals aligned at 90° The light scattering measuring system is connected to the view cell using optical fibers into the lateral windows. The light source is a Deuterium-Tungsten-Halogen lamp (OCEAN OPTICS, model DT-1000) and detector is a photosensor that converts the signal into voltage, which is measured with a voltmeter.

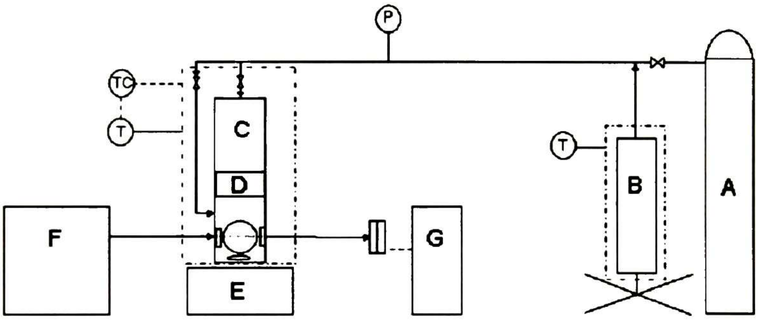

Figure 3.1: Schematic for cloud point measurement in CTN/HFIP/$SCCO_2$ system.

$SCCO_2$ is now introduced into the back chamber of the view cell, the purpose of this chamber is to pressurize the front chamber, where solution was initially charged, until the desired pressure. At this point, pressure is set to 103.4 bar and temperature to 40 °C. The system is left at this conditions for 2 h in order to equilibrate it. After this, $SCCO_2$ is introduced very slowly into the front chamber of the view cell to a fixed amount. The precise amount is calculated using volume and density. The volume is measured using a calibrated scale attached to the manual syringe pump, and density is calculated at P and T of the pump with the program CO2PAC, which uses Wagner's equation of state [119]. After CO_2 is added to the solution, pressure increases slightly. The back stage of the view cell is now slightly depressurized until the set point is reached again. After 1-2 h the system reaches equilibrium again and voltage and CO_2 amount added to the solution are recorded. A small amount of CO_2 is added again and the procedure is repeated. The mixture is kept stirred at all times by means of a magnetic stir bar. The experimental measurement was done twice for repeatability, and experimental error is calculated to be ±2.0% of CO_2 concentration. A schematic and a photograph of the view cell for phase behavior measurements is shown in Figures 3.1 and 3.2.

Figure 3.2: Experimental setup for phase behavior measurements. Variable volume high-pressure cell (inside water bath), fiber optic lines (blue cables), visible light source (at center), and photosensor with voltmeter (not shown)

3.1.5 Apparatus and Procedure at Auburn University

A schematic and a photograph of the SAS apparatus used to produce the chitin fibers are shown in Figures 3.3 and 3.4. Using a syringe pump (ISCO 500D), the vessel (100 mL) is filled with CO_2 from the tank and pressurized to the desired pressure, which is measured using a pressure transducer (Heise ST-2H) connected directly to the vessel.

The vessel is heated by means of a heating tape and temperature is controlled with a temperature controller (Barnant) using a type K thermocouple inserted into the vessel. Once the system is in equilibrium, the backpressure regulator (TESCOM 44100) is opened to allow CO_2 to flow through the system while the flow rate of CO_2 is being maintained by the syringe pump. Once the system is equilibrated and CO_2 is flowing, the chitin/HFIP solution is injected by means of an injection device. The injection device is a small piston-cylinder assembly (HIP) with silicone O-rings. The solution is taken in one side of the device, then water is pumped into the other side using a hand pump (HIP). The solution is injected into the vessel using a 50-cm long silica-capillary tubing (Upchurch) of 100-μm inner diameter.

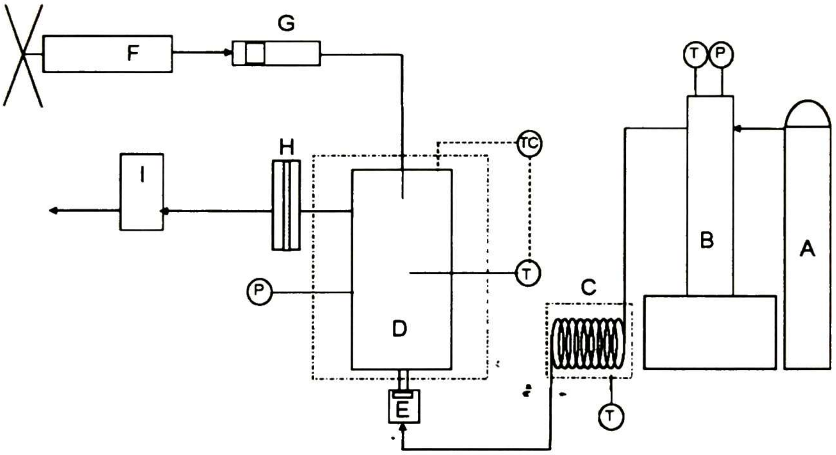

Figure 3.3: Schematic for SAS apparatus showing (A) CO_2 tank, (B) syringe pump, (C) preheating coil, (D) precipitation vessel, (E) 0.5 micron stainless steel frit, (F) manual syringe pump, (G) injection device, (H) high pressure filter holder, and (I) backpressure regulator

When the solution injection is completed, the solution inlet line is closed and CO_2 is kept flowing for purging step. A 0.5-μm stainless steel frit (Valco) situated in the CO_2 inlet line and a 0.2-μm PTFE filter (Millipore) in the CO_2 outlet line are used to collect the particles/fibers formed during the process; however, the material formed is fibrous and tend to agglomerate, almost nothing will be carried out to the filter. The PTFE filter is kept inside of a high pressure filter holder (Millipore). After the vessel is purged with a sufficient quantity of CO_2, the CO_2 feed is closed and the vessel is allowed to depressurize slowly. Finally, the vessel is opened to harvest the product. In these SAS experiments, temperature was set to 40 °C and pressure to 103.4 bar. Enough CO_2 flow was used to ensure a single phase (supercritical), and this was verified experimentally performing one experiment injecting 5.0 mL only of HFIP solvent (which is the maximum quantity of solution injected). The HFIP/CO_2 mixture is formed a single phase.

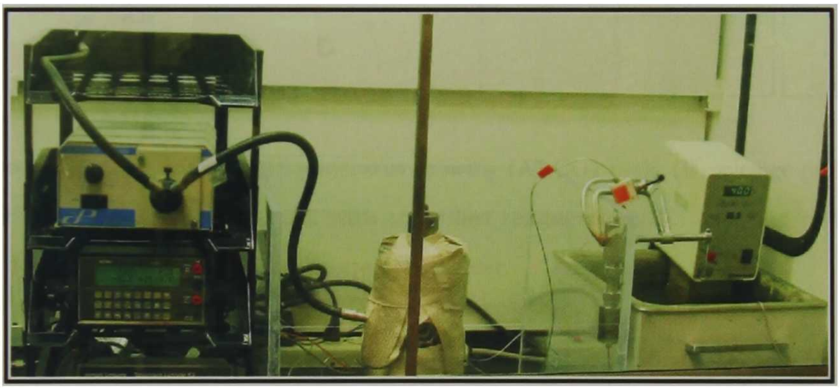

Figure 3.4: Photograph of the apparatus used for SAS process at Auburn University

3.1.6 Apparatus and Procedure at Cinvestav-Querêtaro

A schematic and a photograph of the SAS apparatus used to produce the chitin fibers is shown in Figures 3.5 and 3.6. Using a syringe pump (ISCO 100D), the view cell (40 mL) is filled with CO_2 from the tank and pressurized to the desired pressure, which is measured using a pressure transducer (SENSOTEC TJE/7039-01TJG) connected directly to the view cell, which is immersed in a water bath and the temperature is set by a immersion circulator. Once the system is in equilibrium at the desired conditions, the outlet valve is opened to allow CO_2 to flow through the system while the flow rate of CO_2 is being maintained by the syringe pump.

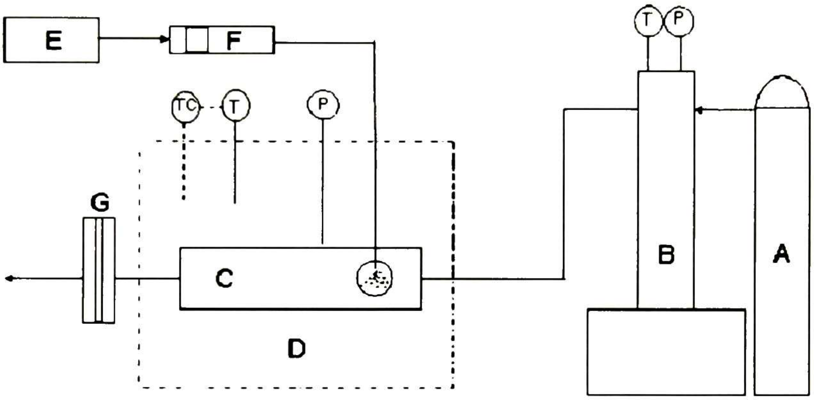

Figure 3.5: Schematic for SAS apparatus showing (A) CO_2 tank, (B) syringe pump, (C) precipitation cell, (D) water bath with controlled temperature, (E) metering pump, (F) injection device, and (G) high pressure filter holder

Once the system is equilibrated and CO_2 is flowing, the chitin/HFIP solution is injected by means of an injection device. The injection device is a small piston-cylinder assembly (HIP) with silicone O-rings. The solution is taken in one side of the device, and water is pumped into the other side using a metering pump (Lab Alliance). The solution is injected into the vessel using a 25-cm long silica-capillary tubing (Upchurch) of 100-micron inner diameter. When the solution injection is completed, the solution inlet line is closed and CO_2 is kept flowing for the purging step. A 0.2-μm PTFE filter (Millipore) in the CO_2 outlet line are used to collect the particles/fibers formed during the process. The PTFE filter is kept inside of a high pressure filter holder (Millipore). After the vessel is purged with a sufficient quantity of CO_2, the CO_2 feed is closed and the vessel is allowed to depressurize slowly. Finally, the vessel is opened to collect the product. In these SAS experiments, temperature was set to 40 °C and pressure to 103.4 bar. Three different injection velocities were performed (0.1; 1.0; and 10.0 mL/min) in order to evaluate different morphologies.

Figure 3.6: Photograph of the apparatus used for SAS process at Cinvestav-Querétaro

3.1.7 Chitin Nano-fibers Characterization

To characterize the obtained product, morphology analysis and FTIR and XDR measurements were performed.

Morphology Analysis

Size and morphology of the obtained fibers was examined by scanning electron microscopy (SEM) either with a Zeiss, model DSM 940 or a Phillips ESEM XL30.

Samples were sputter-coated with gold for 2 or 4 min prior to SEM analysis and the operating voltage in SEM was variated between 10-30 kV. Transmission electron microscopy (TEM) using a JEOL microscope model 2010-F, equipped with an EDS unit, was also employed. Samples for TEM were dispersed in acetone. For the analysis of macro-structure, an optical microscope (Microscope-Depot, model A Trinocular Microscope) was also used.

Infrared Measurements

Chemical analysis of the fibers was performed by Fourier-transform infrared spectroscopy (FTIR) either on a Perkin Elmer spectrophotometer model Spectrum GX, equipped with a KBr beamsplitter and a DTGS detector. Spectra were obtained using an ATR accessory in the range 4000-650 cm^{-1}, resolution was set to 4 cm^{-1} and the spectra shown are an average of 32 scans.

X-Ray Diffraction Measurements

Crystal structure analysis was performed using a 2100-Rigaku diffractometer, equipped with the CuK_α radiation ($\lambda = 1.5406\ \mathring{A}$) in the 2θ range from 5 to 50 degrees, at ambient temperature and operating at 30 kV and 16 mA.

3.2 Chitosan Thermal Relaxations

3.2.1 Chitosan Film Preparation

Chitosan low molecular weight (Mw=150,000 g/gmol) was purchased from Fluka. The manufacturer reported 1.2% of ash content and 96% degree of deacetylation. Acetic acid was purchased from J.T. Baker. Both were used as received without further purification. Detailed procedure for chitosan film preparation is given in Appendix B.2. Briefly, chitosan was dissolved in diluted acetic acid (1.0 vol %) to prepare a 1.0 % w/v solution. This solution was magnetically stirred for 2 h to promote dissolution. Films were prepared by the solvent cast method by pouring the solution into a plastic petri dish and allowing the solvent to evaporate at 60 °C. The resultant films were further neutralized in NaOH 0.1 M for 10 minutes, washed thorouhgly with distilled water until neutral pH, and re-dried at 60 °C.

3.2.2 Electrode Preparation

A thin layer of gold was sputter-coated onto both surfaces to serve as electrodes, using a Sputtering device (Plasma Sciences Inc.) with a gold target (Purity 99.99%) and Argon as gas carrier. Pressure of gas was set to 30 mTorr and voltage was set to 0.2 kV. Sputtering time was 4 minutes onto each surface.

Samples of these films were cut into rectangular pieces. Contact area and thickness were measured with a digital calibrator (Mitutoyo) and a micrometer (Mitutoyo), respectively

3.2.3 Chitosan Films Characterization

The solvent-cast films were analyzed for thermal relaxations using Thermal Analysis and Impedance Spectroscopy.

Thermal Measurements

Thermogravimetric curves were obtained using a Mettler Toledo apparatus, model TGA/SDTA 851e, using a sample mass of *ca.* 3 mg and an aluminum sample holder under argon or nitrogen atmosphere with a flow rate of 75 mL/min. Heating rate was set to 5 °C/min. Differential scanning calorimetry measurements were performed in a Mettler Toledo DSC 822e calorimeter, using a sample mass of *ca.* 3-4 mg. Heating rate was set to 10 °C/min and standard aluminum pans were used within a nitrogen atmosphere flowing at a rate of 80 mL/min. An empty pan was used as reference. First and second scans are shown here.

Impedance Measurement

The impedance spectrum was obtained with different equipments. In the frequency range from 0.1 Hz to 1 MHz with 500 mV amplitude, impedance was measured using an Impedance/Gain-Phase Analyzer SI 1260 from Schlumberger with an Impedance Interface 1294 from Solartron. In the frequency range from 100 Hz to 110 MHz impedance was measured with an Agilent Precision Impedance Analyzer 4294 A using an amplitude of 100 mV.

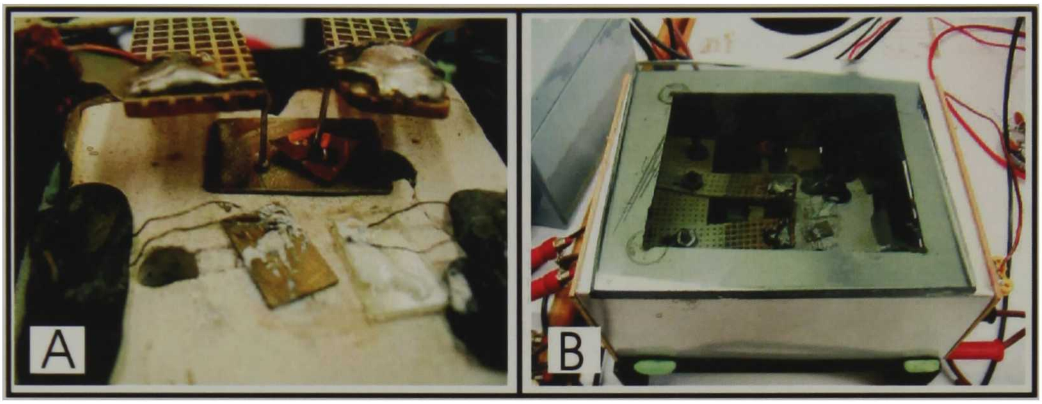

Figure 3.7: Impedance measurement furnace pictures: closed (A) and open (B), where chitosan film placed between electrodes can be seen

Temperature was varied in the frequency range 0.1 to 110 MHz using a home-made furnace (Figure 3.7, with an accuracy of ±1.0 °C, in the range from 25 to 250 °C. The temperature was controlled with a Watlow's Series 982 microprocessor-based, with ramping controller. The sample was left for 5 min at each temperature to ensure thermal equilibrium. The results of impedance measurements were analyzed using the ZView©Electrochemical Impedance Measurement Software version 2.2.

Chapter 4

Results and discussion

Since two main objectives are proposed in this work, results are presented in different sections. Section 4.1 accounts for chitin nano-fibers production using supercritical carbon dioxide. For chitosan thermal relaxations, results and discussion are presented in section 4.2.

4.1 Chitin Nano-fibers by SAS

After purification, chitin is a brown-yellowish flaky material. These flakes are very difficult to grind in the mortar due in part to its high crystallinity. The size of purified chitin flakes prior to solution preparation is about 0.2 – 1.3 mm. In Figure 4.1 a micrograph and optical picture are presented.

Dissolution of chitin is not easily achievable. First, HFIP solvent is added to purified chitin and stirred for several hours. After that, some insoluble particles remain in suspension and it is necessary to filtrate or centrifuge the solution. Viscosity of final solution strongly depends on chitin concentration. Dilute solutions (2.0 mg/mL)

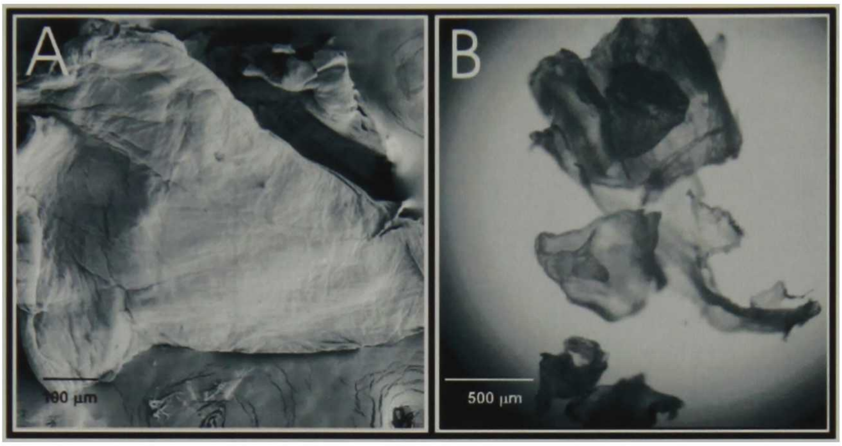

Figure 4.1: Scanning electron micrograph (left) and optical picture (right) of a purified chitin flake

form a transparent and low viscous homogeneous solution, while concentrated solutions (10.0 mg/mL) are very viscous and turbid.

4.1.1 Phase Behavior Measurements

Phase behavior of the ternary system CTN/HFIP/$SCCO_2$ requires cloud point measurements. When a polymer-solvent solution is kept in a homogeneous phase by mechanical stirring at constant pressure, the coexistence curve will be reached —the solution will become turbid— if temperature is lowered. This condition indicates phase separation. This point is known as the "cloud point", and the solution becomes turbid due to light dispersion because of the different refractive index in each phase. If mechanical agitation is stopped, macroscopic phase separation will occur. In a similar fashion, cloud point can be measured by changing solution concentration and maintaining the solution at constant pressure and temperature. Using a light scattering apparatus, the cloud point can be easily detected since an increase in turbidity will be reflected as a decrease in the intensity of the transmitted light.

Figure 4.2 shows the voltage variation as a function of $SCCO_2$ concentration in the ternary system CTN HFIP $SCCO_2$.

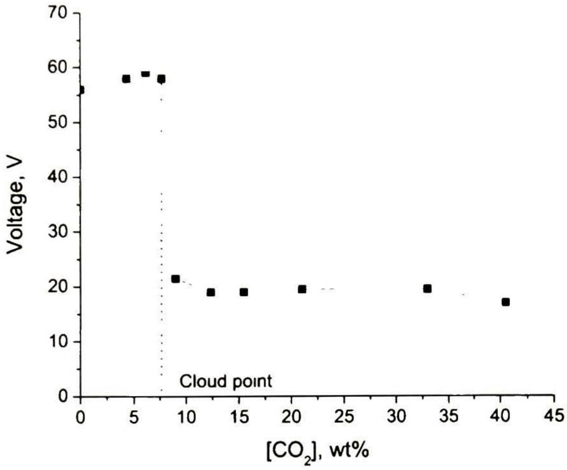

Figure 4.2: Voltage dependence with $SCCO_2$ concentration. The abrupt change in voltage indicates the cloud point

The voltage has a dramatic change at the cloud point, and the slope of the curve changes. Different solution concentrations of chitin in HFIP were used (2.0; 5.0; 10.0; and 15.0 mg/mL), the voltage change versus $SCCO_2$ concentration is plotted and the cloud point calculated.

Figure 4.3 shows a ternary diagram and it is constructed at constant pressure and temperature by plotting the concentration points at which phase separation occurs (cloud point).

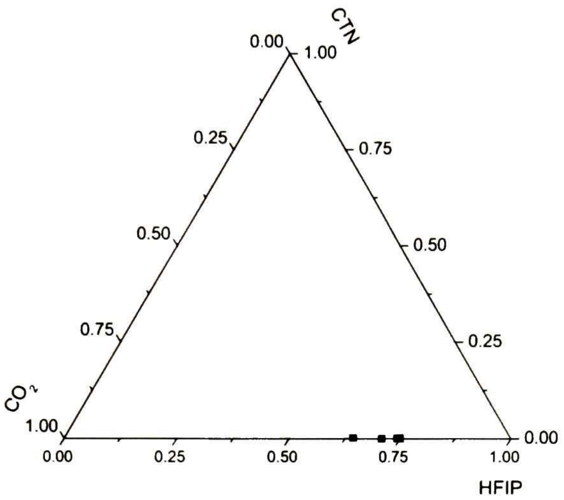

Figure 4.3: Ternary diagram for the system CTN/HFIP/$SCCO_2$ at 40 °C and 103.4 bar

As a result the phase diagram of the ternary system can be plotted at 40 °C and 103.4 bar. However, chitin concentration is very low, hence the points fall in the binary axis HFIP/CO_2.

For clarity, the phase behavior is plotted as a binary system: CO_2 concentration (g) in the y-axis versus chitin concentration in the initial solution (mg/mL). This can also be regarded as an equilibrium curve. Below this curve, the system exists as one homogeneous phase and above the curve, there are two phases. Anti-solvent precipitation requires the system to be in the two-phase region, which is easily achievable since the vessel is initially filled with CO_2, and it is kept flowing during the injection (semi-continuous mode). For the SAS experiments solution concentrations were 2.0 or 4.0 mg/mL. If CO_2 concentration is kept above 15 wt%, anti-solvent process will occur.

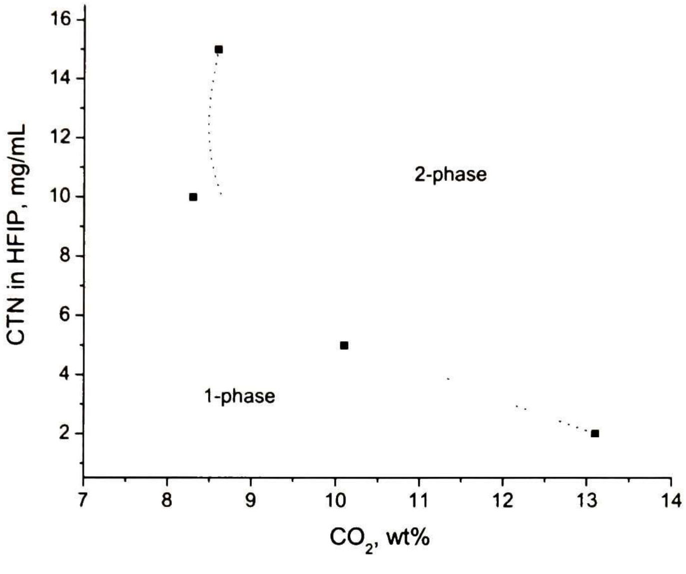

Figure 4.4: Phase diagram for binary system (CTN-HFIP)/CO_2 at 40 °C and 103.4 bar. Dotted line is a guide to the eye

4.1.2 SAS-Processed Chitin

When the chitin/HFIP solution is injected into supercritical carbon dioxide, a fast precipitation of chitin in fiber form occurs. Most SAS processing of organic materials yields precipitate in the particulate form. However in the present case, due to strong intra-molecular H-bonding in chitin, fibers were obtained. The material obtained is white-yellowish (Figure 4.5), extremely fluffy and very light with an estimated bulk density of about 0.01 g cm^{-3} When handling with tweezers, the fibers appear to be sticky.

Similar characteristics were found for the material obtained at Cinvestav-México using the same method The material is very light, and difficult to handle due to high adhesion. A photograph of these fibers is shown in Figure 4.6.

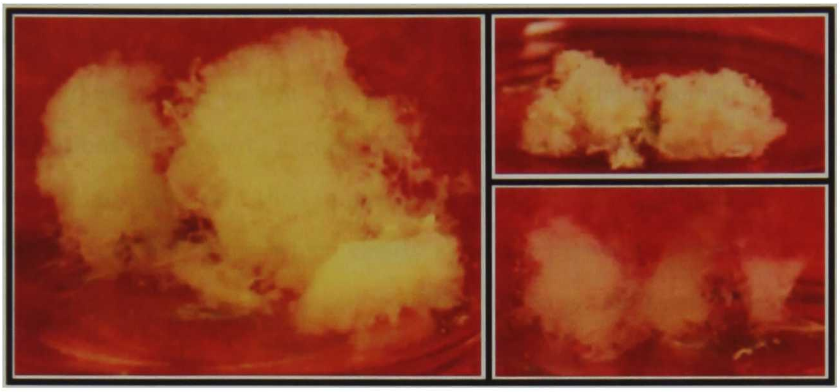

Figure 4.5: Fibrous chitin SAS-processed at Auburn University

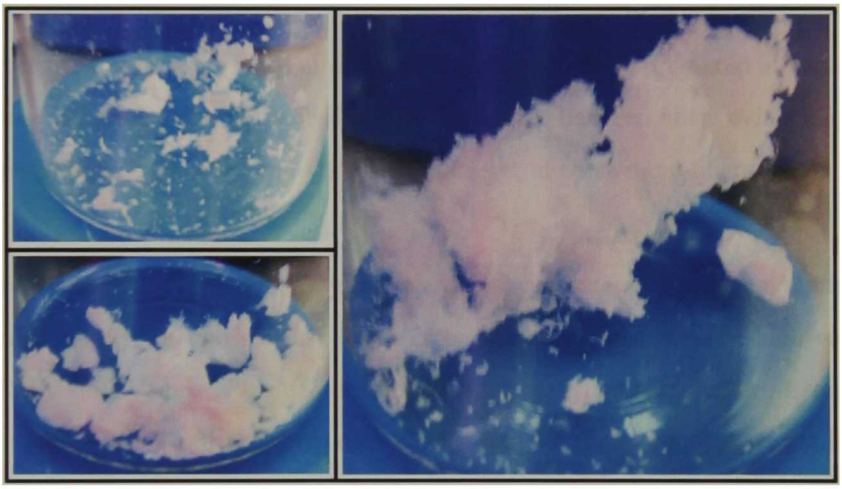

Figure 4.6: Fibrous chitin SAS-processed at Cinvestav-Querétaro

4.1.3 Morphology

Figure 4.7 shows scanning electron micrographs of the chitin fibers processed at Auburn University at different magnifications. At 50× magnification (Figure 4.7a) micro-structure of the material can be seen. The diameter of these fibers is around

50-80 μm which is of the order of the diameter of the nozzle (100 μm) used for the solution injection. To look at the actual structure in the nanometer range higher magnifications are needed. Figure 4.7b and 4.7c show that each fiber is composed of many small fibers or a three-dimensional fibrous network. Figure 4.7d and 4.7e are 20000× magnifications which clearly show the presence of nano-fibers. Figure 4.7f, at 30000× magnification, again confirms that resultant nanostructure of chitin fibers after processing the biopolymer with SAS. The diameters of about two hundred fibers in Figure 4.7e and Figure 4.7f were manually measured. The average diameter was found to be 84 nm with standard deviation of 26 nm.

Microphotographs using TEM at different magnifications are presented in Figure 4.8. In those images is possible to observe the open space between fibers evidencing high surface area and porosity, and the small diameter of these nano-fibers.

Transmission Electron Microscopy is not an ideal characterization technique for this material mainly for two reasons: (a) this technique requires of very high voltages (typically 100 kV) provoking degradation of the biopolymer sample during measurement; and (b) the resultant three-dimensional nano-fibrous structure cannot be well appreciated since this transmission technique provide the projection of the sample. The projection of a three-dimensional set of fibers will not provide information over the individual fiber.

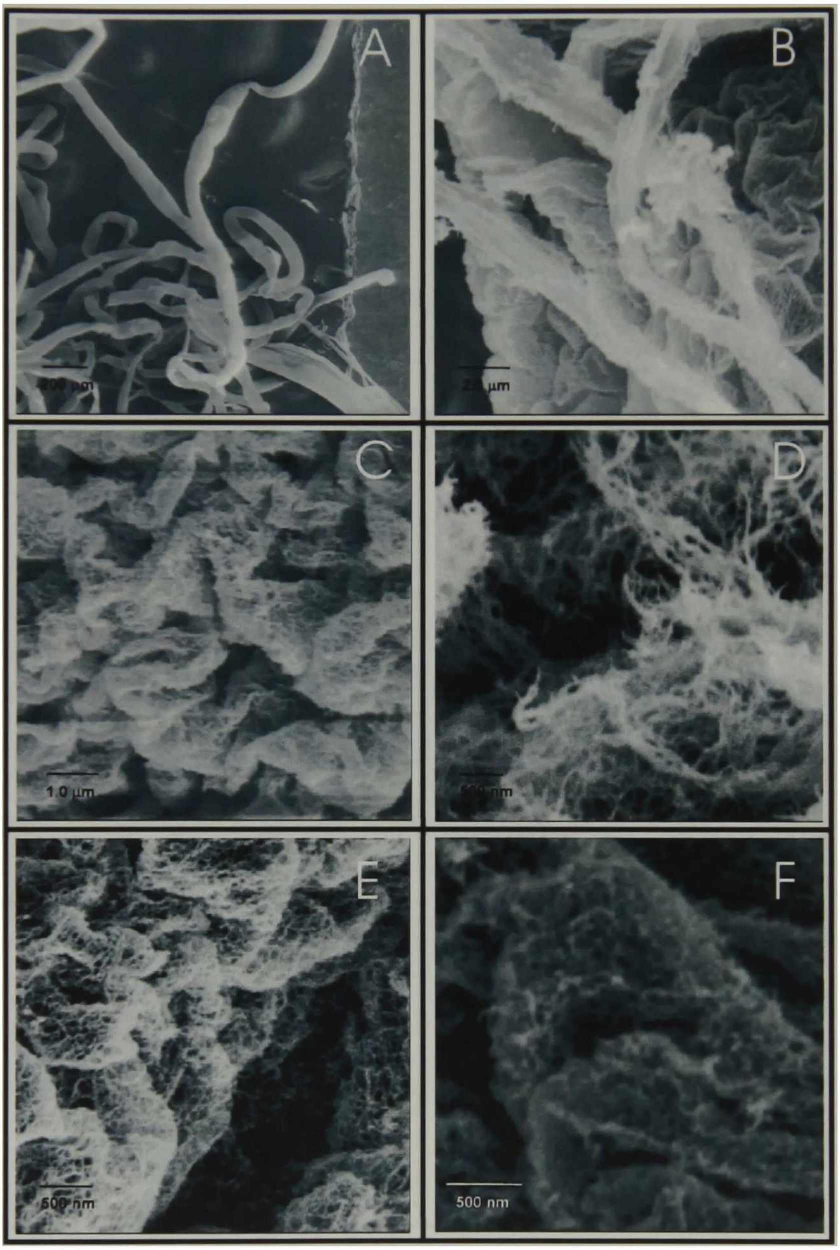

Figure 4.7: Scanning electron micrographs of SAS-processed chitin at Auburn University

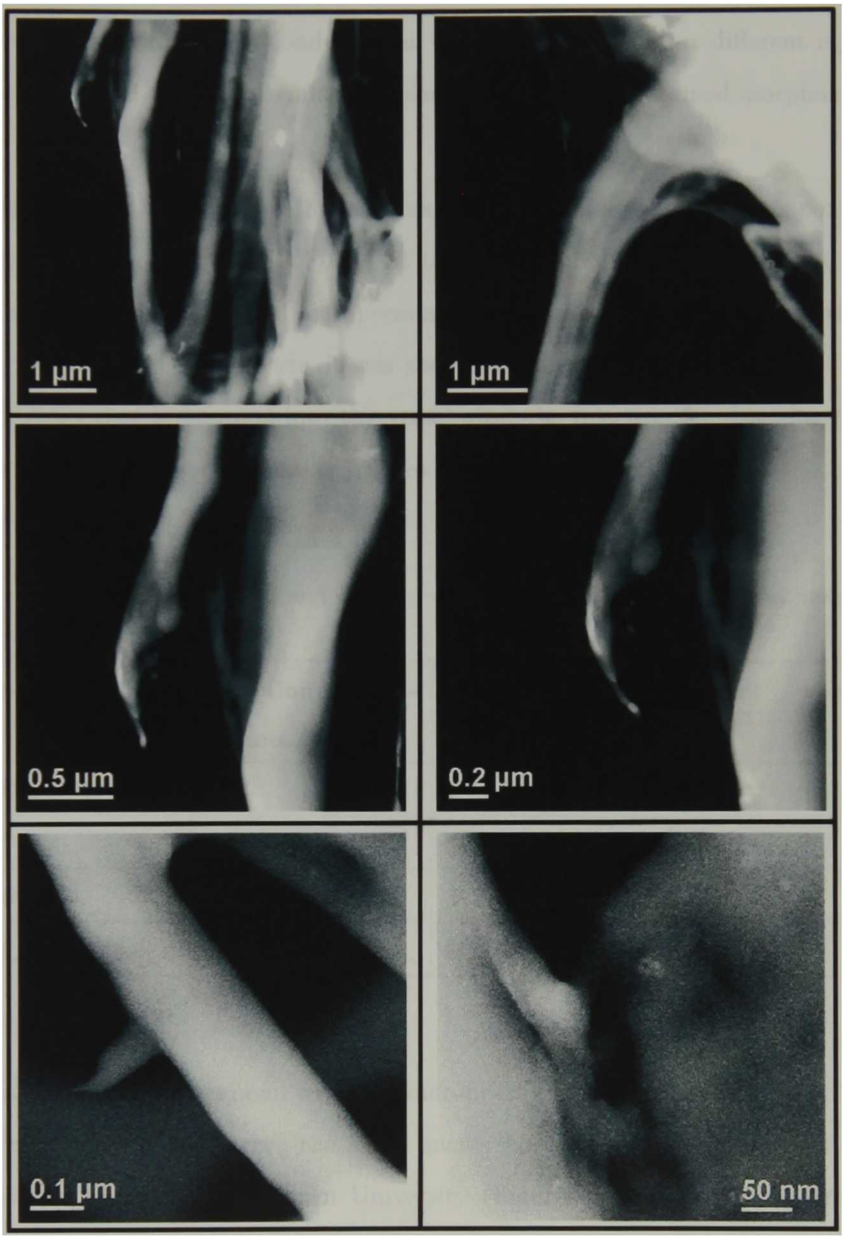

Figure 4.8: Transmission electron micrographs of SAS-processed chitin

The same experiment was conducted at Cinvestav-Querétaro at different injection velocities (0.1, 1.0, 10.0 mL/min) in order to evaluate the obtained morphology.

Table 4.1 lists the conditions for each experiment. Injection velocity is controlled using a metering pump for CNF01, CNF10, CNF100. Solution injection for CNFAU was achieved using a manual high pressure pump, and controlling the injection velocity was not precise, however, it was about 1.0 mL/min. Washing volumes means the $SCCO_2$ that is pumped into the vessel after the injection for dragging the organic solvent. A rule of thumb is 7 times the volume of the vessel.

Table 4.1: Injection velocities and washing volumes for SAS-processed chitin nano-fibers (CNF)

Experiment label	**Injection velocity, mL/min**	**Washing volumes**	**Vessel volume, mL**
CNF01	0.1	7	40
CNF10	1.0	5	40
CNF100	10.0	3	40
CNFAU	1.0	7	100

Figures 4.9A 4.9B correspond to chitin nano-fibers injected at 0.1 mL/min (CNF01) and it is possible to observe the same micro- and nano-structure of those chitin nano-fibers processed at Auburn University (Figures 4.7A and Figure 4.7E). At 100× magnification (Figure 4.9A), the fibers micro-structure is seen with diameters around 50-80 micron. Again, each of these fibers is formed of a nano-fibrous three dimensional network (Figure 4.9B).

For chitin fibers injected at 1.0 mL/min (CNF10) a transversal view of a fiber is shown in Figure 4.9C at 1000×, where is evident that the micro-fiber is not solid but porous. Figure 4.9D shows the nano-structure.

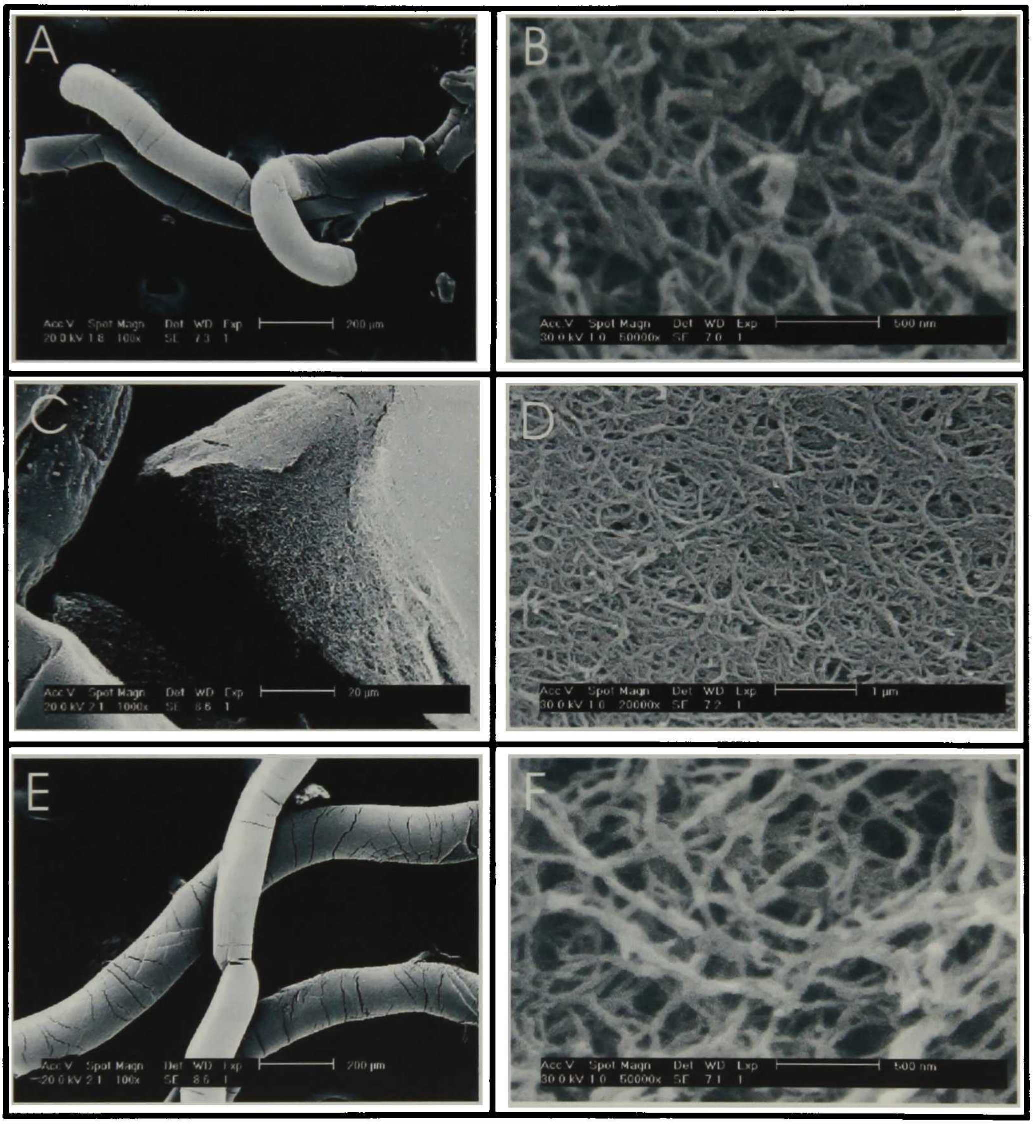

Figure 4.9: Scanning electron micrographs of SAS-processed chitin at Cinvestav-Querétaro

For chitin fibers injected at 10.0 mL/min (CNF100) the micro- and nano-structure are presented in Figures 4.9E and 4.9F. Injection velocity does not affect the morphology of the fibers.

The fine nano-structure of the obtained chitin fibers can be attributed to the strong inter- and intra-molecular H-bonding. The molecular structure of chitin (Figure 1.1) has plenty of h-bonding sites which is also evident by the infrared spectra. In addition, for the nano-scale materials, the van der Waals attraction also become significant; this may be reason for very sticky nature of the obtain fibers as compared to the original chitin. To further examine if the SAS processing resulted in any chemical alteration, infrared spectra were taken from the nano-fibers and compared to the original (purified) chitin.

4.1.4 Infrared Analysis

Figures 4.10-4.12 present the infrared spectra for raw (purified) chitin and chitin nano-fibers obtained at Auburn University. In Figure 4.10 the spectra in the region 3800-2600 cm^{-1} is shown. For purified chitin the band centered at 3433 and the shoulder at 3480 cm^{-1} are typical for α-chitin [120, 35] and are assigned to the stretching vibration of hydrogen bonded -OH groups. These bands correspond to two populations of CH_2OH groups respectively, one half forming inter-molecular hydrogen bonds with OH-6 groups of the neighboring chain, and the other half forming intra-molecular hydrogen bonds with the C=O groups of the next monomer along the same chain [35]. Nano-fibers shows a broad shoulder at 3436 cm^{-1} which coincides with the reported 3444 cm^{-1} ($\pm 10cm^{-1}$ band for β-chitin, and suggest the absence of inter-molecular hydrogen-bonds, and the existence only of intra-molecular hydrogen-bonds.

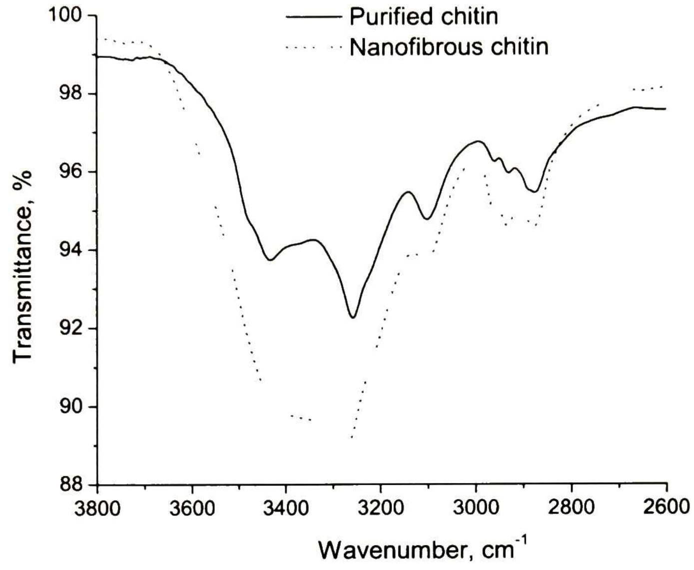

Figure 4.10: Infrared spectra for chitin nano-fibers and purified chitin (raw material) in the 3800 to 2600 cm^{-1} region

The asymmetrical and symmetrical stretching of -NH groups are centered at 3258 and 3103 cm^{-1}, respectively [120]. Interestingly, the Bellamy-Williams[121] relationship for these bands, do not hold true in this case, since it relates the asymmetric and symmetric stretching of NH_2 groups in which the two NH bonds are equivalent. It is reported that, in the solid state, the NH stretch of N-monosubstituted amides gives rise to a strong band near 3300 cm^{-1} and a weaker band near 3100 cm^{-1} the latter due to an overtone of the 1550 cm^{-1} band [121]. In α-chitin, the band at 3258 cm^{-1} is displaced 42 cm^{-1} to lower frequencies respect to that reported for N-monosubstituted amides, because this group is hydrogen-bonded. However, for nano-fibers spectrum, this band shifts back to 3279 cm^{-1} evidencing a decrease in hydrogen bonding, since this band is attributed to the inter-chain $-C{=}O\cdots H\text{-}N$ hydrogen bonded -NH stretches. Moreover, this shift at 3268-3290 cm^{-1} for α- and β-chitin, respectively, has been reported [34, 120]. Contrasting this band shift, the band near 3100 cm^{-1} remain unchanged in both spectra.

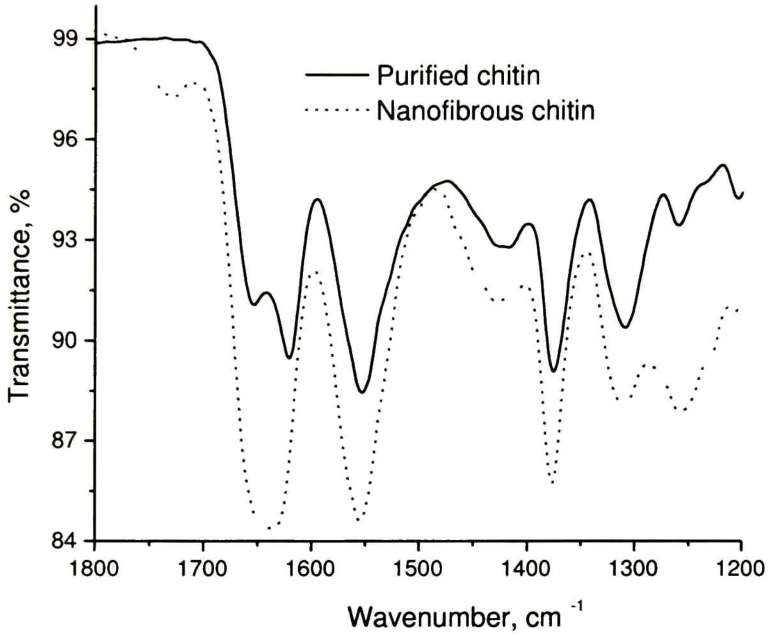

Figure 4.11: Infrared spectra for chitin nano-fibers and purified chitin (raw material) in the 1800 to 1200 cm^{-1} region

The region between 2600-1800 cm^{-1} is not presented since no information is contained in it. In Figure 4.11, the spectra in the region 1800-1200 cm^{-1} is shown. The appearance of a weak band at 1730 cm^{-1} for nano-fibers that can be attributed to carbonyl groups that are hydrogen-bonded to HFIP hydroxyl groups [122]. This explanation can be true since HFIP was the solvent used. The amide I band has a doublet at 1653 and 1621 cm^{-1} for α-chitin . These bands are the result of two types of hydrogen bonds formed by amide groups in the anti-parallel alignment present in α-chitin crystalline regions. The band at 1653 cm^{-1} is related to the ordinary

H-bonded carbonyl group (C=O···H-N) assigned to the stretching of -C=O hydrogen bonded to -NH group. [26] This band is also explained to correspond to the stretching of -C=O groups hydrogen bonded to -NH groups of a neighboring chain, i.e., an inter-chain hydrogen bond [35]. The band at 1625 cm^{-1} is related to -C=O stretching when -C=O is bonded both to an -OH-6 group and to -NH group of the same chain [35]. The existence of one band for nano-fibrous chitin in these region, at 1639 cm^{-1} accounts for the absence of inter-chain H-bonding. For β-chitin is reported a single peak at 1650 cm^{-1} accounting for the existence only of the intra-sheet hydrogen bonding [123]. The amide II band is present at the same wavelength in both spectra at 1553-1555 cm^{-1} and agrees with the fact that the band at 3100 cm^{-1} —also present in both spectra at 3102-3106 cm^{-1}— is an overtone of the amide II band.

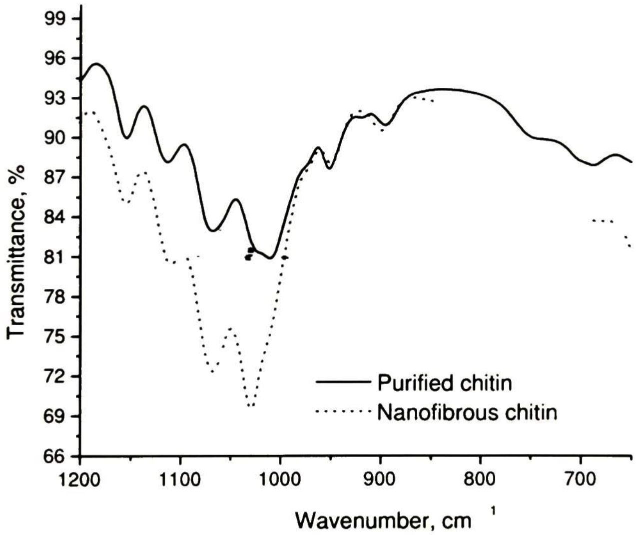

Figure 4.12: Infrared spectra for chitin nano-fibers and purified chitin (raw material) in the 1200 to 650 cm^{-1} region

In Figure 4.12, the spectra in the region 1200-650 cm^{-1} is shown and no evident differences are present. Hence, the chemical structure is preserved after SAS processing, but crystallinity does change. The high stickiness of the nano-fibers can be attributed mainly to the size reduction. Due to the increased surface area, there are more surface molecules with –OH and –NH groups which possibly remain non-H-bonded. The presence of these H-bondable groups may be giving rise to high adhesiveness of the nano-fibers.

4.1.5 X-Ray Analysis

A very important feature of the precipitated nano-fibers by supercritical anti-solvent process is the change in crystallinity, which can be appreciated in the infrared and X-ray diffraction analysis. The infrared spectra of the purified chitin raw material (solid line) and nanofibrous chitin (dashed line) are shown in Figure 4.11. Purified chitin exists as the α-polymorph, since the infrared spectrum shows the two bands in the Amide I region at around 1660 and 1626 cm^{-1} [35, 34, 28]. In contrast, chitin nanofibers do not show these two bands but only one centered at 1639 cm^{-1}; the presence of only one band in the Amide I region is usually related to β-chitin [35], but here is more likely to be related with an amorphous chitin since the X-ray diffraction pattern indicates so.

The most common polymorph of chitin is the α-chitin. In Figure 4.13, the diffraction pattern of purified chitin is shown with well resolved intense peaks at around 9.8 and 19.9 of 2θ degrees, due to the presence of (020) and the mixture of (110) and (040) planes, respectively. Less intense peaks appear at 13.14 and between 20 and 27 of 2θ degrees, owing to the presence of (021), (101), (130), and (013) [124, 125].

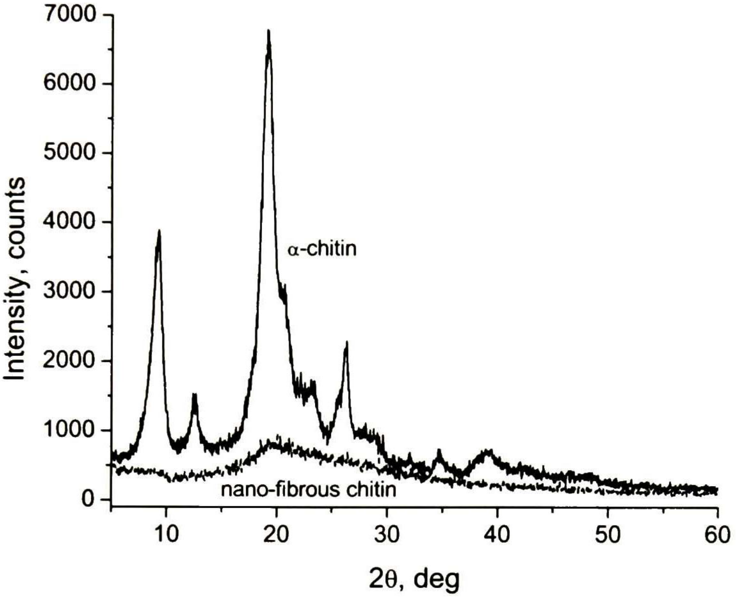

Figure 4.13: Diffraction patterns for α-chitin before processing and SAS-processed chitin nano-fibers

The diffraction pattern of purified chitin was also compared with the diffraction pattern of a commercial purified chitin (not shown) and they are in good agreement. Supercritical anti-solvent process performs a rapid precipitation of chitin yielding an amorphous fibrous material, as indicated by the low intensity very broad diffraction pattern of Figure 4.13.

The infrared spectra and X-ray diffraction pattern suggest that the α-chitin polymorph is physically transformed into an amorphous chitin with a three-dimensional fibrous structure. The resultant nano-fibrous network of this biopolymer is proposed to be used as scaffold for cell culture in tissue engineering. Its high porosity and less crystallinity can be advantageous in this field. Moreover, the proposed SAS technique will provide a sterile, solvent-free biomaterial.

4.2 Chitosan Thermal Relaxations

4.2.1 Thermal Analysis

Thermogravimetric plot for chitosan film is shown in Figure 4.14. The initial weight loss for chitosan film goes from 25 °C to 130 °C, and it is associated with water desorption.

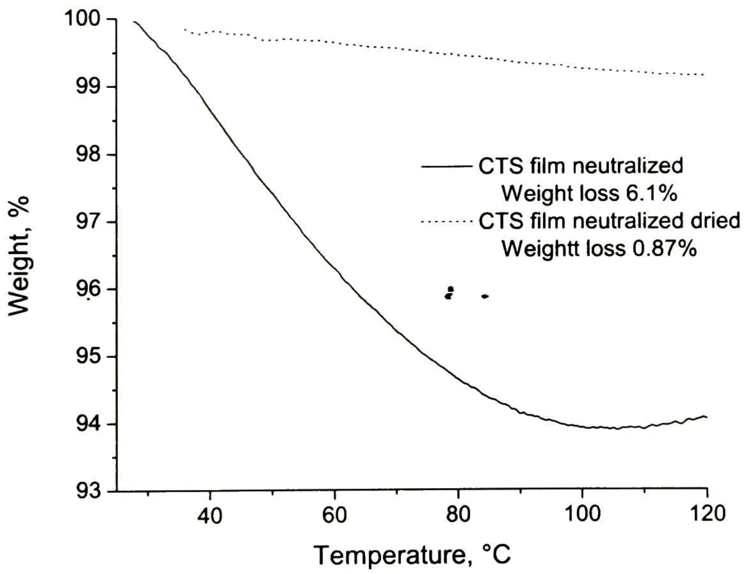

Figure 4.14: Thermogravimetric curve for chitosan film

For samples measured directly from ambient this loss can represent 10-12% of the total sample weight, which are typical values of moisture content for polysaccharides [114]. In this case, the sample had a 6.1% weigth loss due probably to the dryness of the ambient with a very low relative humidity at the moment of the measurement (solid line). Impedance measurements were done over annealed samples which plot is shown with a dotted line. Sample was dried at 110 °C overnight.

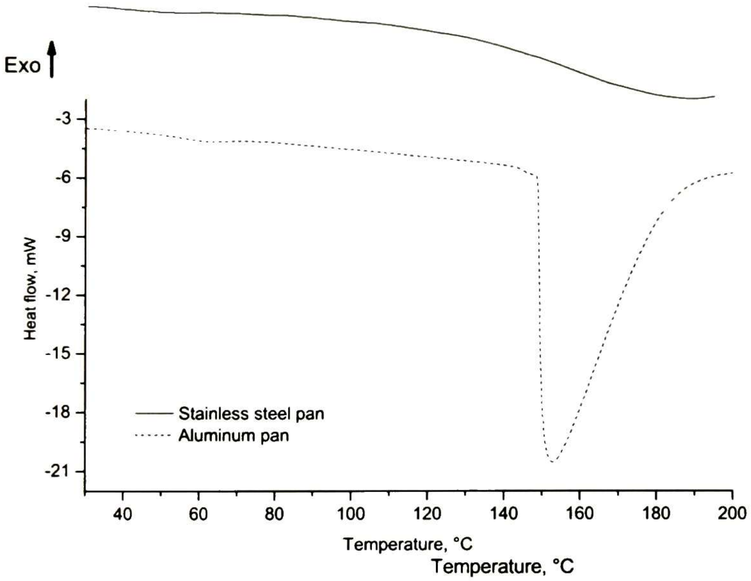

Figure 4.15: Thermogram of chitosan film using stainless steel pan (solid line) and aluminum pan (dotted line) during the first scan.

Thermal Artifact

After several DSC measurements, it was found that the endothermic peak at around 150 °C, is indeed an artifact. If a sealed aluminum pan is used, an endothermic peak at about 130-160 °C appear (Figure 4.15 dotted line), which can be misinterpreted as a melting transition. This cannot be true since these polysaccharides do not melt.

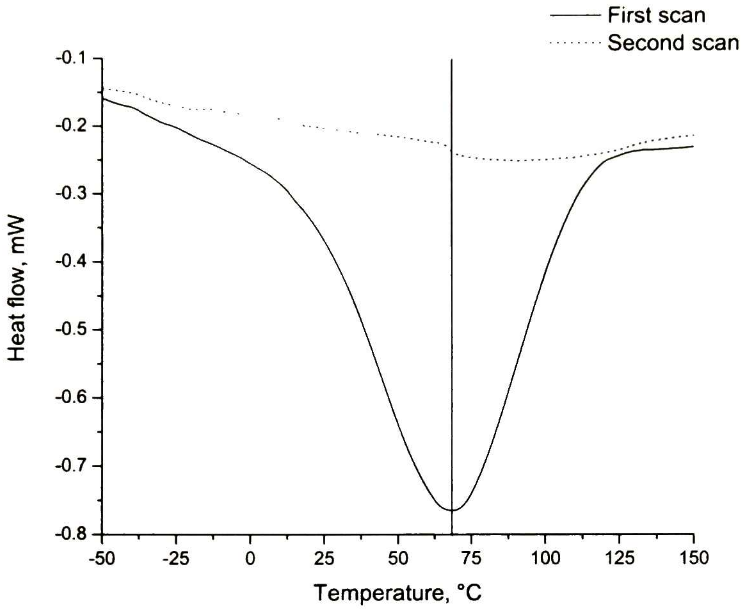

Figure 4.16: Thermogram for chitosan film. First scan from 10 to 130 °C. Heating rate 10 °C/min. The wide endothermic peak is centered at 68.5 °C

On the other hand, if a high-pressure stainless steel pan is used (Figure 4.15 solid line), no event is present until 300 °C (exothermic thermal degradation). As discussed previously, a 10% of moisture is usually present in these polysaccharides, thus an explanation for this artifact is that free water evaporates inside the aluminum pan increasing the pressure as temperature increases until an abrupt lid burst occur (maximum aluminum pan pressure = 0.2 bar) with a change in the temperature of the sample causing the endothermic peak. To avoid this artifact, samples were measured using punctured aluminum pans.

Thermogram for chitosan film is shown in Figure 4.16. First and second scans are shown. The first scan was performed from 10 °C to 150 °C in order to avoid degradation of the films. The wide endothermic peak centered at 68.5 °C is due to water evaporation as previously explained. During the second scan it is possible to observe a small change in the baseline at the same temperature. This change in the baseline has the same shape as a glass transition, and their appearance will be discussed in detail later.

4.2.2 Dielectric Analysis

Figure 4.17 shows a complex impedance plot for chitosan films measured at different temperatures. These Nyquist plots demonstrate two well defined regions: a depressed semicircle at high frequencies, and a linear part in the low frequency range.

This linear part increase and change slope with increasing temperature. Another feature at high temperatures and low frequencies is the appearance of a second semicircle over imposed into the existing one. Such linear part can be associated with contact effects and the second semicircle with interfacial polarization in the bulk of the film also called Maxwell-Wagner-Sillars (M-W-S) relaxation [85, 126].

For analyzing the properties of chitosan films, it is necessary to understand the nature of the low frequency part of the complex impedance plot. Chitosan is a semicrystalline polymer, and charge buildup can occur in the volume or surface of samples due to a change in conductivity and permittivity between phases. This interfacial polarization is known as the Maxwell-Wagner-Sillars polarization and can be modeled with an equivalent circuit composed of two RC elements in series.

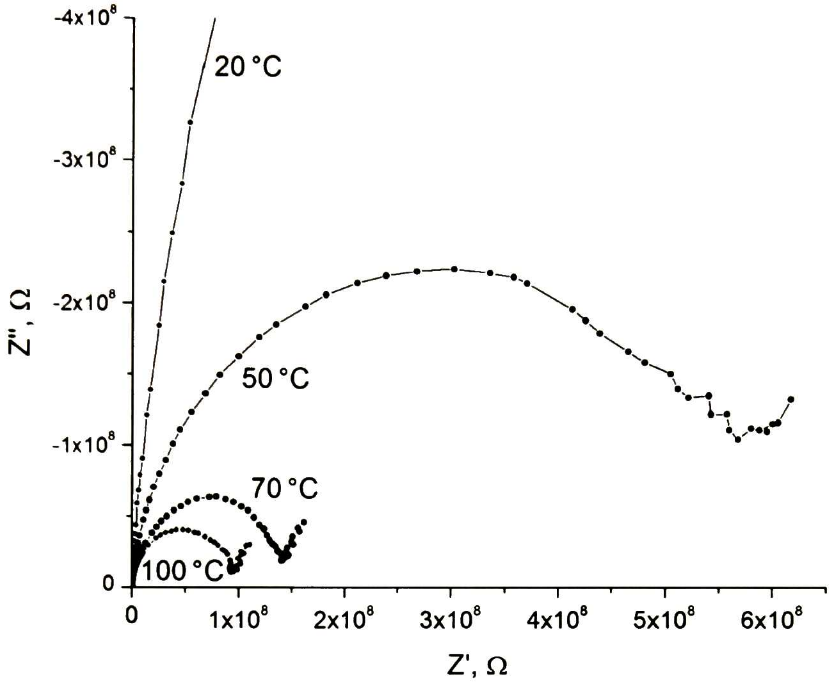

Figure 4.17: Complex impedance spectra at different temperatures. Typical behavior for chitosan films with a depressed semicircle at high frequency

However in this case, the polarization effects (contacts and M-W-S) will not be taken into account for fitting the experimental data; for this, some arguments are given in the following section.

Interfacial Polarization and Contact Effects

The complex impedance spectra is very useful since more information can be deduced from it than from the permittivity bode plot. In Figure 4.18 the complex impedance spectrum of chitosan film at 180 °C is shown.

Features like contact effects and M-W-S polarization are well defined respect to material response. These extra effects appear at low frequencies and high temperatures.

The initial information extracted from this plot is the bulk resistance, R_0, related to dc conductivity with Equation (1.25).

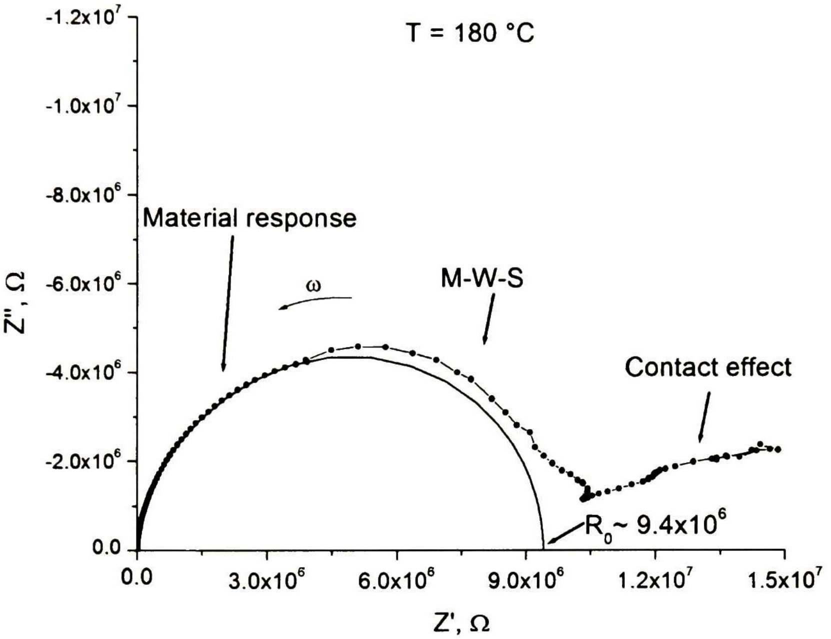

Figure 4.18: Graphical evaluation of material resistance at zero frequency, R_0, fitting the experimental data (dotted line) to a semicircle (solid line), with R_0 taken as the intersection point with the Z' axis. Also shown are the M-W-S polarization and contact effects

The experimental data in the complex impedance plot is fitted to a semicircle using Zview©software. Deviation is taken as low as possible in order to separate the material response from the M-W-S polarization. For that reason a maximum error of 0.2% is set.

The value of the bulk resistance is taken as the intersection point with the Z' axis. This value will be further used for plotting the conductivity behavior versus $1/T$ and for calculate the relaxation time.

Real and imaginary parts of permittivity are plotted against frequency in Figure 4.19. It is possible to compare the behavior of permittivity versus impedance and stand out the advantages of the complex impedance plot.

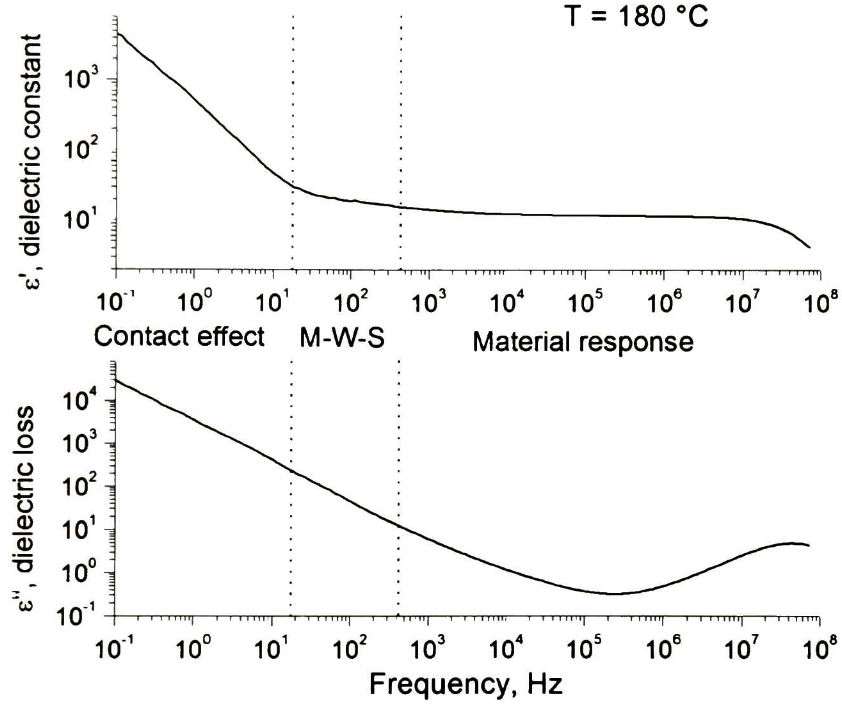

Figure 4.19: Corresponding permittivity bode plot (real and imaginary parts) to the impedance spectra of Figure 4.18. M-W-S polarization and contact effects are shown

The real part of permittivity shows a growth linear part at low frequency which is related to contact effects. These effects increases the value of ε' in two orders of magnitude. The interfacial polarization (M-W-S) is not as evident as in the complex impedance plot, hence being more difficult to observe in the bode plot. On the other hand, in the imaginary part of permittivity, contact effects, M-W-S polarization, dc conductivity, and the low frequency relaxation are all over imposed in the same growth linear part. There is no boundary to identify each one.

It is known that the time constant of the interfacial polarization leads to a single relaxation time [86], which does not depend on the area of sample. Relaxation time dependence on contact area of sample is plotted in Figure 4.20. Since τ depends on area of sample, it can be inferred that interfacial bulk polarization does not play any important role in the mechanism of relaxation.

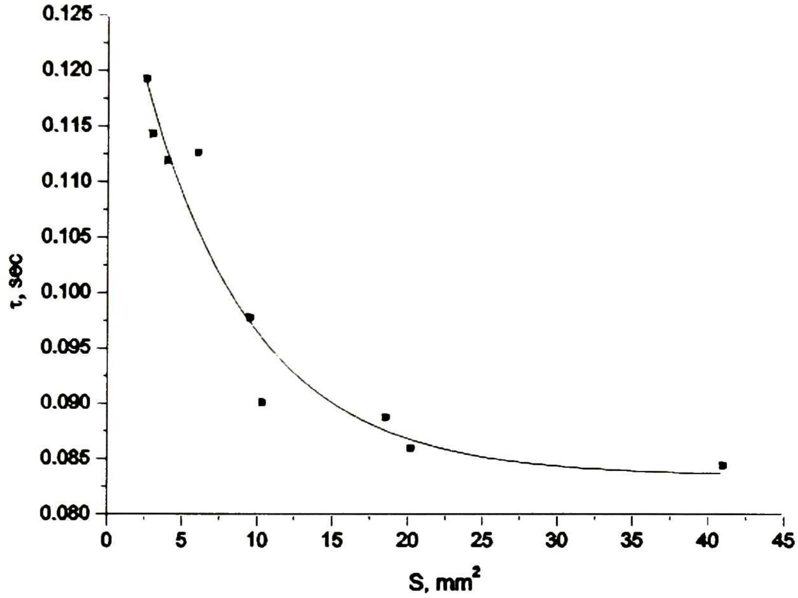

Figure 4.20: Dependence of relaxation time, τ, with contact area, S, of chitosan films ($r = 0.94087$)

In order to verify the influence of metal-polymer contact on the impedance spectra, non-symmetrical structures were prepared. A sample with a large back gold-sputtered electrode with area of 0.75 cm^2 was prepared in order to decrease series resistance of the bottom face electrode. Also a counter gold electrode was formed on the top face with an area of 0.008 cm^2

Due to difference in area of contacts, the current thorough the structure will depend, basically, on the properties of the top face electrode.

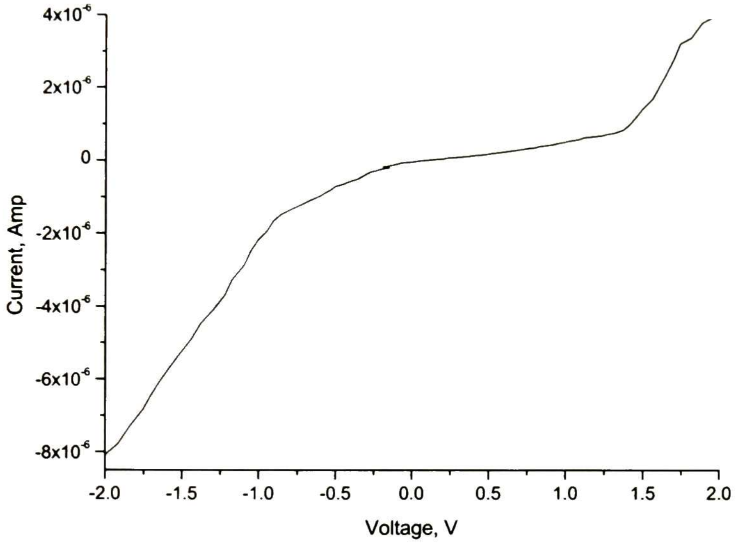

Figure 4.21: Current-Voltage response for chitosan films

A typical I-V curve is shown in Figure 4.21, where negative voltages correspond to the forward direction. The current-voltage characteristic of such asymmetrical structure is qualitatively similar to the dependence obtained in other metal-organic-metal structures [127, 128]. To get more insight into the characteristics of Au-chitosan-Au samples, impedance measurements were carried out with different applied forward bias voltage as shown in Figure 4.22. In this plot, only the low frequency part of impedance spectra change with increasing of bias voltage, while the depressed semi-circles at the high frequency region remain unchanged. The increasing of forward bias lead to: a change in barrier's parameters, a reduction of barrier resistance, and a change in the low frequency part of impedance spectrum.

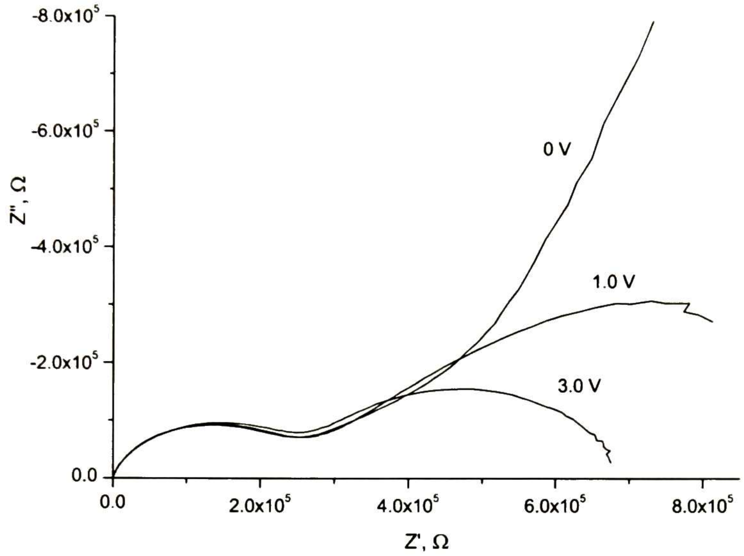

Figure 4.22: Impedance spectra at different bias applied voltage

From the results obtained, we can infer that the growth part of impedance spectra in the low frequency range, is related to the barrier behavior of the contact Au-chitosan-Au. As a consequence, for the analysis of the bulk properties of chitosan films, it is necessary to use only the depressed semicircle at the high frequency region.

4.2.3 Equivalent Circuit Fitting

If the dc conductivity is subtracted from the imaginary part of permittivity, using Equation (1.26), two well defined relaxations are observed. These relaxations are shown in bode plots (Figure 4.23) as well as in the Argand diagram of Figure 4.24.

The information of a relaxation due to a glass transition, if such transition exists, must be contained into the low frequency relaxation. Thus, only the low frequency part of the experimental data will be fitted using an equivalent circuit. In principle the relaxation at lower frequency is label as α, while the following relaxation is the β-relaxation.

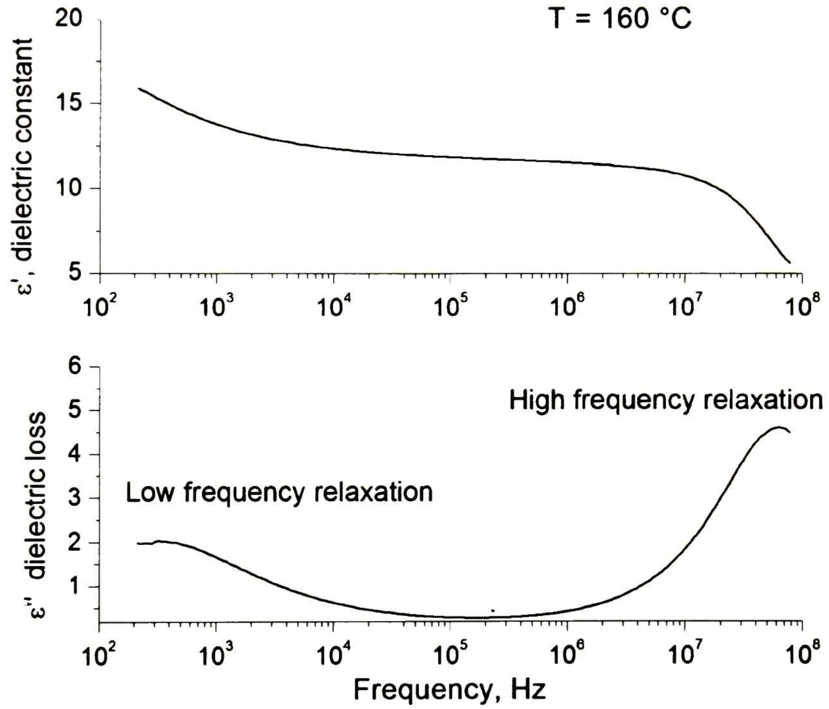

Figure 4.23: Bode plots for permittivity with dc correction at 160 °C

Moreover, experimental data of chitosan films for the fitting is restricted to the region where no contact effects and M-W-S polarization appear. Since the relaxation moves to higher frequencies as temperature is increased. This frequency region must be adjusted for each temperature.

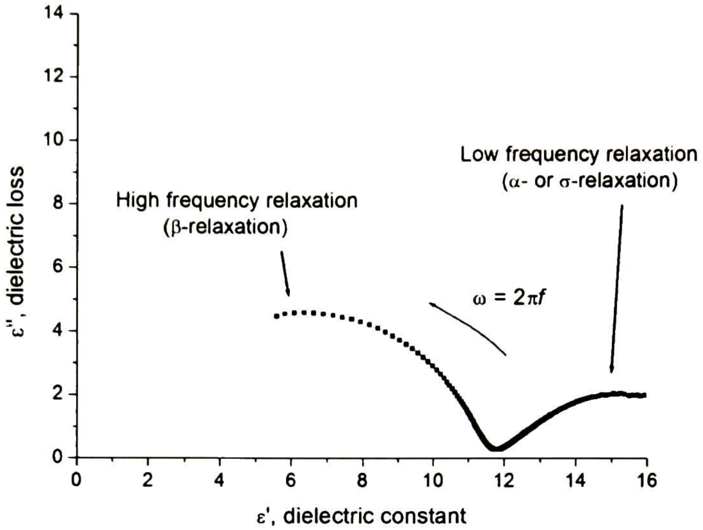

Figure 4.24: Argand plot for chitosan film with dc correction at 160 °C

Furthermore, since the dc conductivity subtraction might introduce more error into the experimental data (see section 1.4.9), the fitting is done using an equivalent circuit which is a combination of a distributed element in parallel with a resistance and with a capacitance. So, no dc correction is done in this work, since bulk resistance is taken into account into the equivalent circuit. This is the same approach of Furukawa *et al.* [85] and Viciosa *et al.* [126]; although it differs from that of Einfeldt *el al.* [91] where they made the dc correction to the experimental data and fit the resultant permittivity.

The equivalent circuit used in this work is shown in Figure 4.25, where the distributed element is given in the Zview©software for Havriliak-Negami; the capacitance C_{infty} must be introduced for the ε_∞; and the resistance, R_0 describes the dc conductivity.

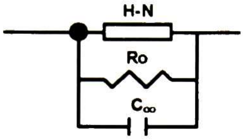

Figure 4.25: Equivalent circuit using a distributed element (H-N), a resistance and a capacitor for describing the low frequency relaxation

The complex admittance Y^* of such circuit may be expressed as following:

$$Y^* = j\omega C_\infty + \frac{j\omega(C_0 - C_\infty)}{[1 + (j\tau\omega)^\alpha]^\beta} - \frac{1}{R_0} \tag{4.1}$$

thus, dividing for $j\omega\varepsilon_0$ it is possible to obtain the complex permittivity [86] defined by:

$$\varepsilon^* = \varepsilon_\infty + \frac{\varepsilon_s - \varepsilon_\infty}{[1 + (j\omega\tau)^\alpha]^\beta} + \frac{\sigma_{dc}}{j\omega\varepsilon_0} \tag{4.2}$$

where ε_s and ε_∞ are the low and high frequency limit values of the real part of complex permittivity, respectively; τ is the relaxation time; and α and β are fitting parameters. Which is the same equation proposed by Furukawa *et al.* [85], and explained previously in section 1.4.5 as Equation (1.13).

The temperature dependence of the fitting parameters is depicted in Figure 4.26, where $\alpha, \beta, \varepsilon_\infty$, and $\Delta\varepsilon$ are plotted. The α parameter remain almost constant at a value of 1.0, suggesting a Davidson-Cole type relaxation. Remember that the empirical correlation of Havriliak-Negami includes the special cases of the relaxation expressions of Debye (if $\alpha = \beta = 1.0$), Cole-Cole (if $\beta = 1.0$), and Davidson-Cole

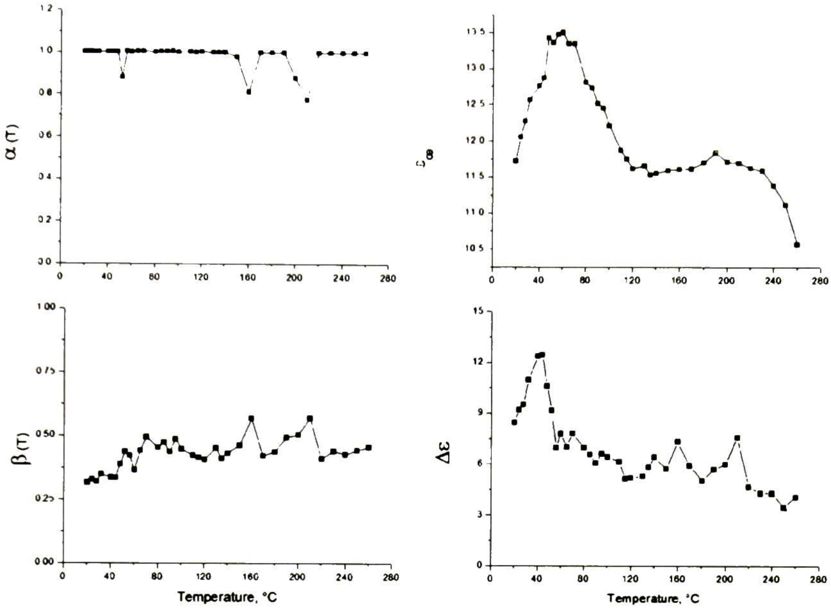

Figure 4.26: Temperature dependence of fitting parameters

(if α = 1.0). This behavior of α also indicates a narrow distribution of relaxation times. While low values for β represent an asymmetrical distribution in the time and frequency scales. The β shows a slight increment with temperature, with values between $0.25 < \beta < 0.50$.

The dielectric strength shows a peak at 45 °C and, even the points are disperse, a decreasing behavior with temperature. An interesting feature is the behavior of ε_∞ vs temperature. It has a maximum value of 13.5 at 60 °C, and then it shows a constant value of about 11.5 from 120 to 230 °C. After this temperature it further decreases. The behavior of this parameter will be discussed later.

Using the equivalent circuit approach it is possible to separate the dc conductivity of sample just eliminating the resistance R_0 from the circuit depicted in Figure 4.25, and thus simulate the low frequency relaxation using the equivalent circuit from Figure 4.27.

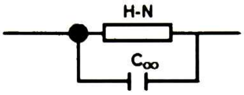

Figure 4.27: Equivalent circuit for separate dc conductivity of sample and simulate the low frequency relaxation

For further illustrate the agreement between experimental data and fitting, a comparison among experimental values, dc corrected experimental values and simulated data from fitting are presented in Figure 4.28. Simulated data is plotted as a solid line in Figure 4.28 and is in good agreement with dc corrected data (open circles).

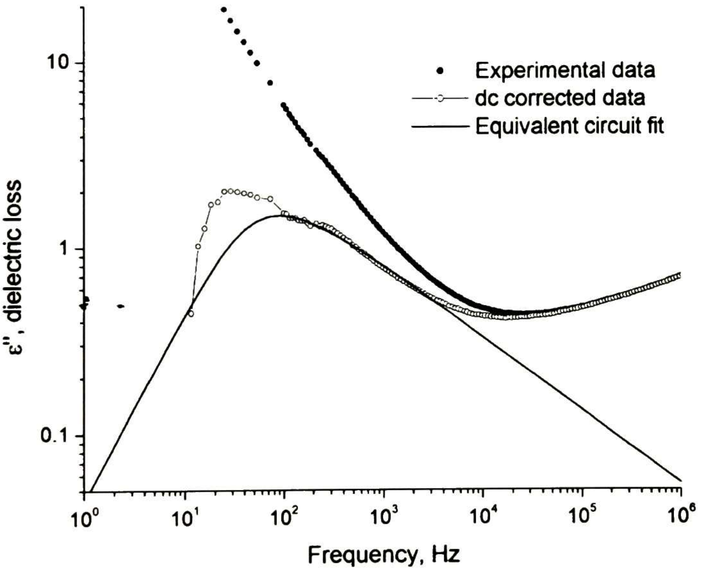

Figure 4.28: Comparison among experimental data (filled circles), dc corrected data (open circles), and equivalent circuit fitted curve (solid line) for the sample measured at 90 °C

The corrected dielectric loss was done using Equation (1.26). As can be seen, the

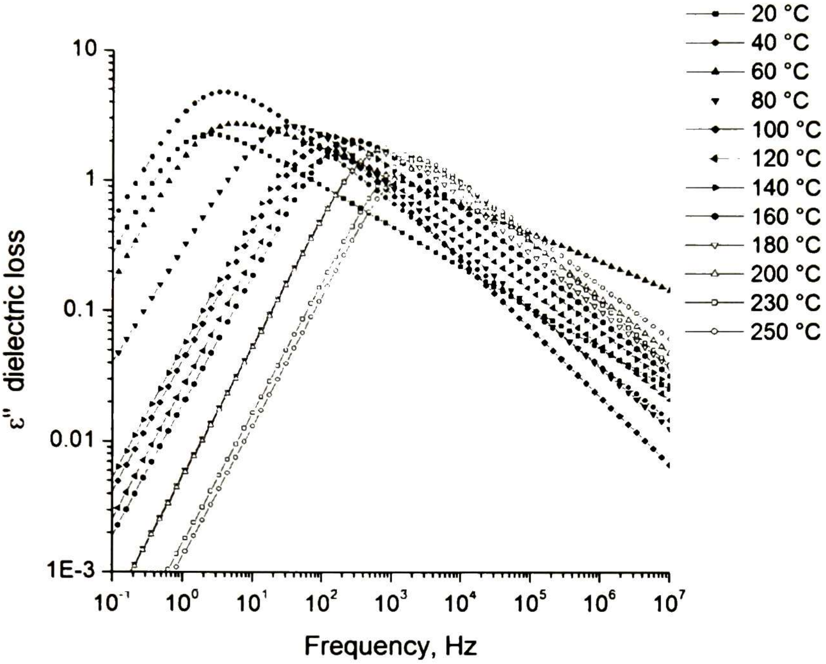

Figure 4.29: Dielectric loss spectra from simulated data at different temperatures

dielectric loss corrected data show a second feature in the low frequency end, which is not part of the relaxation. If experimental data had been corrected and the fitting done over dc corrected data, the results would had contained more error. The fitted data values for imaginary part of permittivity can be plotted against frequency at different temperatures (Figure 4.29) in order to visualize the behavior of the relaxation. It is possible to see that relaxation moves to higher frequencies as temperature increase. Of course, the shape of the relaxation corresponds to a Davidson-Cole relaxation.

Furthermore, dielectric loss is plotted as a function of temperature at two different fixed frequencies in Figure 4.30. It is interesting to note the effect of dc conductivity over dielectric loss at high temperature and low frequencies. The solid symbols represent the dielectric loss taken from simulated data at 10 Hz (filled circles), and 1.0 kHz (filled triangles). At 10 Hz it is possible to observe a relaxation with a maximum value of 4.2 centered around 40 °C, while at 1.0 kHz the relaxation at about 210 °C is more pronounced. The open symbols represent the dielectric loss taken from experimental data without subtracting dc conductivity.

This conductivity obscure the material response. For 1.0 kHz, experimental (open triangles) and simulated are very close at low temperatures, but after 80 °C, experimental data increases exponentially. The same effect occurs at lower frequencies (open circles) tough it appears at lower temperatures.

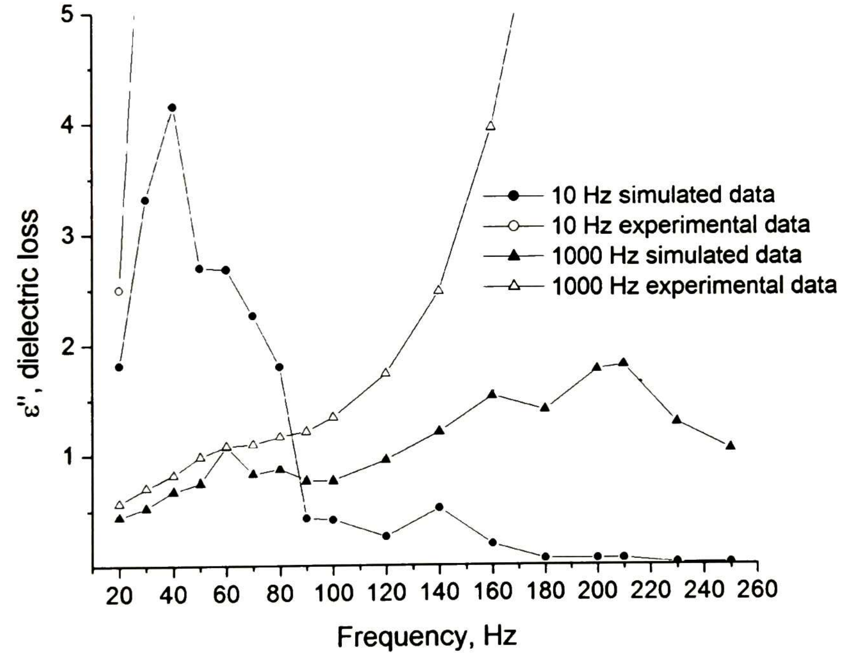

Figure 4.30: Dielectric loss as a function of temperature at 10 Hz and 1000 Hz. Comparative of experimental data (open symbols) and simulated data (filled symbols)

4.2.4 Temperature Dependence of Relaxation Time

Relaxation time for each temperature is obtained form fitting the experimental data (with no dc correction) to the equivalent circuit of Figure 4.25. The logarithm of relaxation time is plotted against reciprocal temperature in Figure 4.31. Two well differentiated regions are observed: an Arrhenius type at high temperature (solid line), and a Vogel type in the low temperature region (dotted line). The low temperature region is well described with the Vogel-Fulcher-Tamman-Hesse Equation (1.21), while for the high temperature region the Arrhenius Equation (1.20) for relaxation time

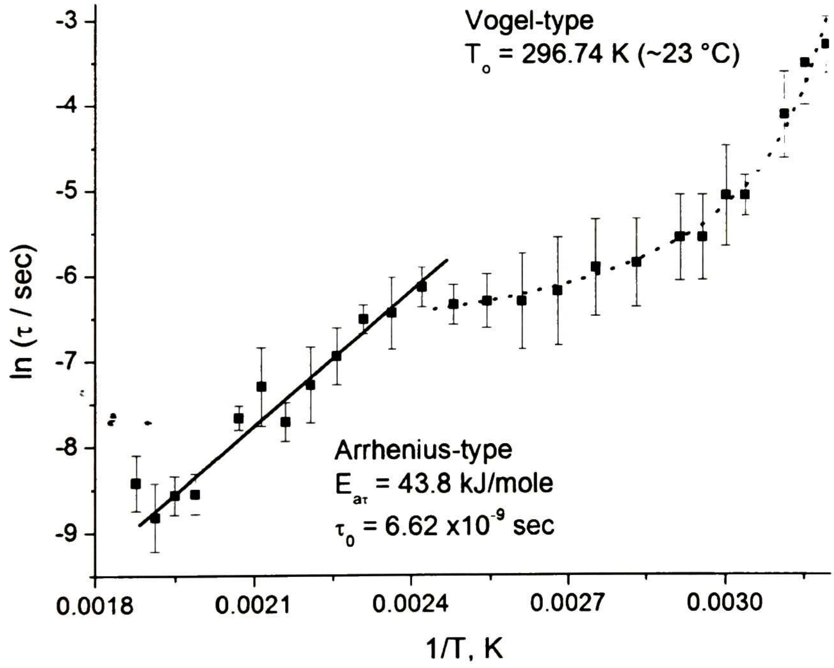

Figure 4.31: Relaxation time dependence on reciprocal temperature. Values obtained from fitting the low frequency relaxation with the equivalent circuit of Figure 4.25. Two regions are observed: an Arrhenius-type at high temperature (solid line), and a Vogel-type in the low temperature region (dotted line)

For the Arrhenius type at high temperature region (313-373 K), it was found an energy of activation of 43.8 kJ/mole, and a pre-exponential factor of 6.62×10^{-9} The activation energy does not corresponds to a typical value for the σ relaxation of chitosan as reported by Viciosa et al. [126], with values between 95-110 kJ/mole. Our measured value is half of those reported. Probably due to the presence of residual moisture in the sample. All samples were annealed at 110 °C prior to measurement, however the atmosphere inside the furnace cannot be controlled. Thus it is highly possible that chitosan film adsorbed some water from ambient even during the measurement. These water contained in the bulk material exert some influence to the polymer relaxation which can be detected using dielectric analysis. Moreover, Einfeldt *et al.* [91] found difficult to detect this σ relaxation in chitosan as well as in some strongly or per-substituted polysaccharides.

Another feature is that typical values for relaxation strength for σ relaxation of polysaccharides are nearly independent of temperature and lay between 1 and 10 [91]. The relaxation strength measured in this work is somewhat independent of temperature (above 100 °C) with values between 4-8, as can be seen in Figure 4.26.

The water contained in the sample modifies the response its response. Water can act as a plasticizer for chitosan. For that reason, it is possible to fit the low temperature region using the VFTH Equation (1.21). The VFTH equation describes the behavior of polymer near glass transition temperature, Tg, and in many polymers T_0 is usually 50 K lower than Tg [93, 94, 95]. The Vogel-temperature obtained is 296.74 K, and thus, the Tg value must be 73 °C.

4.2.5 Conductivity Dependence on Temperature

The behavior of conductivity can also be analyzed as a function of temperature. Interestingly, it shows nearly the same behavior as relaxation time. It makes sense since both quantities correspond to the low frequency region. Although a striking difference is that dc conductivity is evaluated from experimental data while relaxation time is calculated from fitted data to the equivalent circuit. As previously explained (sections 1.4.9 and 4.2.2), dc conductivity, σ_{dc}, is calculated using equation (1.25), where the bulk resistance, R_0, is graphically evaluated [92] as depicted in Figure 4.18. Dependence of $\ln\sigma$ versus reciprocal temperature is plotted in Figure 4.32.

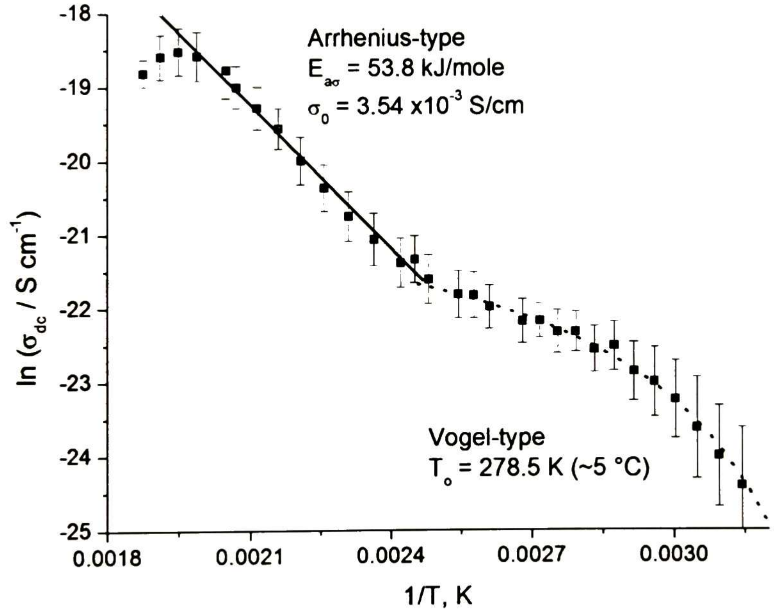

Figure 4.32: Conductivity dependence with temperature. Experimental results (circles) adjusted to a Vogel-type relaxation (dotted line) at low temperature. Arrhenius-type relaxation at high temperature (solid line)

For the low temperature region, the VFTH relation can be written in terms of conductivity [88] which is Equation (1.28). The Vogel-temperature obtained with this relation is 278.52 K, thus a predicted glass transition temperature of 55 °C is given. For the Arrhenius-type process in the temperature range from 110-240 °C, an apparent activation energy of 53.8 kJ/mole was found. This value is very close to that obtained in the relaxation time plot of 43.8 kJ/mole indicating a good correlation in the measurement. Above 240 °C a negative energy of activation is found. This is normally known as "metallic behavior" and can be attributed to the beginning of degradation of chitosan. A negative activation energy of conduction had been reported in polymeric blends [129, 130] which corresponds to a non reversible degradation of the polymer films.

In Table 4.2 the values for fitting parameters of the Vogel-type relaxation are listed. It is noteworthy that Vogel-temperature, T_0, and the activation parameter, B, have very close values. The correlation factor for relaxation time is lower since this parameter is provided from a previous fitting where systematical error was introduced.

Table 4.2: Parameters from fitting Relaxation Time and Conductivity for the Vogel-type relaxation

Parameter	**Conductivity**	**Relaxation Time**
T_0, K	278.52	296.74
σ_0, $S\,cm^{-1}$ or τ_0, sec	1.27×10^{-9}	9.46×10^{-4}
B	151.18	64.78
R^2	0.99238	0.980381
χ^2	0.00565	0.02658

In Table 4.3 the values for fitting parameters of the Arrhenius-type relaxation are listed. It is noteworthy that the activation energy, have very close values.

Table 4.3: Parameters from fitting Relaxation Time and Conductivity for the Arrhenius-type relaxation

Parameter	**Conductivity**	**Relaxation Time**
$E_{a\sigma}$ or $E_{a\tau}$, kJ/mole	-53.8	43.8
σ_0, $S\,cm^{-1}$ or τ_0, sec	3.54×10^{-3}	6.62×10^{-9}
R	-0.99512	0.9778
Std. Dev.	0.11257	0.20273

If the logarithm of relaxation time is plotted against the logarithm of dc conductivity, the points can be fitted to a line with slope -1.0685. Einfeldt *et al.* [91] proposed this correlation because the dc conductivity represents a migration property of movable ions and the relaxation time corresponds with the formation of dipolar structures in the material. For the σ-relaxation, they found a good correlation described with the following equation:

$$\ln \tau = A + B \ln \sigma_{dc} \tag{4.3}$$

where B is the fraction of both activation energies, $B = E_{a\tau}/E_a\sigma_{dc}$, with typical values between 0.89 and 1.15 for polysaccharides. In Figure 4.33 the double logarithmic plot is shown. The slope of the line is -1.0685 while the calculated B is equal to -0.901.

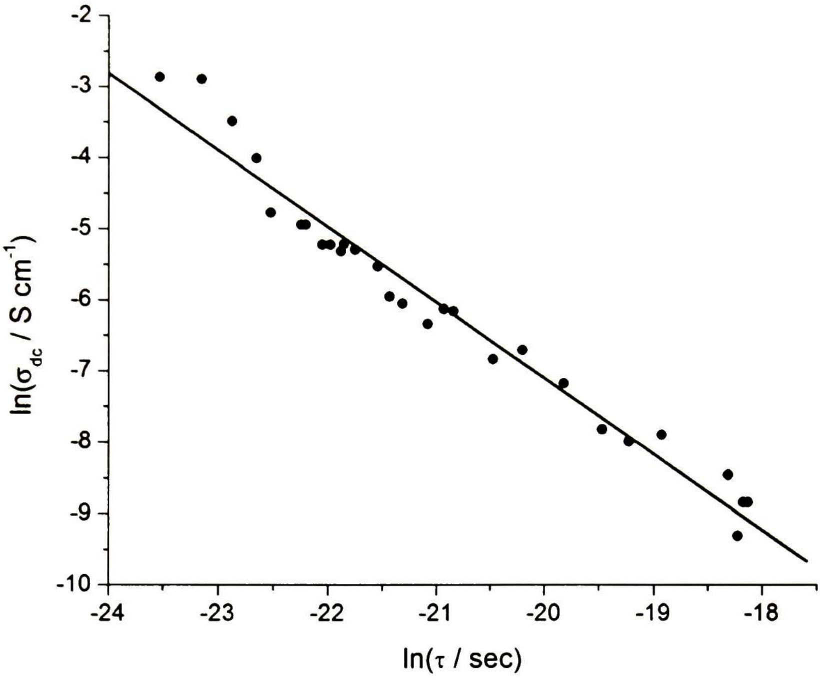

Figure 4.33: Correlation between dc conductivity and relaxation time for the σ-relaxation in the temperature range from 110 to 240 °C

4.2.6 Proposed Relaxation Mechanisms

It was found that two different processes occur in the low frequency relaxation of chitosan; both, in the relaxation time and conductivity plots. The low temperature process with the features of an α-relaxation which is well described by the VFTH relation. The high temperature process is Arrhenius-type and present some features that might associate it with the σ-relaxation found in a series of polysaccharides. Finally, above 240 °C, degradation of the biopolymer begins.

Low temperature relaxation: 40-100 °C

The VFTH relation yields a glass transition temperature of about 73 °C and 65 °C in the relaxation time (Figure 4.31) and conductivity (Figure 4.32) plots, respectively. A peak centered around 40 °C is obtained when dielectric loss is plotted against temperature at 10 Hz (Figure 4.30), indicating a relaxation. Evaporation of water is observed in the thermogram of Figure 4.16 at 68.5 °C during first scan. However, a change in baseline is seen at the same temperature during the second scan, indicating a Tg. As explained previously, it is possible that some small quantity of water remains inside the bulk material acting as a plasticizer and giving rise to this relaxation in the temperature range 60-80 °C. This has to be proved yet, however, experimental evidence has been obtained in our research center using ellipsometry spectroscopy, that even with a very low water content (<1.0%) this effect at around 60-70 °C can be detected, but in well dried samples it is not detected [131]. To further support this proposed relaxation, it has been reported as a glass transition [107, 108].

High temperature relaxation: 110-240 °C

Even this process is Arrhenius-type it cannot be related to a β-relaxation since it occurs in the high frequency range and was not studied here. The only reference to this process is the σ-relaxation found in some polysaccharides by Einfeldt *et al.*[91], but they are not able to detect this σ-relaxation for chitosan. Viciosa et al.[126] reported a well correlated σ-relaxation for chitosan neutralized and non-neutralized, with the difference that they used a less deacetylated chitosan with a higher molecular weight (DD=68-70%; Mv=594kDa) than the sample studied here. Differences that can modify the response in parameters such as energy of activation and preexponential factor. In this work it was found, for a σ-relaxation, a dielectric strength values between 4-8, and the good correlation between dc conductivity and relaxation time with a slope equal to -1.0685 [91]. The energy of activation value (41-46 kJ/mole) does not lie into the typical values for these relaxation (95-110 kJ/mole); and the preexponential factor for the relaxation time is several orders of magnitude less: 7.7×10^{-9} compared to 2×10^{-17} for neutralized chitosan reported by Viciosa *et al.*[126].

Above 240 °C

In the conductivity plot, a negative slope has been associated to polymer degradation [129, 130]. This transition can be attributed to the movement of end groups of the backbone as it could be the onset of depolymerization, due to breaking of glycosidic bonds [112].

Chapter 5

Conclusions and Recommendations

5.1 Chitin Nano-fibers by SAS

Nano-fibrous chitin can be successfully produced using supercritical antisolvent process. The obtained nano-fibrous chitin is very porous and sticky, and has very low bulk density. The average diameter of the nano-fibers is 84 nm. Infra-red analysis show that the molecular structure is not altered during the supercritical antisolvent processing.

An important feature of the precipitated nanofibers by supercritical antisolvent process is the change in crystallinity. The infrared spectra and X-ray diffraction pattern suggest that the α-chitin polymorph is physically transformed into an amorphous chitin with a three-dimensional fibrous structure.

It is proposed that, by combining the bioactive properties of chitin with the SAS ability for obtaining porous structures, a novel biomaterial can be successful used as scaffold in tissue engineering. An important feature of this work is the reproducibility of results, being capable of produce the nanofibrous chitin material in

Auburn University laboratories as well as in Cinvestav-Querétaro. Using a similar setup but with different vessels (100 mL and 40 mL) the process was reproduced with satisfactory results.

5.2 Chitosan Thermal Relaxations

It is possible to observe three different processes in the conductivity plot of solvent-casted chitosan films. In the low temperature region (40-100 °C), the VFTH relation yields a glass transition temperature of about 73 °C and 55 °C in the relaxation time and conductivity plots, respectively. A change in the baseline of the thermogram during the second scan indicates a Tg at 68.5 °C. It is possible that some small quantity of water remains inside the bulk material acting as a plasticizer and giving rise to this relaxation in the temperature range 60-80 °C.

The high temperature Arrhenius-type process (110-240 °C)might be related to the σ-relaxation found in some polysaccharides. In this work it was found that, for a σ-relaxation, dielectric strength values are between 4-8, and there is a good correlation between dc conductivity and relaxation time with a slope equal to -1.0685 [91]. Differences in parameters such as energy of activation and preexponential factor can be due to different properties of the material such as degree of deacetylation and molecular weight.

The process above 240 °C is associated to the beginning of degradation of chitosan, due to chain scission giving rise to depolymerization. Impedance Spectroscopy is a very sensitive tool for analyzing thermal relaxations on biopolymers. Dielectric analysis is already used as a characterization technique, although, including the conductivity plot and the complex impedance spectrum will result in a more complete understanding of the phenomenological behavior of these biopolymers.

5.3 Perspectives for future work

5.3.1 Chitin and SAS for Biomaterials Processing

Even though the produced nanofibrous biomaterial can be commercialized in the medical specialty field, it would be necessary to evaluate a different solvent, not as expensive as HFIP. An interesting opportunity is to evaluate a mixture of HFIP with some other solvents such as dichloromethane (DCM) or dimethylacetamide (DMA).

The evaluation of this biomaterial as a scaffold for cell culture in Tissue Engineering may be straightforward, once the application is decided. Either for cartilage or nerve repair, or even as a scaffold for bone tissue. A study on its biocompatibility with different cells might be done.

Also different composites can be produced using this SAS technique. A mixture of chitin with polymethylmethacrylate (CTN/PMMA) may be dissolved in HFIP and precipitated in the same fashion, yielding a composite biomaterial for different applications.

5.3.2 Impedance Spectroscopy for Biopolymer Analysis

Polysaccharides are a very interesting area of study due to its commercial importance. Measurements with Impedance Spectroscopy can be done in different polysaccharides such as chitin, cellulose, amylose, amylopectin, dextran, pullulan, heparin, or hyaluronic acid, in order to assess the capability of this powerful tool. Conductivity plot may be compared and a description of the thermal behavior of these polysaccharides can be done. Impedance measurements can be extended even to different gums as xanthan, guar, tragacant, etc.

In order to evaluate the glass transition temperature of chitosan films, it is important to take care in the preparation of the sample. Also the measurement cell must be modified to get control over the atmosphere, *i.e.* to use a hermetically closed cell with a purge gas or in vacuum during the measurement. This measurement can also can be done over chitosan films with different moisture contents. Water acts as a plasticizer decreasing the value of glass transition temperature.

It is possible to investigate different fitting procedures to obtain a complete separation of the low frequency relaxation. This can be done either using the equivalent circuit approach or using the Havriliak-Negami relation in series with other terms accounting for interfacial polarization and electrode polarization effects.

Bibliography

[1] M. A. McHugh and V. J. Krukonis. *Supercritical Fluid Extraction: Principles and Practice.* Butterworth, Stoneham, MA, 2nd edition, 1994.

[2] R. H. Perry and D. W. Green. *Perry's Chemical Engineers' Handbook.* McGraw-Hill, 1990.

[3] Wikipedia [Web Site]. Dielectric Responses. Retrived December 19, 2005. Available at: http://en.wikipedia.org/wiki/Image:Dielectric_responses.jpg, December 18, 2005.

[4] M. N. V. Ravi Kumar, R. A. A. Muzzarelli, C. Muzzarelli, H. Sashiwa, and A. J. Domb. Chitosan Chemistry and Pharmaceutical Perspectives. *Chem. Rev.*, 104(12):6017–6084, 2004.

[5] T. H. Fischer, R. Connolly, H. S. Thatte, and S. S. Schwaitzberg. Comparison of Structural and Hemostatic Properties of the Poly-N-Acetyl Glucosamine Syvek Patch with Products Containing Chitosan. *Microsc. Res. Tech.*, 63:168–174, 2004.

[6] M. W. Chan, S. D. Schwaitzberg, M. Demcheva, J. Vournakis, S. Finkielsztein, and R. J. Conolly. Comparison of Poly-N-Acetyl Glucosamine with Absorbable Collagen (Actifoam), and Fibrin Sealant (Bolheal) for Achieving Hemostasis in a Swine Model of Splenic Hemorrhage. *J. Trauma*, 48:454–458, 2000.

[7] J. Vournakis, M. Demcheva, A. Whitson, R. Guirca, and E. R. Pariser. Isolation, Purification, and Characterization of Poly-N-Acetyl Glucosamine Use as a Hemostatic Agent. *J. Trauma*, 57:S2–S6, 2004.

[8] L. Li, J.H.P. Hui, J. C. H. Goh, F. Chen, and E. H. Lee. Chitin as a Scaffold for Mesenchymal Stem Cells Transfers in the Treatment of Partial Growth Arrest. *J. Pediatr. Orthop.*, 24:205–210, 2004.

[9] S. Yamane, N. Iwasaki, T. Majima, T. Funakoshi, T. Masuko, K. Harada, A. Minami, K. Monde, and S. Nishimura. Feasibility of Chitosan-based Hyaluronic Acid Hybrid Biomaterial for a Novel Scaffold in Cartilage Tissue Engineering. *Biomaterials*, 26:611–619, 2005.

[10] T. Funakoshi, T. Majima, N. Iwasaki, S. Yamane, T. Masuko, A. Minami, K. Harada, H. Tamura, S. Tokura, and S. Nishimura. Novel Chitosan-based Hyaluronan Hybrid Polymer Fibers as a Scaffold in Ligament Tissue Engineering. *J. Biomed. Mater. Res. A.*, 74:338–346, 2005.

[11] T. Majima, T. Funakosi, N. Iwasaki, S. T. Yamane, K. Harada, S. Nonaka, A. Minami, and S. Nishimura. Alginate and Chitosan Polyion Complex Hybrid Fibers for Scaffolds in Ligament and Tendon Tissue Engineering. *J. Orthop. Sci.*, 10:302–307, 2005.

[12] T. Masuko, N. Iwasaki, S. Yamane, T. Funakoshi, T. Majima, A. Minami, N. Ohsuga, T. Ohta, and S. Nishimura. Chitosan-RGDSGGC Conjugate as a Scaffold Material for Musculoskeletal Tissue Engineering. *Biomaterials*, 26:5339–5347, 2005.

[13] P. York. Strategies for particle design using supercritical fluid technologies. *PSTT*, 2:430–440, 1999.

[14] J. Jung and M. Perrut. Particle design using supercritical fluids: Literature and patent survey. *J. Supercrit. Fluids*, 20(3):179–219, 2001.

[15] C.A. Eckert, B.L. Knutson, and P.G. Debenedetti. Supercritical Fluids as Solvents for Chemical and Materials Processing. *Nature*, 383(26):313–318. 1996.

[16] B. D. Ratner, A. S. Hoffman, F. J. Schoen, and J. E. Lemons. Biomaterials science: A multidisciplinary endeavor. In B.D. Ratner, A.S. Hoffman, F.J. Schoen, and J.E. Lemons, editors, *Biomaterials Science: An Introduction to Materials in Medicine*, pages 1–9. Elsevier, Amsterdam, 2nd edition, 2004.

[17] J. F. Louvier-Hernández, G. Luna-Bárcenas, R. Thakur, and R. B. Gupta. Formation of Chitin Nanofibers by Supercritical Antisolvent. *J. Biomed. Nanotech.*, 1:109–114. 2005.

[18] Merriam-Webster Online Dictionary [Web site]. Chitin Definition. Retrived October 17, 2005. Available at: http://www.m-w.com/dictionary chitin, October 17, 2005.

[19] H-M. Cauchie. Chitin Production by Arthropods in the Hydrosphere. *Hydrobiology*, 470:63–96, 2002.

[20] E. Khor. *Chitin: Fulfilling a Biomaterials Promise.* Elsevier, Oxford, UK, 2001.

[21] C. Lárez-Velásquez [Serial Online]. Algunos usos del quitosano en sistemas acuosos. *Revista Iberoamericana de polímeros*, 4(2):91–109, Retrived October 17, 2005. Available at: http://www.ehu.es/reviberpol/pdf/ABR03/Cristobal2003.pdf April, 2003.

[22] A. Pastor de Abram, editor. *Quitina y Quitosano: Obtención, Caracterización y Aplicaciones.* Pontificia Universidad Católica del Perú/Fondo Editorial, 2004.

[23] Merriam-Webster Online Dictionary [Web Site]. Coat of Mail Definition. Retrived October 25, 2005. Available at: http://www.m-w.com dictionary/coat

[24] K. H. Meyer and G. W. Pankow. Sur la Constitution et la Structure de la Chitine. *Helv. Chim. Acta*, 18:589–598, 1935.

[25] G. L. Clark and A. F. Smith. X-Ray Diffraction Studies of Chitin, Chitosan, and Derivatives. *J. Phys. Chem.*, 40:863–879, 1936.

[26] S. E. Darmond and K. M. Rudall. Infra-red and X-Ray Studies of Chitin. *Discus. Faraday Soc.*, 9:251–260, 1950.

[27] D. Carlström. The Crystal Structure of α-chitin. *J. Biophysic. Biochem. Cytol.*, 3:669–683, 1957.

[28] F. G. Pearson, R. H. Marchessault, and C. Y. Liang. Infrared Spectra of Crystalline Polysaccharides. V. Chitin. *J. Polym. Sci.*, 43:101–116, 1960.

[29] N. E. Dweltz. The Structure of Chitin. *Biochim. Biophys. Acta*, 44:416–435, 1960.

[30] D. Carlström. The Polysaccharide Chain of Chitin. *Biochim. Biophys. Acta*, 59:361–364, 1962.

[31] N. E. Dweltz. The Structure of β-chitin. *Biochim Biophys Acta*, 51:283–294, 1961.

[32] J. Blackwell. Structure of β-chitin or Parallel Chain Systems of Poly-$\beta-(1 \rightarrow 4)$-N-Acetyl-D-Glucosamine. *Biopolymers*, 7:281–298, 1969.

[33] K. H. Gardner and J. Blackwell. Refinement of the Structure of β-chitin. *Biopolymers*, 14:1581–1595, 1975.

[34] N. A. R. Gow, G. W. Gooday, J. D. Russell, and M.J. Wilson. Infrared and X-ray Diffraction Data on Chitins of Variable Structure. *Carbohydr. Res.*, 165:105–110, 1987.

[35] B. Focher, A. Naggi, G. Torri, A. Cosani, and M. Terbojevich. Structural Differences Between Chitin Polymorphs and their Precipitates from Solutions —Evidence from CP-MAS ^{13}C-NMR, FT-IR, and FT-Raman Spectroscopy. *Carbohydr. Polym*, 17:97–102, 1992.

[36] R. A. A. Muzzarelli. *Chitin*. Pergamon Press, New York, 1977.

[37] P. A. Sanford. Chitosan: Commercial Uses and Potential Applications. In G. Skjåk-Bræk, T. Anthonsen, and P. Sanford, editors, *Chitin and Chitosan*, pages 51–69. Elsevier, Amsterdam, 1989.

[38] C. Brine, P. Sanford, and J. Zikakis, editors. *Advances in Chitin and Chitosan*. Elsevier Science Publishers, London, 1992.

[39] R. Muzzarelli, C. Jeuniaux, and G. Gooday, editors. *Chitin in Nature and Technology*. Plenum Press, New York, 1986.

[40] S. Salmon and S. Hudson. Crystal Morphology, Biosynthesis, and Physical Assembly of Cellulose, Chitin, and Chitosan. *J. Macromol. Sci. Rev. Macromol. Chem. Phys.*, C37(2):199–276, 1997.

[41] K. A. Janes, M. P. Fresneau, A. Marazuela, A. Fabra, and M. J. Alonso. Chitosan Nanoparticles as Delivery Systems for Doxorubicin. *J. Controlled Release*, 73:255–267, 2001.

[42] K. Roy, H-Q. Mao, S-K-Huang, and K. W. Leong. Oral Gene Delivery with Chitosan-DNA Nanoparticles Generates Immunologic Protection in a Murine Model of Peanut Allergy. *Nat. Med.*, 5(4):387–391, 1999.

[43] H-Q. Mao, K. Roy, V. L. Troung-Le, K. A Janes, K. Y. Lin, Y. Wang, J. T. August, and K. W. Leong. Chitosan-DNA Nnanoparticles as Gene Carriers: Synthesis, Characterization and Transfection Efficiency. *J. Controlled Release*, 70:399–421, 2001.

[44] Z. Cui and R. J. Mumper. Chitosan-based Nanoparticles for Topical Genetic Immunization. *J. Controlled Release*, 75:409–419, 2001.

[45] F. Shikata, H. Tokumitsu, H. Ichikawa, and Y. Fukumori. *In Vitro* Cellular Accumulation of Gadolinium Incorporated into Chitosan Nanoparticles Designed for Neutron-capture Therapy of Cancer. *Eur. J. Pharm. Biopharm.*, 53:57–63, 2002.

[46] A. M. De Campos, A. Sánchez, and M. J. Alonso. Chitosan Nanoparticles: A New Vehicle for the Improvement of the Delivery of Drugs to the Ocular Surface. Application to Cyclosporin A. *Int. J. Pharm.*, 224:159–168, 2001.

[47] T. Banerjee, S. Mitra, A. K. singh, R. K. Sharma, and A. Maitra. Preparation, Characterization and Biodistribution of Ultrafine Chitosan Nanoparticles. *Int. J. Pharma.*, 243:93–105, 2002.

[48] F. Chen, Z-C. Wang, and C-J. Lin. Preparation andCharacterization of Nano-sized Hydroxyapatite Particles and Hydroxyapatite/Chitosan Nano-composite for use in Biomedical Materials. *Mater. Lett.*, 57(4):858–861, 2002.

[49] P. R. Austin, C. J. Brine, J.E. Castle, and J. P. Zikakis. Chitin: New Facets of Research. *Science*, 212:749–753, 1981.

[50] S. Tokura, N. Nishi, A. Tsutsumi, and O. Somorin. Studies on Chitin. VIII. Some Properties of Water Soluble Chitin Derivates. *Polymer J.*, 15:485–489, 1983.

[51] S. Tokura, S.I. Nishimura, N. Sakairi, and N. Nishi. Biological Activities of Biodegradable Polysaccharide. *Macromol. Symp.*, 101:389–396, 1996.

[52] R.C. Capozza. Spinning and Shaping Poly-(N-Acetyl-D-Glucosamine). US3988411, 1976.

[53] R.C. Capozza. Solution of Poly-(N-Acetyl-D-Glucosamine). US3989535. 1976.

[54] A. Hoekstra, H. Struszczyk, and O. Kivekäs. Percutaneous Microcrystalline Chitosan Application for Sealing Arterial Puncture Sites. *Biomaterials*, 19:1467–1471, 1998.

[55] R. N. Tharanathan and F. S. Kittur. Chitin—The Undisputed Biomolecule of Great Potential. *Crit. Rev. Food Sci. Nutr.*, 43:61–87, 2003.

[56] S. Senel and S. J. McClure. Potential Applications of Chitosan in Veterinary Medicine. *Adv. Drug Delivery Rev.*, 56:1467–1480, 2004.

[57] University of Delaware Graduate College of Marine Studies and the Sea Grant College Program [Web Site]. Horseshoe Crab Chitin Research. Retrived October 8, 2004. Available at: http://www.ocean.udel.edu/horseshoecrab/Research/chitin.html, October, 2004.

[58] France Chitine [WebSite]. Chitosan and Medicine. Retrived October 9, 2004. Available at: http://www.france-chitine.com/emed.htm, October, 2004.

[59] Vanson HaloSource [Web Site]. Biomedical Applications. Retrived October 18, 2005. Available at: http://www.vanson.com/biomedical_index.shtml, October 18, 2005.

[60] J. Synowiecki and N. A. Al-Khateeb. Production, Properties, and Some New Applications of Chitin and its Derivatives. *Crit. Rev. Food Sci. Nutr.*, 43(2):145–171, 2003.

[61] M. N. V. Ravi Kumar. A Review of Chitin and Chitosan Applications. *React. Funct. Polym.*, 46:1–27, 2000.

[62] W. J. Hennen. *Chitosan.* Woodland Publishing Inc., Pleasant Grove, UT, 1996.

[63] I. Olabarrieta. *Strategies to Improve the Aging, Barrier and Mechanical Properties of Chitosan, Whey and Wheat Gluten Protein Films.* PhD thesis, KTH, Fibre and Polymer Technology, Retrived December 19, 2005: Available at: http://urn.kb.se/resolve?urn=urn:nbn:se:kth:diva-208, 2005.

[64] Fifth Framework Programme [Web Site]. FP5 project. A New Natural Seed Coating Based on Chitosan. Retrived December 19, 2005. Available at: http://www.cordis.lu/data/PROJ_FP5/ACTIONeqDndSESSIONeq11248200-5919ndDOCeq52ndTBLeqEN_PROJ.htm.

[65] U.S. Environmental Protection Agency [Web Site]. Chitin; Poly-N-Acetyl-D-Glucosamine (128991) Fact Sheet. Retrived December 19, 2005. Available at: http://www.epa.gov/pesticides/biopesticides/ingredients/factsheets/factsheet-_128991.htm, January 26, 2005.

[66] M. McCoy. DuPont, UNC Partnership Yields Teflon Investment. *Chem. Eng. News*, 77:10, 1999.

[67] University of Leeds [Web Site]. Leeds Cleaner Synthesis Group. Retrived October 17, 2005. Available at: http: www.chem.leeds.ac.uk/People CMR/whatarescf.html, 2001.

[68] J. DeSimone. Personal communication, May, 2005.

[69] J. W. Tom, G. B Lim, P. G. Debenedetti, and R. K. Prud'homme. Applications of Supercritical Fluids in Controlled Release of Drugs. In J. F. Brennecke and E. Kiran, editors, *Supercritical Engineering Science: Fundamentals and Applications*, ACS Symp. Ser., Washington DC., 1992. American Chemical Society.

[70] B. W. Mueller and W. Fischer. Manufacturing of Sterile Sustained-release Drug Formulations Using Liquefied Gases. West Germany Patent, July 1989.

[71] D. W. Matson, R. C. Peterson, and R.D. Smith. The Preparation of Polycarbosilane Powders and Fibers During Rapid Expansion of Supercritical Fluid Solutions. *Mater. Lett.*, 4:429–432, 1985.

[72] R. C. D. Peterson, D. W. Matson, and R. D. Smith. Rapid Precipitation of Low Vapor Pressure Solids from Supercritical Fluid Solutions: The Formation of Thin Films and Powders. *J. Amer. Chem. Soc.*, 108:2100, 1985.

[73] D. W. Matson, J. L Fulton, R. C. Peterson, and R. D. Smith. Rapid Expansion of Supercritical Fluid Solutions: Solute Formation of Powders, Thin Films, and Fibers. *Ind. Eng. Chem. Res.*, 25:2298–2305, 1987.

[74] E. Reverchon, G. Della Porta, R. Taddeo, P. Pallado, and A. Stassi. Solubility and Micronization of Griseofulvin in Supercritical CHF_3. *Ind. Eng. Chem. Res.*, 34:4087–4091, 1995.

[75] I. Kikic, M. Lora, and A. Bertucco. A Thermodynamic Analysis of Three-Phase Equilibria in Binary and Ternary Systems for Applications in Rapid Expansion of a Supercritical Solution (RESS), Particles from Gas-Saturated Solutions (PGSS), and Supercritical Antisolvent (SAS). *Ind. Eng. Chem. Res.*, 36(12):5507–5515, 1997.

[76] E. Reverchon. Process for the Production of Micro and /or Nanoparticles. WO03004142, 2003.

[77] E. Reverchon. Process for the Production of Micro and /or Nanoparticles. US20040178529, 2004.

[78] M. Hanna and P. York. Method and Apparatus for the Formation of Particles. WO9600610, 1996.

[79] M. Hanna and P. York. Method and Apparatus for the Formation of Particles. US6063138, 2000.

[80] M. Hanna and P. York. Method Particles Formation. US6860907, 2005.

[81] R.Taylor and S. Zhai [Web Site]. Pharmaceutical Drying Technology. SEDS. Retrived October 19, 2005. Available at: www.cheng.cam.ac.uk/exemplarch2002/sz216/seds.html, 2002.

[82] R. B. Gupta and P. Chattopadhyay. Method of Forming Nanoparticles and Microparticle of Controllable Size Using Supercritical Fluids and Ultrasound. US6620351, 2003.

[83] P. Debye. *Polar Molecules*. Chemical Catalog Co., New York, 1929.

[84] R. H. Cole. On the Analysis of Dielectric Relaxation Measurements. *J. Chem. Phys.*, 23(3):493–499, 1955.

[85] T. Furukawa, M. Date, K. Nakajima, T. Kosaka, and I. Seo. Large Dielectric Relaxations in an Alternate Copolymer of Vinylidene Cyanide and Vinyl Acetate. *Jap. J. Appl. Phys.*, 25(8):1178–1182, 1986.

[86] J. R. Macdonald. *Impedance Spectroscopy: Emphasizing Solid Materials and Systems.* John Wiley and Sons, New York, 1987.

[87] Y. E. Rybov, H. Nuriel, G. Marom, and Y. Feldman. Relaxation Peak Broadening and Polymer Chain Dynamics in Aramid-Fiber-Reinforced Nylon-66 Microcomposites. *J. Polym. Sci. B: Polym. Phys.*, 41:217–223, 2003.

[88] R. M. Neagu, E. Neagu, N. Bonanos, and P. Pissis. Electrical Conductivity Studies in Nylon 11. *J. Appl. Phys.*, 88:6669–6677, 2000.

[89] N. McCrum, B. Read, and G. Williams. *Anelastic and Dielectric Effects in Polymeric Solids.* Wiley, London, 1967.

[90] H. Mallick and A. Sarkar. An Experimental Investigation of Electrical Conductivities in Biopolymers. *Bull. Mater. Sci.*, 23:319–324, 2000.

[91] J. Einfeldt, D. Meißbner, and A. Kwasniewski. Contributions to the Molecular Origin of the Dielectric Relaxation Processes in Polysaccharides —The High Temperature Range. *J. Non-Cryst. Solids*, 320:40–55, 2003.

[92] A. K. Arof Z. Osman, Z. A. Ibrahim. Conductivity Enhancement Due to Ion Dissociation in Plasticized Chitosan Based Polymer Electrolytes. *Carbohydr. Polym.*, 44:167–173, 2001.

[93] G. G. Raju. *Dielectrics in Electrical Fields.* Marcel Dekker Inc., New York, 2003.

[94] F. García, A. García-Bernabé, V. Compañ, R. Díaz-Calleja, J. Guzmán, and E. Riande. Relaxation Behavior of Acrylate and Methacrylate Polymers Containing Dioxacyclopentane Rings in the Side Chains. *J. Polym. Sci. B: Polym. Phys.*, 39:286–299, 2001.

[95] V. Compañ, J. Guzmán, R. Díaz-Calleja, and E. Riande. Relaxation Behavior of Methacrylic Polymers with Bulky Hydrophilic Groups in their Structures. *J. Polym. Sci. B: Polym. Phys.*, 37:3027–3037, 1999.

[96] O. Hirokazu, N. Seiko, T. Hiroaki, S. Yuki, I. Kotaro, and D. Kazumi. Pulmonary Gene Delivery by Chitosan-pDNA Complex Powder Prepared by a Supercritical Carbon Dioxide Process. *J. Pharm. Sci.*, 92:371–380, 2003.

[97] M. Yalpani. Supercritical Fluids: Puissant Media for the Modification of Polymers and Biopolymers. *Polymer*, 34:1102–1105, 1993.

[98] H. Wakayama, S. R. Hall, and S. Mann. Fabrication of $CaCO_3$-biopolymer Thin Films Using Supercritical Carbon Dioxide. *J. Mater. Chem.*, 15:1134–1136, 2005.

[99] E. Reverchon, G. Della Porta, I De Rosa, P. Subra, and D. Letourneur. Supercritical Antisolvent Micronization of Some Biopolymers. *J. Supercrit. Fluids*, 18:239–245, 2000.

[100] W. K. Snavely, B. Subramaniam, R. A. Rajewski, and M. R. Defelippis. Micronization of Insulin from Halogenated Alcohol Solution Using Supercritical Carbon Dioxide as an Antisolvent. *J. Pharm. Sci.*, 91:2026–2039, 2002.

[101] B-M. Min, S. W. Lee, J. N. Lim, Y. You, T. S. Lee, P. H. Kang, and W. H. Park. Chitin and Chitosan Nanofibers: Electrospinning of Chitin and Deacetylation of Chitin Nanofibers. *Polymer*, 45:7137–7142, 2004.

[102] M. Spasova, N. Manolova, D. Paneva, and I. Rashkov [Serial online]. Preparation of Chitosan-containing Nanofibres by Electrospinning of Chitosan/Poly(Ethylene Oxide) Blend Solutions. *e-Polymers*, 056:Retrived March 9, 2005. Available from: http://www.e–polymers.org/index.cfm., 2004.

[103] P. Sorlier, C. Viton, and A. Domard. Relation Between Solution Properties and Degree of Acetylation. *Biomacromolecules*, 3:1336–1342, 2002.

[104] K. Kurita M. Inoue M. Harata. Graft copolymerization of methyl methacrylate onto. *Biomacromolecules*, 3:147–152, 2002.

[105] H. Sato, H. Otani, S. Tsuge, K. Aoi, A. Takasu, and M. Okada. Characterization of Chitin-based Polymer Hybrids by Temperature-programmed Analytical Pyrolysis Techniques. 2. Chitin-Graft-Poly(2-Methyl-2-Oxazoline)/Poly(Vinyl Alcohol) Blends. *Macromolecules*, 33:357–362, 2000.

[106] F. S. Kittur, K. V. H. Prashanth, K. U. Sankar, and R. N. Tharanathan. Characterization of Chitin, Chitosan and their Carboxymethyl Derivatives by Differential Scanning Calorimetry. *Carbohyr. Polym*, 49:185–193, 2002.

[107] I. F. Kaymin, G. A. Ozolinya, and Ye. A. Plisko. Investigation of Temperature Transitions of Chitosan. *Polym. Sci. U.S.S.R.*, 22:171–177, 1980.

[108] L. Y. Lim, E. Khor, and C. E. Ling. Effects of Dry Heat and Saturated Steam on the Physical Properties of Chitosan. *J. Biomed. Mater. Res. (Appl. Biomater.)*, 48:111–116, 1999.

[109] R. Khachatoorian and I. G. Petrisor T. F. Yen. Prediction of Plugging Effect of Biopolymers Using their Glass Transition Temperatures. *J. Pet. Sci. Eng.*, 41:243–251, 2004.

[110] Y. Dong, Y. Ruan H. Wang Y. Zhao, and D. Bi. Studies on Glass Transition Temperature of Chitosan with Four Techniques. *J. Appl. Polym. Sci.*, 93:1553–1558, 2004.

[111] J. S. Ahn, H. K. Choi, and C. S. Cho. A Novel Mucoadhesive Polymer Prepared by Template Polymerization of Acrylic Acid in the Presence of Chitosan. *Biomaterials*, 22:923–928, 2001.

[112] M. Mucha and A. Pawlak. Thermal Analysis of Chitosan and its Blends. *Thermochim. acta*, 427:69–76, 2005.

[113] K. Sakurai, T. Maegawa, and T. Takahashi. Glass Transition Temperature of Chitosan and Miscibility of Chitosan/Poly(N-Vinyl Pyrrolidone) Bends. *Polymer*, 41:7051–7056, 2000.

[114] M. Pizzoli, G. Ceccorulli, and M. Scandola. Molecular Motions of Chitosan in the Solid State. *Carbohydr. Res.*, 222:205–213, 1991.

[115] Clarke [Web Site]. Rheology of Chitin. Retrived June 15, 2004. Available at: http://www.lboro.ac.uk/departments/cg/Projects/2001/clarke/introduction.html, 2001.

[116] S. Hirano and N. Nagao. *Agric. Biol. Chem.*, 52(8):2111–2112, 1988.

[117] J. J. Skujins, H. J. Potgieter, and M. Alexander. Dissolution of Fungal Cell Walls by a Streptomycete Chitinase and β-(1$\rightarrow$3) Glucanase. *Arch. Biochem. Biophys.*, 111:358–364, 1965.

[118] C. Jeuniaux. Chitinases. *Methods Enzymol.*, 8:644–650, 1966.

[119] J.F. Ely. CO2PAC: A Computer Program to Calculate Physical Properties of Pure CO_2. National Bureau of Standards, Boulder, CO 1986.

[120] G. Cárdenas, G. Cabrera, E. Taboada, and S. P. Miranda. Chitin Characterization by SEM, FTIR, XRD, and ^{13}C Cross Polarization/Mass Angle Spinning NMR. *J. Appl. Polym. Sci.*, 93:1876–1885, 2004.

[121] N. B. Colthup, L. H. Daly, and S. E. Wiberley. *Introduction to Infrared and Raman Spectroscopy.* Academic Press, San Diego, 3rd edition, 1990.

[122] K. S. Guigley. *Hydrogen Bonded Polymer Blends.* PhD thesis, Department of Materials Science and Engineering. The Pennsylvania State University, December 2001.

[123] M-K. Jang, B-G. Jeong, C. H. Lee, and J-W. Nah. Physicochemical Characterization of α-chitin, β-chitin, and γ-chitin Separated from natural Resources. *J. Polym. Sci. A: Polym. Chem.*, 42:3423–3432, 2004.

[124] S. S. Kim, S. H. Kim, and Y. M. Lee. Preparation, Characterization, and Properties of β-chitin and N-acetylated β-chitin. *J. Polym. Sci. B: Polym. Phys.*, 34:2367–2374, 1996.

[125] C. T. Andrade, K. M. P. Silva, M. I. Tavares, R. A. Simão, C. Achete, and C. A. Pérez. Comparative Study on Structural Features of α Chitin for *Xiphopenaeus kroyeri* and its Precipitated Product from Phosphoric Acid Solution. *J. Appl. Polym. Sci.*, 83:151–159, 2002.

[126] M. T. Viciosa, M. Dionisio, R. M. Silva, and J. F. Mano. Molecular Motions in Chitosan Studied by Dielectric Relaxation Spectroscopy. *Biomacromolecules*, 5:2073–2078, 2004.

[127] A. E. H. Bekkali, I. Thurzo, T. U. Kampen, and D. R. T. Zahn. Impedance Spectroscopy Study of Metal-organic-metal Structures. *Appl. Surf. Sci.*, 234:149–154, 2004.

[128] L. M. Huang, T.Ch. Wen, and A. Gopalan. Polymer-polymer Rectifying Heterojunction Based on Poly(3,4-Dicyanothiophene) and MEH-PPV. *Thin Solid Films*, 473:300–307, 2005.

[129] J. Zhou, G. Tzamalis, N.A. Zaidi, N.P. Comfort, and A.P. Monkman. Effect of Thermal Aging on Electrical Conductivity of the 2-Acrylamido-2-Methyl-1-Propanesulfonic Acid-doped Polyaniline Fiber. *J. Appl. Polym. Sci.*, 79:2503–2508, 2001.

[130] V. Jousseaume, M. Morsli, and A. Bonnet. Thermal Behavior of Polyaniline Films and Polyaniline-polystyrene Blends. *J. Appl. Polym. Sci.*, 84:1848–1855, 2002.

[131] Z. Montiel-González. Estudio elipsométrico en películas delgadas de poliestireno y quitosán. Master's thesis, Cinvestav-Querétaro, Querétaro, Qro., México, Manuscript in preparation 2006.

Appendix A

Publications and Presentations

A.1 Publications

- **Louvier-Hernández, J.F.**, Luna-Bárcenas, and Gupta, R.B., *Characterization of SAS processed three-dimensional chitin nanofibrous scaffold*, Manuscript in preparation, (2006).

- **Louvier-Hernández, J.F.**, Luna-Bárcenas, G., Evgene, P., and Nuño-Donlucas, S.M., *Thermal relaxations of Chitosan Films*, Manuscript in preparation, (2006).

- Zakharchenko, R.V., Horley, P.P., Vorobiev, Yu.V., Gorley, P.N., **Louvier-Hernández, J.F.**, Luna-Bárcenas, G., and González-Hernández, J., *Quantum-mechanical treatment of electronic spectra of nanostructured materials using the "mirror" boundary conditions*, Manuscript in preparation, (2006).

- **Louvier-Hernández, J.F.**, Luna-Bárcenas, G., Thakur, R., and Gupta, R.B., *Formation of chitin nanofibers by supercritical antisolvent*, J. Biomed. Nanotech., Vol. **1**, 109, (2005).

- Quintero-Ortega, I.A., Vivaldo-Lima, E., Luna-Bárcenas, G., Alvarado, J.F.J., and **Louvier-Hernández, J.F.**, *Modeling of the Free-Radical Copolymerization Kinetics with Crosslinking of Vinyl/Divinyl Monomers in Supercritical Carbon Dioxide*, Ind. Ing. Chem. Res., Vol. **44**, 2823, (2005).

A.2 Oral and Poster Presentations

- **Lecture.** "Thermal relaxations of chitosan films." II Minicongreso Estudiantil Cinvestav-Querétaro, November 2005, Querétaro, Querétaro.

- **Poster.** "Formation of Nanostructured Chitin by Supercritical Antisolvent Precipitation." II Minicongreso Estudiantil Cinvestav-Querétaro, November 2005, Querétaro, Querétaro.

- **Lecture.** "Nanofibrous chitin scaffold prepared by supercritical antisolvent." XVIII Congreso Nacional de la Sociedad Polimérica de México, October 2005, Puerto Vallarta, Jalisco.

- **Lecture.** "Desarrollo, Innovaciones Tecnológicas y Caracterización de Biomateriales." XVII Jornada de Ingeniería Bioquímica, Departamento de Ingeniería Bioquímica, Instituto Tecnológico de Celaya, October 2005, Celaya, Guanajuato.

- **Lecture.** "Desarrollo de materiales nanoestructurados mediante fluidos supercríticos para aplicaciones biomédicas." XXV Aniversario del Posgrado en Ingeniería Química, Departamento de Ingeniería Química, Instituto Tecnológico de Celaya, September 2005, Celaya, Guanajuato.

- **Lecture.** "Formación de nanofibras de quitina mediante anti-solvente supercrítico." Seminario Departamental, Departamento de Ingeniería Química, Instituto Tecnológico de Celaya, April 2005, Celaya, Guanajuato.

- **Poster.** "Formation of Nanostructured Chitin by Supercritical Antisolvent Precipitation." 7th International Symposium on Supercritical Fluids, May 2005, Orlando, FL, USA.

- **Lecture.** "Formation of Chitin Nanoparticles and Nanofibers Using Supercritical CO_2." Annual Conference of the AIChE, November 2004, Austin, TX, USA.

- **Poster.** "Formation of Chitin Nano-Fibers by Supercritical Antisolvent." XVII Congreso Nacional de la Sociedad Polimérica de México, November 2004, Chihuahua, Chihuahua.

Appendix B

Laboratory Standard Methods

Standard methods developed for the quality system in Supercritical Fluids and Polymer Laboratory at Cinvestav-Querétaro

B.1 Standard Method for Chitin Purification

12-SM-001

Laboratorio de
fluidos supercríticos
y polímeros

Excelencia en
investigación
y posgrado

Cinvestav-Querétaro

Standard Method
Chitin Purification

12-SM-001

Total pages: 4 (Four)

Elaboration date: Jul 1, 2005 Rev 0

Substitutes: New

Elaborated by:

José Francisco Louvier H.

Jhoana Aréchiga Carbajal

Revised by:

Dr. Gabriel Luna Bárcenas
Investigador Responsable

M.C. Reina Araceli
Mauricio Sánchez
Auxiliar de Investigación

Autorized by:

Dr. José Luis Alejandro
Naredo Villagrán
Director Unidad Querétaro

1. PURPOSE.

1.1. To purify 10 g of chitin from shellfish sources.

2. SCOPE.

2.1. All shellfish derived sources of chitin from commercial vendors. Specially chitin practical grade from crab shell (Sigma).

3. RESPOSABILITY.

3.1. All students of Dr. Gabriel Luna Bárcenas and M.C. Reina Araceli Mauricio Sánchez.

4. SAFETY.

4.1. Students must worn apron, safety glasses and gloves at all times.
4.2. All acids and bases must be handled in the fume-hood.

5. TERMINOLOGY.

5.1. Chitin: Biopolymer.

6. METHOD.

6.1. Materials and apparatus

- 6.1.1. Raw Chitin
- 6.1.2. 800 mL of 5 % Sodium Hydroxide (NaOH)
- 6.1.3. 180 mL of 1 N Hydrochloric Acid (Hcl)
- 6.1.4. Deionized and distilled water
- 6.1.5. Mechanical stirrer and magnetic bar
- 6.1.6. 1 L Beaker
- 6.1.7. Crystallization dish
- 6.1.8. Parafilm
- 6.1.9. pH paper
- 6.1.10. Pipet

6.2. Preparation of acid and base dissolutions

- 6.2.1. Add slowly 18 mL of 36.5 % HCl into 160 mL of deionized water.
- 6.2.2. Add slowly 40.5 g of NaOH (assay 98.7%) into 800 mL of deionized water.
- 6.2.3. **NOTE:** Keep the beaker cool (immersed in iced water) and stir during the addition of both acid and base into the water, to avoid overheating. And always inside the fume-hood.

6.3. Purification of Chitin

6.3.1. *Deproteinization*

- 6.3.1.1. Weigh 10 g of raw chitin and place into a 1 L beaker along with a magnetic bar
- 6.3.1.2. Add 800 mL of 5 % (w/v) NaOH solution
- 6.3.1.3. Stir the raw chitin suspended mixture with a mechanical stirrer for 7 days at room temperature. Adjust the stirring speed so that the solution is swirled homogeneously without any spillage or splashing of the solution and cover the top of the beaker with parafilm to minimize evaporation of NaOH.
- 6.3.1.4. After 7 days of stirring, turn off the stirrer and wash the chitin mass with distilled water until the washings are pH neutral as indicated by pH paper.
- 6.3.1.5. Dispose the washing water appropriately.
- 6.3.1.6. Allow to air dry for one day.

6.3.2. *Demineralization.*

- 6.3.2.1. Add the dry neutral washed chitin into 1 M of HCl solution ensuring that the chitin is immersed in the acid. It is important to ensure that the chitin is almost dried before transferring into the acid to minimize diluting the solution.

6.3.2.2. Stir the suspended chitin mixture for 2 h.

6.3.2.3. Allow the chitin to settle down again and decant most of the HCl followed by several washes with distilled water until the washings are pH neutral as indicated by pH paper.

6.3.2.4. Decant the distilled water and dispose appropriately.

6.3.2.5. Place the chitin into a crystallization dish covered with a paper sheet, and allow to air dry for 1 day.

6.3.2.6. Finally, place the crystallization dish containing chitin in a stove at 150 °C for 48 h.

6.3.2.7. Store in an ambeer flask away from light until required.

6.3.3. *Ash Test. Mineral content.*

6.3.3.1. Weigh a Petri dish with cap (W_{ds}). And record this data.

6.3.3.2. Weigh 1.0 g of purified chitin (W_{pc}) and put in the Petri dish.

6.3.3.3. Repeat 6.3.3.1 and 6.3.3.2 for raw chitin.

6.3.3.4. Put both samples in in a plate of heating for its calcination.

6.3.3.5. Put both samples in the muffle furnace at 800 °C for 6 h.

6.3.3.6. Weigh the Petri dish with the ashes (W_{da}) and do the math:

$$W_{ash} = W_{da} - W_{ds}$$

$$\text{Purity } \% = ((W_{pc} - W_{ash}) / W_{pc}) \times 100$$

6.3.3.7. Any remaining ash was assumed to be calcium carbonate.

7. HISTORY.

• July, 2005	First Edition

8. REFERENCES.

8.1. E. Khor. Chitin: Fulfilling a biomaterials promise. Elsevier, 2001.
8.2. Capozza. US Patent 3989535 (1976)
8.3. R. A. A. Muzzarelli. Chitin. Pergamon Press. Oxford. 1977, pp 57-58.
8.4. A. Pastor de Abram. Quitin y Quitosano: Obtención, caracterización y aplicaciones. Pontificia Universidad Católica del Perú/Fondo Editorial, 2004, pp 158.
8.5. Rheology of Chitin. Web site address: www.lboro.ac.uk/departments/cg/Projects/2001/clarke/exper.html#chitinpurif

ANNEX 1
FLUX DIAGRAM.

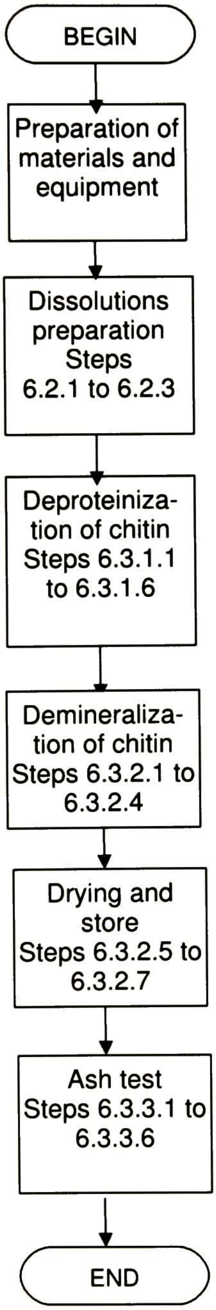

B.2 Standard Method for Chitosan Film Preparation 12-SM-004

Laboratorio de
fluidos supercríticos
y polímeros

Excelencia en
investigación
y posgrado

Cinvestav-Querétaro

Standard Method
Chitosan Film Preparation

12-SM-004

Total pages: 4 (Four)

Elaboration date: Feb 27, 2006 Rev 0

Substitutes: New

Elaborated by:

José Francisco Louvier H.

J. Betzabe González Campos

Revised by:

Dr. Gabriel Luna Bárcenas
Investigador Responsable

M.C. Reina Araceli Mauricio Sánchez
Auxiliar de Investigación

Autorized by:

Dr. Arturo Mendoza Galván

Coordinado Técnico

1. PURPOSE.

1.1. To prepare chitosan films for dielectric measurements.

2. SCOPE.

2.1. Chitosan form commercial vendors.

3. RESPOSABILITY.

3.1. All students of Dr. Gabriel Luna Bárcenas and M.C. Reina Araceli Mauricio Sánchez.

4. SAFETY.

4.1. Students must worn apron, safety glasses and gloves at all times.
4.2. All acids and bases must be handled in the fume-hood.

5. TERMINOLOGY.

5.1. Chitosan: Biopolymer.

6. METHOD.

6.1. Materials and apparatus

6.1.1. Chitosan from commercial vendors.
6.1.2. Acetic acid 1.0 wt%.
6.1.3. Sodium hydroxide 0.1 M.
6.1.4. Mechanical stirrer and magnetic bar.
6.1.5. pH paper.
6.1.6. Plastic Petri Dish.
6.1.7. 100 mL beaker.
6.1.8. Disposable transfer pipet.

6.2. Preparation of acid and base dissolutions

6.2.1. Add slowly 1.0 mL of glacial acetic acid (100%) into 99 mL of deionized water.
6.2.2. Add slowly 0.202 g of NaOH (assay 98.7%) into 50 mL of deionized water.
6.2.3. **NOTE:** Keep the beaker cool (immersed in iced water) and stir during the addition of base into the water, to avoid overheating. And always inside the fume-hood.

6.3. Chitosan film preparation

6.3.1. *Chitosan dissolution*

6.3.1.1. Weigh 1 g of chitosan and place into a 100 mL beaker along with a magnetic bar
6.3.1.2. Add 99 mL of 1.0 wt% Acetic Acid solution
6.3.1.3. Stir the chitosan suspended mixture with a mechanical stirrer for 1 hr at room temperature.
6.3.1.4. After complete dissolution, store at room temperature.

6.3.2. *Solvent-cast film*

6.3.2.1. Add slowly the chitosan solution 1 wt% into the top part of a plastic Petri dish until half of height of Petri dish. Use a disposable transfer pipet.
6.3.2.2. Allow the solution to dry at room temperature for 24 h.
6.3.2.3. Put the Petri dish inside an oven at 60 ºC overnight.
6.3.2.4. **Note:** Chitosan films obtained by this procedure are in the non-neutralized form with the amino side group protonated, called chitosan acetate films.
6.3.2.5. Store in a dessicator away from light until required.

6.3.3. *Neutralization of chitosan acetate film*

6.3.3.1. Add slowly 5 mL of the NaOH 0.1 M solution into the Petri dish with the chitosan acetate film.
6.3.3.2. Stir gentle with you hand to ensure the dissolution get in contact with the film. Also use tweezers to allow free movement of the film.
6.3.3.3. Dispose the NaOH solution after washing the film. Add another 5 mL of NaOH 0.1 M solution.
6.3.3.4. Repeat steps 6.3.3.2 and 6.3.3.3 until neutral pH.
6.3.3.5. Put the bottom part of Petri dish inside the top part, both facing up as depicted in Figure 1. This process will ensure that chitosan film will not roll up when drying.

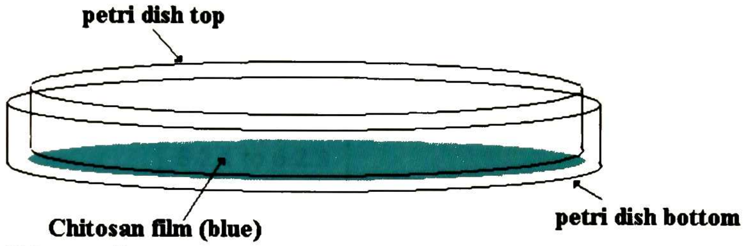

Figure 1. Chitosan film after neutralization covered with bottom Petri dish for drying.

6.3.3.6. Put the film inside an oven at 60 °C overnight.

6.3.3.7. Store in a dessicator away from light until required.

7. HISTORY.

•	February, 2006	First Edition

8. REFERENCES.

8.1. M. T. Viciosa, M Dionísio, R.M. Silva, R. L. Reis, and J.F. Mano. Molecular motions in chitosan studied by dielectric relaxation spectroscopy. *Biomacromolecules.* 5: 2073-2078, 2004.

ANNEX 1
FLUX DIAGRAM.

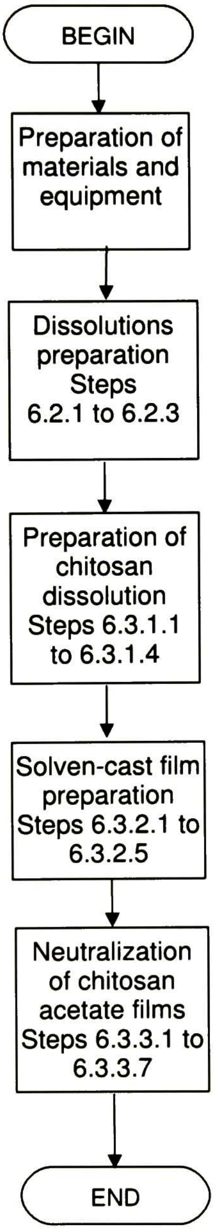

Vita

José Francisco Louvier Hernández was born in Puebla City, Puebla, México on November 17, 1975, the fifth son out of eight of Maria de Lourdes Hernández and Eduardo Louvier. After completing High School at Instituto México de Puebla in 1993, he entered the College of Engineering at Universidad Popular Autónoma del Estado de Puebla (UPAEP). He recived the degree of Bachelor of Science with honors from UPAEP in January 1999. He received his degree on Master of Science in Chemical Engineering from Instituto Tecnológico de Celaya in November 2000. The following year he held a position in Mabe Celaya (a joint venture with General Electric Appliances). In January 2002, he began doctoral studies in Materials Science at Cinvestav-Querétaro. During that time, he spent one year as a Research Scholar at Auburn Univeristy with a Fulbright-García Robles scholarship.

This dissertation was typeset with LaTeX 2_{ε}[1] by the author

---

[1] LaTeX 2_{ε} is an extension of LaTeX. LaTeX is a collection of macros for TeX. TeX is a trademark of the American Mathematical Society.

EL JURADO DESIGNADO POR LA UNIDAD QUERÉTARO DEL CENTRO DE INVESTIGACIÓN Y DE ESTUDIOS AVANZADOS DEL INSTITUTO POLITÉCNICO NACIONAL, APROBÓ LA TESIS DEL C. JOSÉ FRANCISCO LOUVIER HERNÁNDEZ TITULADA: "NANOFIBRAS DE QUITINA PROCESADAS MEDIANTE DIÓXIDO DE CARBONO SUPERCRÍTICO Y PROPIEDADES TÉRMICAS DE PELÍCULAS DE QUITOSÁN", FIRMAN AL CALCE DE COMÚN ACUERDO LOS INTEGRANTES DE DICHO JURADO, EN LA CIUDAD DE QUERÉTARO, QRO., A LOS 17 DE ABRIL DE 2006.

Aldo Humberto Romero C

DR. ALDO HUMBERTO ROMERO CASTRO
INVESTIGADOR CINVESTAV 3B
CINVESTAV-QUERÉTARO

R. Ramírez Bon

DR. RAFAEL RAMÍREZ BON
INVESTIGADOR CINVESTAV 3C
CINVESTAV-QUERÉTARO

DR. EVGEN PROKHOROV FEDEROVITCH
INVESTIGADOR CINVESTAV 3C
CINVESTAV-QUERÉTARO

DR. ARTURO MENDOZA GALVÁN
INVESTIGADOR CINVESTAV 3C
CINVESTAV-QUERÉTARO

PROF. KIRK J. ZIEGLER
ASSISTANT PROFESSOR
UNIVERSITY OF FLORIDA